ORNL/ SPR-2015/263

Preliminary Assessment of the Impact on Reactor Vessel dpa Rates Due to Installation of a Proposed Low Enriched Uranium (LEU) Core in the High Flux Isotope Reactor (HFIR)

Charles Daily

October 2015

OAK RIDGE NATIONAL LABORATORY
MANAGED BY UT-BATTELLE FOR THE US DEPARTMENT OF ENERGY

ORNL/ SPR-2015/263

Reactor and Nuclear Systems Division
Radiation Transport Methods Group

PRELIMINARY ASSESSMENT OF THE IMPACT ON REACTOR VESSEL DPA RATES DUE TO INSTALLATION OF A PROPOSED LOW ENRICHED URANIUM (LEU) CORE IN THE HIGH FLUX ISOTOPE REACTOR (HFIR)

Charles Daily

Date Published: October 2015

Prepared by
OAK RIDGE NATIONAL LABORATORY
Oak Ridge, TN 37831-6283
managed by
UT-BATTELLE, LLC
for the
US DEPARTMENT OF ENERGY
under contract DE-AC05-00OR22725

CONTENTS

LIST OF FIGURES

LIST OF TABLES

ACRONYMS AND ABBREVIATIONS

ADVANTG	Automated Variance Reduction Generator
ASTM	American Society for Testing and Materials
BOC	beginning of cycle
CADIS	Consistent Adjoint Driven Importance Sampling
CPU	central processing unit
DOE	US Department of Energy
DOORS	Discrete Ordinates of Oak Ridge System
DORT	two-dimensional neutron/photon transport
FOM	figure of merit
FP	fission product
FW-CADIS	Forward-Weighted CADIS
dpa	displacements per atom
ENDF	evaluated nuclear data file
EOC	end of cycle
HB	horizontal beam
HEU	highly enriched uranium
HFIR	High Flux Isotope Reactor
IC	ion chamber
IFE	inner fuel element
IFT	inner flux trap
KCODE	MCNP direct method for calculating k_{eff}
LANL	Los Alamos National Laboratory
LEU	low enriched uranium
MC	Monte Carlo
MCNP	MC N-Particle
MCNPX	MCNP alternate version
MCTAL	MC tally results file
MW	megawatt
NNSA	National Nuclear Security Administration
od	octal dump
OECD	Organisation for Economic Co-Operation and Development
OFE	outer fuel element
OIC	ORNL Institutional Cluster
OMP	OpenMP
ORIGEN	ORNL Isotope Generation and Depletion Code
ORNL	Oak Ridge National Laboratory
PKA	primary knock-on atom
RMS	root-mean-square
RSICC	Radiation Safety Information Computational Center
RV	reactor vessel
SDEF	source definition
SB	source bias
SI	source information
SP	source probabilities
TORT	three-dimensional neutron/photon transport
V&V	verification and validation
VESTA	Visualization for Electronical and Structural Analysis
WWP	weight window parameter
ZAID	an isotope's atomic number (Z) and mass number (A) identification

EXECUTIVE SUMMARY

An assessment of the impact on the High Flux Isotope Reactor (HFIR) reactor vessel (RV) displacements-per-atom (dpa) rates due to operations with the proposed low enriched uranium (LEU) core described by Ilas and Primm [1] has been performed and is presented herein. The analyses documented herein support the conclusion that conversion of HFIR to low-enriched uranium (LEU) core operations using the LEU core design of Ilas and Primm [1] will have no negative impact on HFIR RV dpa rates.

Since its inception, HFIR has been operated with highly enriched uranium (HEU) cores. As part of an effort sponsored by the National Nuclear Security Administration (NNSA), conversion to LEU cores is being considered for future HFIR operations. The HFIR LEU configurations analyzed are consistent with the LEU core models used by Ilas and Primm and the HEU balance-of-plant models used by Risner and Blakeman [2] in the latest analyses performed to support the HFIR materials surveillance program [3–6].

The Risner and Blakeman analyses, as well as the studies documented herein, are the first to apply the hybrid transport methods available in the Automated Variance reduction Generator (ADVANTG) [7] code to HFIR RV dpa rate calculations. These calculations have been performed on the Oak Ridge National Laboratory (ORNL) Institutional Cluster (OIC) with version 1.60 of the Monte Carlo N-Particle 5 (MCNP5) computer code.

1. INTRODUCTION

Since its inception, the High Flux Isotope Reactor (HFIR) has been operated with highly enriched uranium (HEU) cores. As part of an effort sponsored by the National Nuclear Security Administration (NNSA), conversion to low enriched uranium (LEU) cores is being considered for future HFIR operations. An assessment of the impact on HFIR reactor vessel (RV) damage due to operations with the LEU core described by Ilas and Primm [1] has been performed and is presented herein.

Displacements-per-atom (dpa) have long been used to correlate radiation exposure and RV damage. This report describes the methods and models involved in determining the dpa rates in the HFIR RV for LEU core operations. The dpa rates at beginning-of-cycle (BOC) and end-of-cycle (EOC) have been calculated. The dpa rates presented in Section 4 consist of both neutron- and photon-induced components. Risner and Blakeman [2] performed similar analyses for the current HEU core configuration. A comparison of the HEU and LEU dpa rates in the HFIR RV demonstrates that the calculated dpa rates with the proposed LEU core installed are lower than those calculated for the current HEU core and thus support a preliminary conclusion that conversion of HFIR to LEU core operations will have no negative impact on vessel damage.

The analyses of Risner and Blakeman are the latest in a series of studies performed in support of the HFIR materials surveillance program [3–6]. The purpose of this program, which has been in place since the 1960s, is to analyze, update, and document the effects of radiation-induced embrittlement on the HFIR RV. A variety of modeling techniques have been employed in support of the HFIR materials surveillance program over the years. Historically, 1-, 2-, and where feasible, limited 3-D deterministic transport methods have been used to calculate the dpa rates at the HFIR RV. Use of stochastic transport codes, such as MCNP [8], to calculate statistically meaningful results over a large portion of a given model, where the results of interest are in regions dominated by significant (many orders of magnitude) attenuation between the source and the regions of interest, has traditionally been intractable. Recent advances in the area of hybrid transport methods, which combine deterministic and stochastic techniques, have made it feasible to obtain such global, deep-penetration results with stochastic transport codes like MCNP5.

The HEU analyses of Risner and Blakeman [2] and the LEU analyses documented herein are the first to apply the hybrid transport methods available through the Automated Variance Reduction Generator (ADVANTG) [7] code to the calculation of dpa rates in the HFIR RV. ADVANTG is a powerful suite of software that combines the strengths of the deterministic transport code, Denovo [9], and the stochastic transport code, MCNP5 [8], to minimize both the user's effort and computational burden involved in the calculation of local or global flux solutions (or any related response functions like dose, dpa rates, etc.) for a wide range of fixed-source applications. ADVANTG employs either the Consistent Adjoint Driven Importance Sampling (CADIS) [10] or Forward-Weighted CADIS (FW-CADIS) [11] algorithms to automatically generate variance reduction parameters (weight windows and consistently biased sources) for MCNP5. Implementation of the methods available in ADVANTG is straightforward: the user provides a single model description (i.e., the MCNP input file) and an auxiliary input file with a minimal set of user-defined parameters to

- control the discretization of the model,
- define the nuclear data library to use,
- request the creation and format of various output files,
- invoke specific variance reduction generation algorithms,
- specify one or more tallies for which the weight windows and biased source will be optimized, and
- control execution of both ADVANTG and Denovo.

ADVANTG will read the MCNP model and the auxiliary input, and then will automatically

- generate and execute a complete Denovo input file in serial or parallel mode,
- process the Denovo output to generate a weight windows file and biased source description for MCNP, and
- modify the original MCNP input file to include the biased source cards.

After execution of ADVANTG, the user needs only to submit the automatically modified MCNP input file.

ADVANTG has been applied to a wide variety of difficult, real-world problems. Depending on the complexity of the problem and the extent over which results are desired, improvements in the tally figure of merit (FOM) ranging between 10^1 and 10^4 have been seen for single-detector problems employing the CADIS and FW-CADIS methods. Note that the FOM is defined as $1/R^2T$, where R is the tally relative error, and T is the time required to converge the solution to a relative error of R. For analog MCNP runs (i.e., cases in which no variance reduction is applied), the value of T will only include the time required to execute MCNP. For jobs employing the variance reduction techniques of ADVANTG, T will include both the ADVANTG and ADVANTG-accelerated MCNP run times.

ADVANTG is available for multiple computing platforms. The results documented herein have been generated on the Oak Ridge National Laboratory (ORNL) Institutional Cluster (OIC) Linux cluster. The ADVANTG-generated weight windows and biased sources were used with MCNP5, version 1.60 on the OIC. Testing of multiple MCNP5, version 1.60 executables on the OIC, each generated with slightly different compilation options, has been performed. Results of these verification tests and comparison of selected design calculations performed on both the OIC and Betty clusters are documented in Appendix A.

2. BACKGROUND

An extensive, well-documented materials surveillance program to analyze, update, and document the effects of radiation-induced embrittlement on the HFIR RV has been in place since the 1960s. According to Cheverton [12], "At the time the HFIR vessel was being designed (late 1950s, early 1960s), it was recognized that a vessel materials surveillance program, to check on radiation embrittlement rates, was necessary." Cheverton [12] provides an excellent summary of the material surveillance program through 2010, as well as a substantial list of references related to the program. The initial documentation of the surveillance program [3] specified locations for the placement of Charpy V-notch specimens and dosimeters. Per Cheverton, various specimens and dosimeters were removed and analyzed in 1969, 1974, 1984, and 1986. Results of the 1986 analysis led to modification of the materials surveillance program [4] and required additional specimens to be analyzed in 1993. Additional modifications to the material surveillance program were made to address life extension and beam tube modification plans [5] and to incorporate new dosimetry data and analysis capabilities [6]. In 1994, the significant contribution of photons to the total dpa rates in the vessel was identified [13,14].

Blakeman and Cheverton [15] issued a comprehensive update to the calculated fluxes and dpa rates at the HFIR RV beltline region. The flux and dpa rate calculations of their work were performed with various codes from the Discrete Ordinates of Oak Ridge System (DOORS) [16] code package, as well as other related utilities [17, 18]. At the time, the 2- and 3-dimensional (2D and 3D) deterministic transport codes from the DOORS suite represented the state-of-the-art for obtaining the global, deep penetration flux solutions required for the HFIR RV dpa rate analyses of Blakeman and Cheverton [15]. The ADVANTG

software was actively being developed and improved at the time, and a recommendation was made in Blakeman and Cheverton [15] to pursue fully stochastic solutions for future HFIR RV dpa rate analyses.

Risner and Blakeman [2] applied the hybrid methods of an earlier version of ADVANTG (ADVANTG2) to the latest analysis of dpa rates in the HFIR RV. Their analyses present a wide range of calculations based on the cycle 400 model of HFIR with an HEU core [19]. Fluxes in the RV and in all dosimetry key locations were recalculated, and comparisons of the deterministic and ADVANTG-accelerated stochastic (MCNP) results were made. Comparisons of the MCNP fluxes to measured values were also made. While the analyses of Risner and Blakeman [2] were underway, the proposed LEU core design of Ilas and Primm [1] was finalized. Blakeman developed shielding models that incorporated the LEU core of Ilas and Primm [1] and used the older ADVANTG2 code to calculate dpa rates in the reactor vessel of these models. Both the HEU and LEU cycle 400 models have been subsequently reanalyzed with ADVANTG3. These LEU analyses are focused entirely on the dpa rates in the HFIR RV; no analysis of the dosimetry keys or comparisons to measurements was performed for the LEU model.

3. DISCUSSION

3.1 METHODS

3.1.1 Hybrid Transport Methods

Previous analyses of the neutron and gamma dpa rates in the HFIR RV have been conducted using primarily deterministic transport methods. The most recent of these analyses [15] made extensive use of the 2D (DORT) and 3D (TORT) deterministic transport codes from the DOORS [16] code package, as well as various other related utilities [17,18] that are not part of the DOORS system. Deterministic methods have long been the computational standard for typical deep penetration shielding analyses. These analyses are characterized by the need for a high fidelity solution over much if not all of a given solution space, with significant (i.e., many orders of magnitude) attenuation occurring between the source(s) of particles and the regions of the geometry where the particle flux, and/or one or more responses (e.g., dpa rates) are desired.

While the ability to obtain global solutions from numerous distributed sources is a strength of deterministic methods, the need to discretize the solution space in all spatial, angular, and energy variables (and time for transient problems) leads to certain limitations. Because most deterministic transport codes, including those in the DOORS package, have traditionally been restricted to the use of orthogonal, rectilinear grids, the ability to rigorously represent curved surfaces is not possible. The solution accuracy in the vicinity of such surfaces will be limited by how fine of a spatial mesh can be used to define these surfaces. Regardless of how fine of a spatial mesh can be accommodated on a given computing platform, the solution will still only be approximate in the vicinity of curved surfaces, and some type of post processing will be needed to interpolate from the solution calculated on the rectilinear grid to the locations desired on the smooth surfaces of the problem geometry. Appendix B of Blakeman and Cheverton [15] describes how this smoothing of the gridded solution was performed for that analysis.

In addition to discretization in one, two, or three spatial dimensions, the direction that particles are traveling before and after any scattering interactions, as well as the particle energies before and after a scattering event, must be discretized. To capture the detail of narrow-angle scatters in long, thin regions such as pipe walls or void streaming in regions of low density material such as air, a large angular quadrature is desired. To appropriately account for the physics of how neutrons and gamma rays either lose energy or are absorbed when they interact with matter, a large number of energy groups may be required. The ability to discretize a complex reactor system with enough spatial cells, angular directions, and energy groups is primarily limited by the size of the available computing facility. While large

supercomputers can accommodate full 3D deterministic models, the size of HFIR deep penetration shielding analyses are typically limited to 2D or 2D/3D hybrid techniques on smaller computing clusters. In the 2D/3D hybrid method used in Blakeman and Cheverton [15], complex 2D solutions are used to generate boundary sources for a 3D model that describes a small portion of the full geometry (e.g., limited to the vicinity of a nozzle or beam tube) in more detail than could be used in a 3D model covering the entire geometry. The entire geometry spans 3 m in height and 1.5 m in radius.

To avoid the limitations of discretization inherent in the deterministic methods used for prior HFIR vessel damage analyses, a stochastic transport approach, commonly referred to as the Monte Carlo (MC) method, was proposed as a possibility in Blakeman and Cheverton [15]. The ability to use an exact geometrical representation of any combination of physical structures that can be defined by quadratic surfaces, the use of continuous energy nuclear interaction (cross section) data, and the ability to rigorously account for changes in a particle's direction of travel following an interaction, makes the MC method suitable for a wide variety of analyses. However, the method tracks individual particles and must have a sufficient population of particles at any given location in phase-space (location, energy, angle) to generate a statistically valid representation of the average behavior of all particles at that location in phase-space. Therefore, problems with numerous distinct sources and/or significant amounts of attenuating material between the source(s) and locations where a particular response is to be calculated (detector region) pose a substantial challenge for the MC method. Complicated streaming paths between the source(s) and detector(s), and/or numerous detector locations also pose significant challenges for the MC method. For example, typical shielding analyses involve the generation of response functions (e.g., dose or dpa rates) in locations where the particle flux may be 10–15 orders of magnitude lower than at the location of the source(s). Clearly, tracking enough analog particles to acquire a statistically valid response at a single location of interest through such a shield is beyond the capability of any current computing system. Methods to bias the simulation in a manner that only follows the particles of interest for a given response of interest while still playing a fair statistical game have long been employed in the MC method to make certain shielding analyses feasible. However, for problems with very high attenuation or where the solution is needed at numerous locations (e.g., over an axial height of a few feet around the entire azimuthal extent of the RV/clad interface region of the HFIR), even the traditional methods of MC biasing can be inadequate.

Fortunately, over the last several years, hybrid methodologies that combine the strengths of both the deterministic and stochastic transport methodologies have been developed. One such methodology is the CADIS technique . This technique combines the ability of deterministic transport methods to easily obtain a global solution to the transport equation (in either forward or adjoint form) with the high fidelity problem representations of stochastic transport methods.

When the adjoint form of the Boltzmann transport equation is to be solved, the adjoint source is specified as a desired response function (e.g., energy-dependent flux-to-dose or flux-to-dpa conversion factors) over a given detector location. The resulting adjoint flux in each spatial cell/energy group then represents the relative importance of the flux in that cell/group to the desired response. Calculation of a high-fidelity adjoint flux with a discrete ordinates solver will suffer from the same limitations as the forward flux calculation. Fortunately, a fairly coarse estimate of the adjoint flux is generally sufficient to create adequate biasing parameters for an accelerated MC calculation. These adjoint-driven biasing parameters enable the MC simulation to track more particles that are important to the desired response and eliminate computational time and effort that would otherwise be wasted tracking particles with no impact on the desired response.

While the CADIS methodology enables certain deep penetration shielding analyses, there are scenarios where additional automation and biasing capabilities would be beneficial. For example, if a single response such as the dpa rate is desired at a few detector locations for a single source configuration, then

one could conceivably use a brute-force method of setting up one MC model and a few deterministic models, one for each adjoint source, and creating biasing parameters from each of the individual deterministic models by hand. This process would quickly become intractable if responses were required at more than a few detector locations and/or if multiple source configurations (e.g., at multiple times in life) were to be analyzed. Even for the simplest case, with just a single source and detector, independent deterministic and stochastic models of the same geometry must still be built.

The ADVANTG code has been developed to automate implementation of the CADIS methodology. ADVANTG automates coupling of the ORNL deterministic transport code Denovo and the Los Alamos National Labs (LANL) stochastic transport code, MCNP. To use ADVANTG, the user first creates an MCNP model of the desired geometry. This model is then run in eigenvalue or KCODE mode to generate a fixed-source representation of the core neutron source distribution. ADVANTG then uses the MCNP analysis model and fixed-source description, along with a small number of user-definable modeling parameters (many of which default to reasonable values) to (1) build a discretized Denovo input model, (2) run the Denovo adjoint, and (3) if requested, forward, flux solution(s), and generate a set of biasing parameters from the deterministic flux solution(s). The files with these biasing parameters are then added to the original MCNP input file as a replacement for the eigenvalue-mode source description, and the resulting MCNP input deck is then run in either neutron-only or coupled neutron-gamma transport mode to generate the desired responses at the desired detector locations.

The CADIS methodology implemented in ADVANTG works well for models containing multiple distributed sources and an arbitrary number of detector locations where the response at the different detectors can be reasonably expected to be similar. When the various expected detector responses may be significantly different (e.g., one location with a line-of-sight view of the core and one location where structural material such as a beam tube may obstruct the view of the core), or for global solutions in which many detector locations are near the core and many are far from the core [20], the ADVANTG code can implement an augmented version of the CADIS methodology with a technique known as Forward-Weighted CADIS (FW-CADIS). In this technique, the adjoint-biased source parameters for each detector location are multiplied by the inverse of the expected response at that location (i.e., they are divided by the forward flux at that location). Thus, the number of simulated particles driven to each detector location is roughly constant. Therefore, a single MC calculation can be biased to obtain statistically valid results at multiple detector locations where the expected response can vary dramatically while still playing a fair statistical game.

Figure 3.1-1 presents a view of the simplified 3D Denovo geometry automatically generated by ADVANTG from the more exact MCNP geometry seen in Figs. 3.2-1 through 3.2-10. The discretized geometric representation for deterministic transport codes like Denovo that use orthogonal rectilinear grids will always exhibit the stair-stepped representation of curved surfaces seen in Fig. 3.1-1, and the level of discretization needed for radiation transport analyses conducted entirely with a deterministic code would typically be much finer. To achieve sufficient accuracy, a 3D deterministic model covering the same limited portion of HFIR as that shown in Fig. 3.1-1 could easily require 100 million or more mesh cells, as well as several hundred or more discrete scattering angles and several dozen to a few hundred energy groups. By contrast, the model depicted in Fig. 3.1-1 is constructed from slightly less than 1.3 million total mesh cells and uses only 10 angles per octant for a total of 80 angles over a unit sphere. A total of 47 neutron and 19 gamma groups were used in the Denovo calculation of the forward and adjoint fluxes used by ADVANTG to generate the MCNP biased sources.

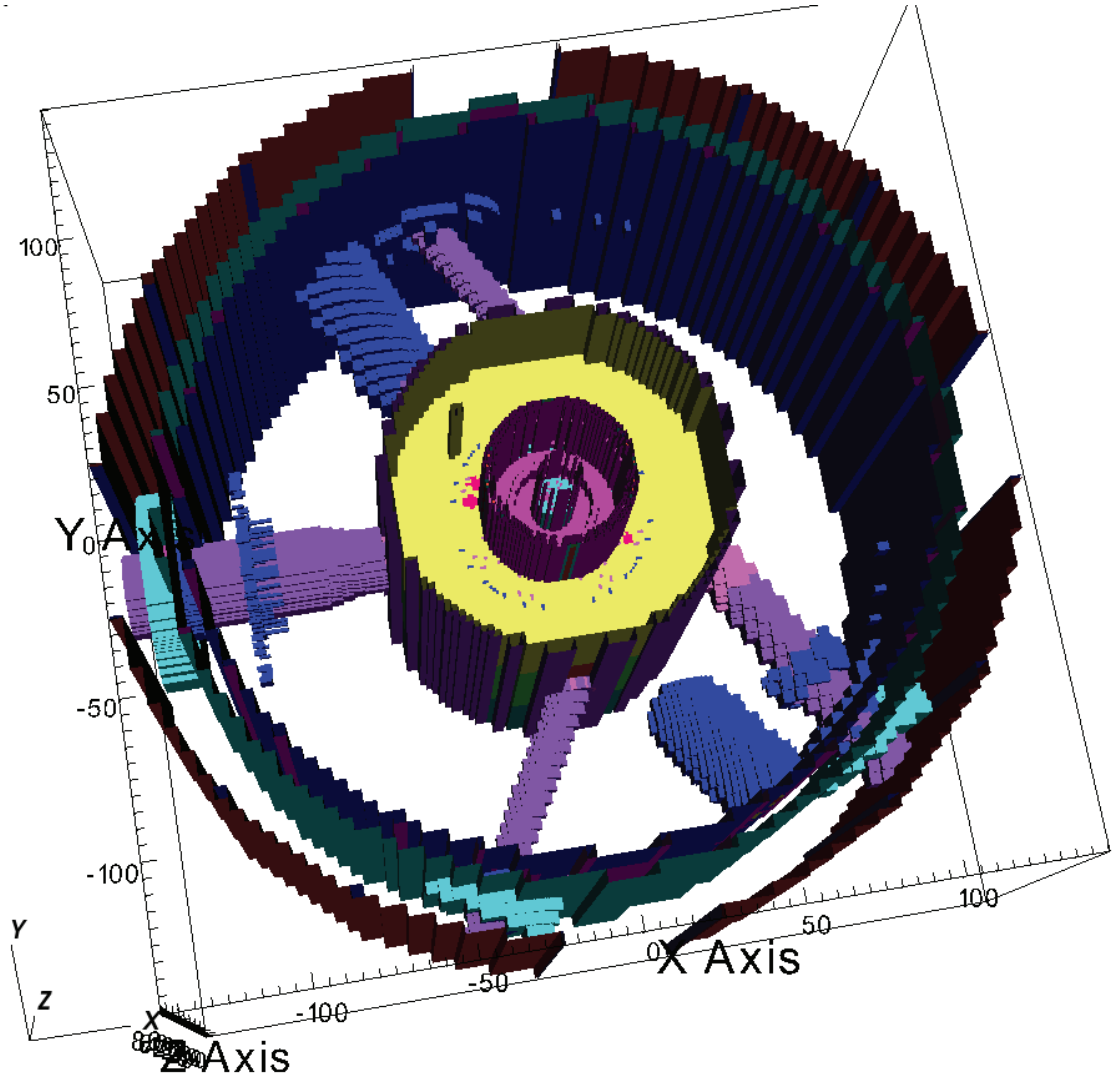

Fig. 3.1-1. Discretized Denovo model for weight windows generation.

3.1.2 Depletion Methods

The transport methods described above are well suited for steady state calculations in which the material compositions and power densities are constant. This approach is valid for determining flux or reaction rate densities at a specific time in life. However, to obtain accurate fluxes throughout the useful lifetime of a core, the transport calculations must be coupled to depletion calculations. For the proposed LEU core design of Ilas and Primm [1], the VESTA [21] code was used to generate depleted material compositions at 25 time steps. As described in Ilas and Primm [1], VESTA can be used to couple a variety of transport codes, including MCNP, to the ORIGEN2.2 [22] depletion code. However, because highly detailed and validated 3D MCNP models existed for prior HFIR HEU analyses [23], these models were used in VESTA as the starting point to develop the proposed LEU core design of Ilas and Primm [1]. Material compositions from the first (BOC) and last time (EOC) steps of the Ilas and Primm [1] design study have been used for the current LEU RV dpa rate analyses.

The material compositions and corresponding power profiles generated for the Ilas and Primm [1] design study represent an improvement over those available for previous depletion studies, because VESTA

allows for the depletion of both in-core and ex-core components. The use of MCNP models in VESTA also allows control element motion throughout life to be easily incorporated into the analysis. VESTA is currently linked to the evaluated nuclear data file (ENDF)/B-VII.0 nuclear cross section data. Although newer (ENDF/B-VII.1) nuclear data are available, the ENDF/B-VII.0 data are the currently approved data set for HFIR safety-basis calculations.

3.2 MODELS

3.2.1 Overview

The models used in the current evaluation are derived from the HFIR version 4.0 (V4.0) models of Xoubi and Primm [19]. The Xoubi and Primm models were, in turn, derived from earlier models, referred to internally as HFIR-V.2. The HFIR-V.2 models were originally developed by J. C. Gehin, L. A. Smith, and J. A. Bucholz. These models were all developed for general core analyses. The models of Xoubi and Primm were subsequently modified for shielding analyses by adding detail to the pressure vessel region of the model and incorporating an updated cores source specification.

The initial LEU shielding analysis models were created by E. D. Blakeman. The Blakeman modifications of the V4.0 base model were focused on two major areas. The first modification was to add or revise geometric features important to the calculation of damage rates in the pressure vessel and at numerous dosimetry locations. This included (1) modifications to beam tubes HB-2 and HB-4 to incorporate the larger diameter tubes installed after 22.7 effective full power years (EFPYs) of HFIR operations, (2) addition of several tubular dosimeters, (3) incorporation of additional detail in several existing dosimeter locations, (4) the use of the most current as-built information (e.g., slight shifts of beam tubes HB-1 and HB-4 in their outer pressure tubes), and (5) updates to some material definitions. The second major change to the V4.0 base model involved incorporating the V4.1 core descriptions of Ilas and Primm [1]. Both BOC and EOC configurations were generated for the existing HEU and proposed LEU cores. The final Blakeman modifications resulted in models acceptable for any number of shielding analyses, including assessment of the neutron and/or gamma flux at various dosimetry locations, or various response functions, such as dpa rates in the RV.

Additional modifications to the Blakeman HEU shielding models were made by J. M. Risner [2]. In this analysis, the shielding models were split into several independent geometric “universes” to allow for easier viewing and debugging of the models. This modular approach to model construction facilitates bulk changes to a specific region of the geometry, such as the core, by simply referencing the files containing the appropriate set of universes in a job stream. The shielding models were then incorporated into an ADVANTG analysis.

3.2.2 Geometry

Modifications analogous to those made to the HEU models by Risner [2] were made to the Blakeman LEU shielding models and are the focus of this report. Except for the core and inner flux trap (IFT) descriptions, the HEU and LEU models are nearly identical. The HEU model contains a few additional tally cells near the seam and girth welds that are not included in the LEU mode, but this does not affect the results at the reactor vessel. The LEU and HEU models use different control element withdrawal curves to position the control elements throughout core life.

Within the IFT, the models differ only in the compositions placed in several of the target locations. The HEU model is based on HFIR cycle 400, in which the sample cells are primarily filled with aluminum plugs. For the proposed LEU core design, the sample irradiation locations in the IFT were filled with curium targets. Within the core region, both the HEU and LEU models are divided into 323 distinct

regions. However, the radial and axial extents, the material composition, and the fission density assigned to each of these regions are quite different. Plan and elevation views of the HFIR LEU analysis geometry are presented in Figs. 3.2-1 and 3.2-2, respectively. More detailed views of the areas highlighted in these figures are presented in Figs. 3.2-3 through 3.2-10.

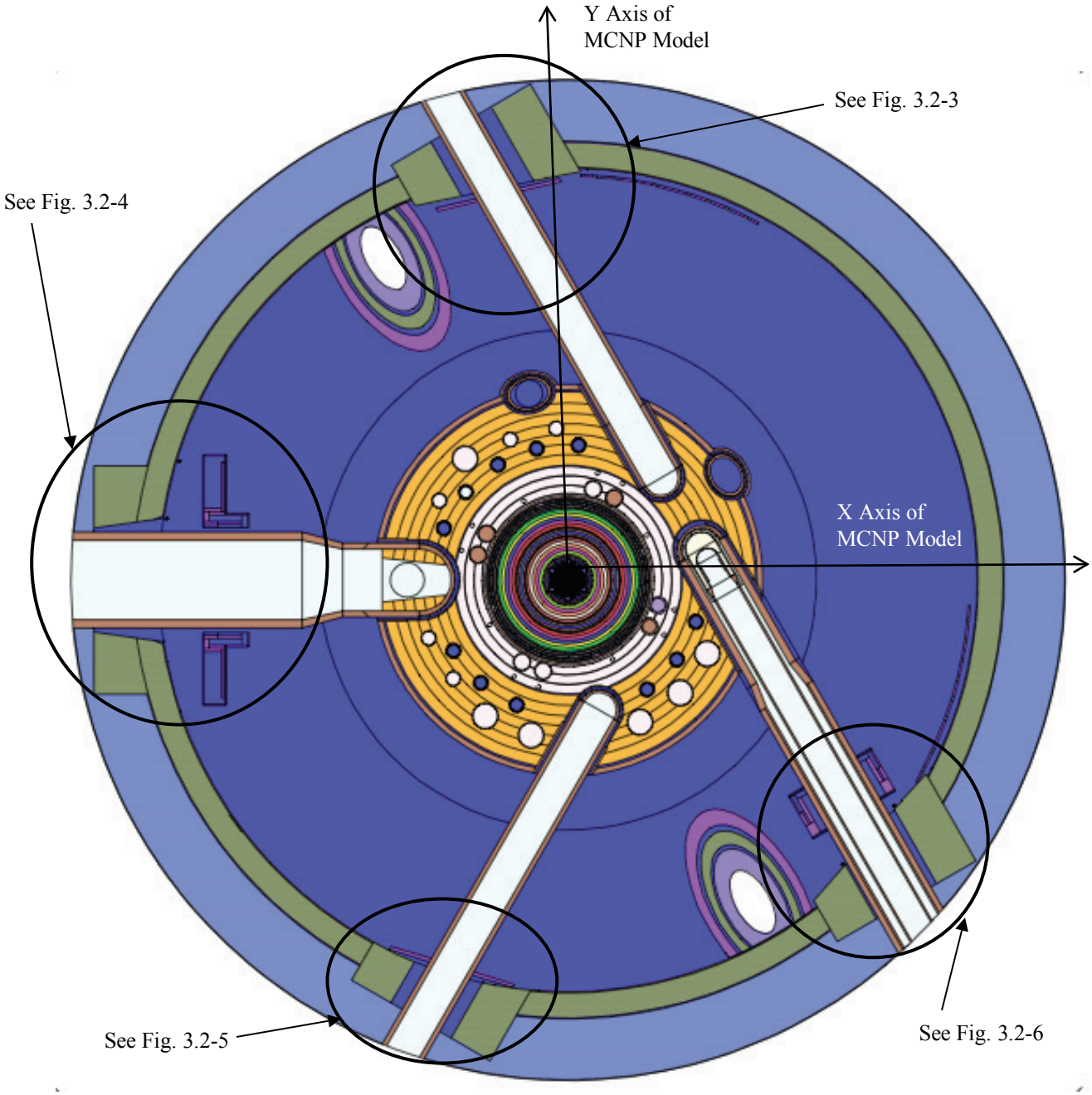

Fig. 3.2-1. Plan view (XY plane at Z=0 cm) through the axial centerline of the HFIR LEU core. Highlighted regions around beam tubes HB-1 through HB-4 are shown in more detail in Figs. 3.2-3 through 3.2-6 and Figs. 3.2-8 and 3.2-10.

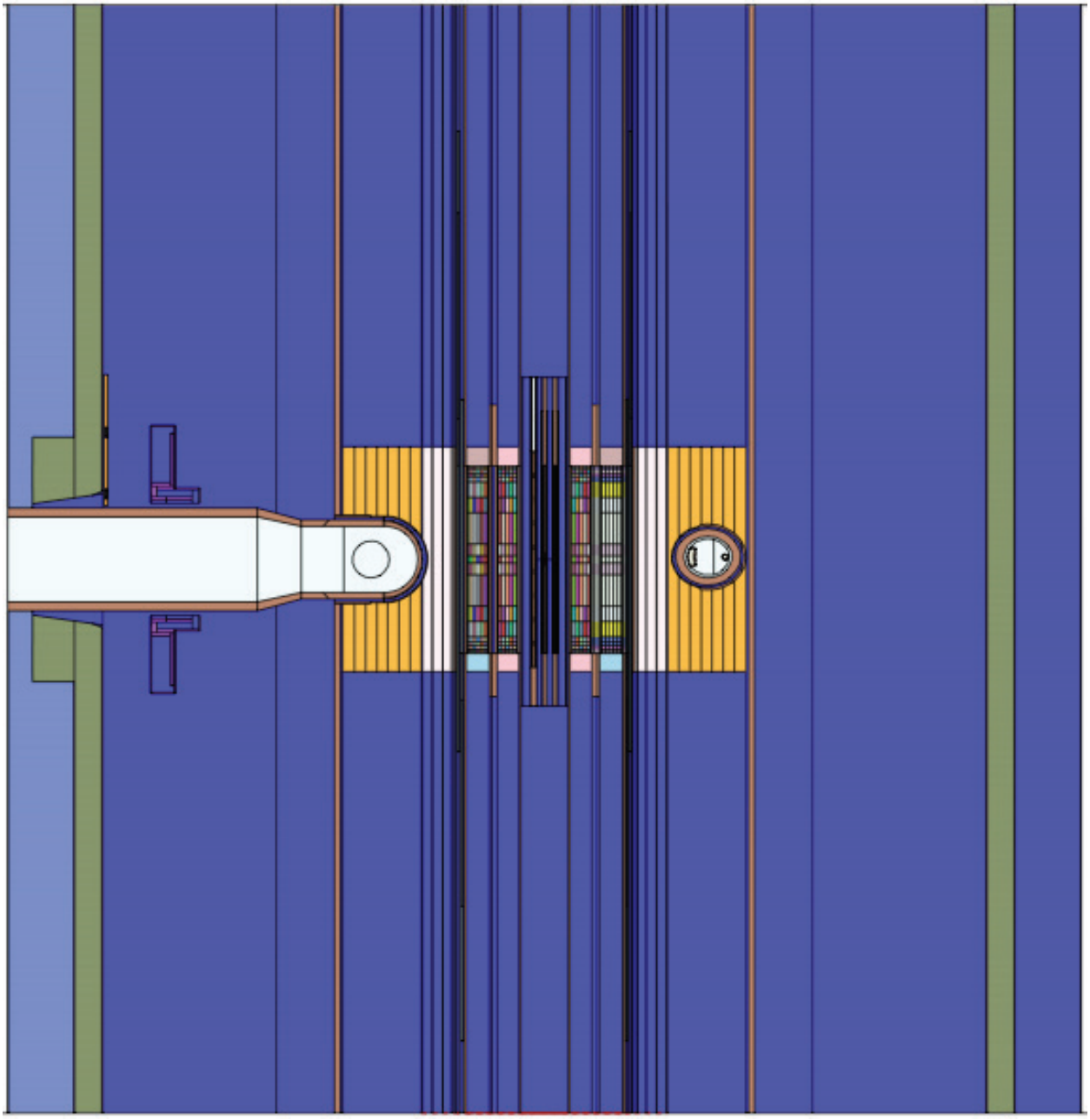

Fig. 3.2-2. Elevation view (XZ plane at Y=0 cm) through radial centerline of core and beam tube HB-2. Core region is shown in more detail in Fig. 3.2-7. RV dosimetry is shown in more detail in Figs. 3.2-4 and 3.2-10.

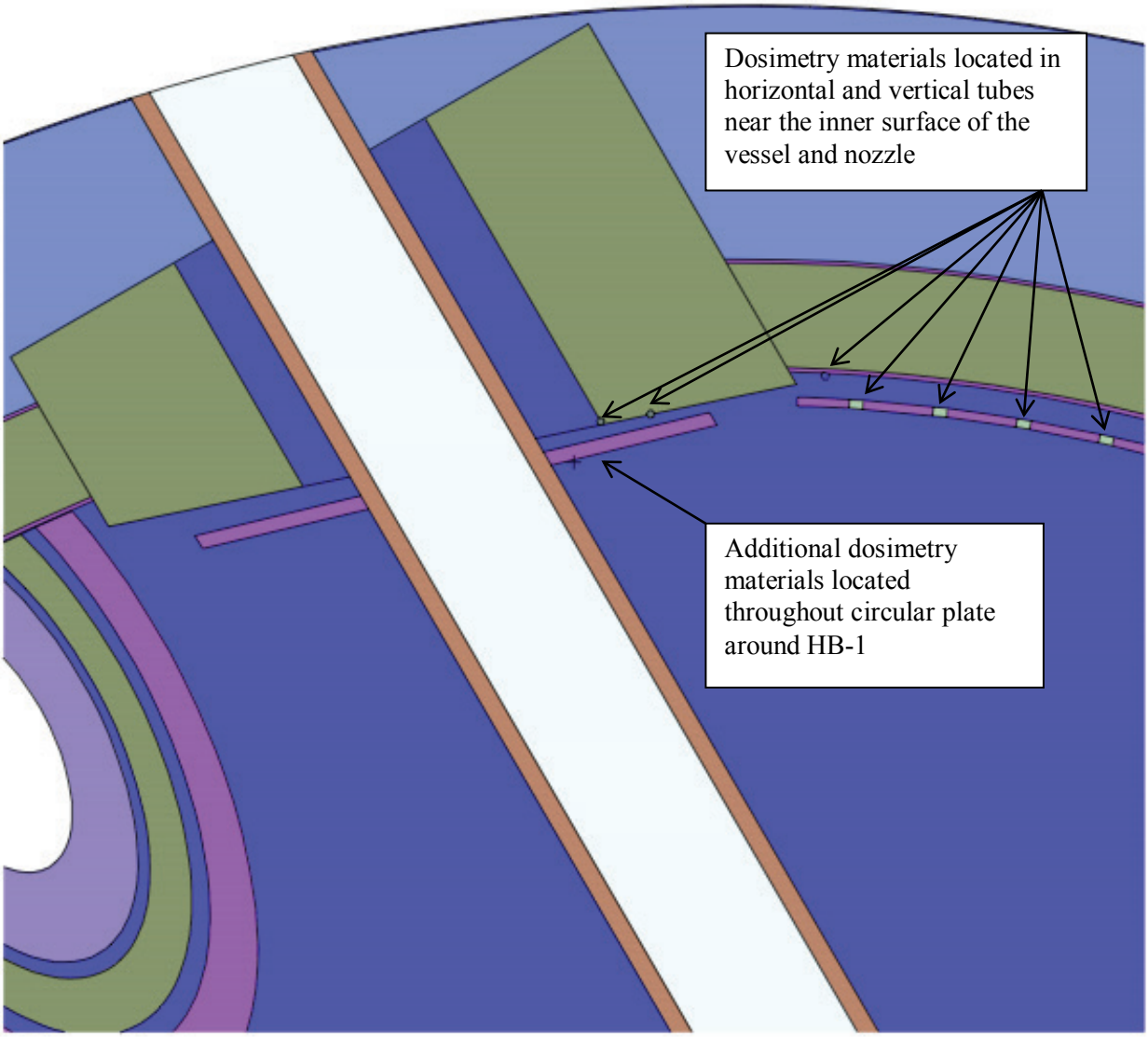

Fig. 3.2-3. Plan (XY plane at Z=0 cm) view showing detail of dosimetry location around beam tube HB-1.

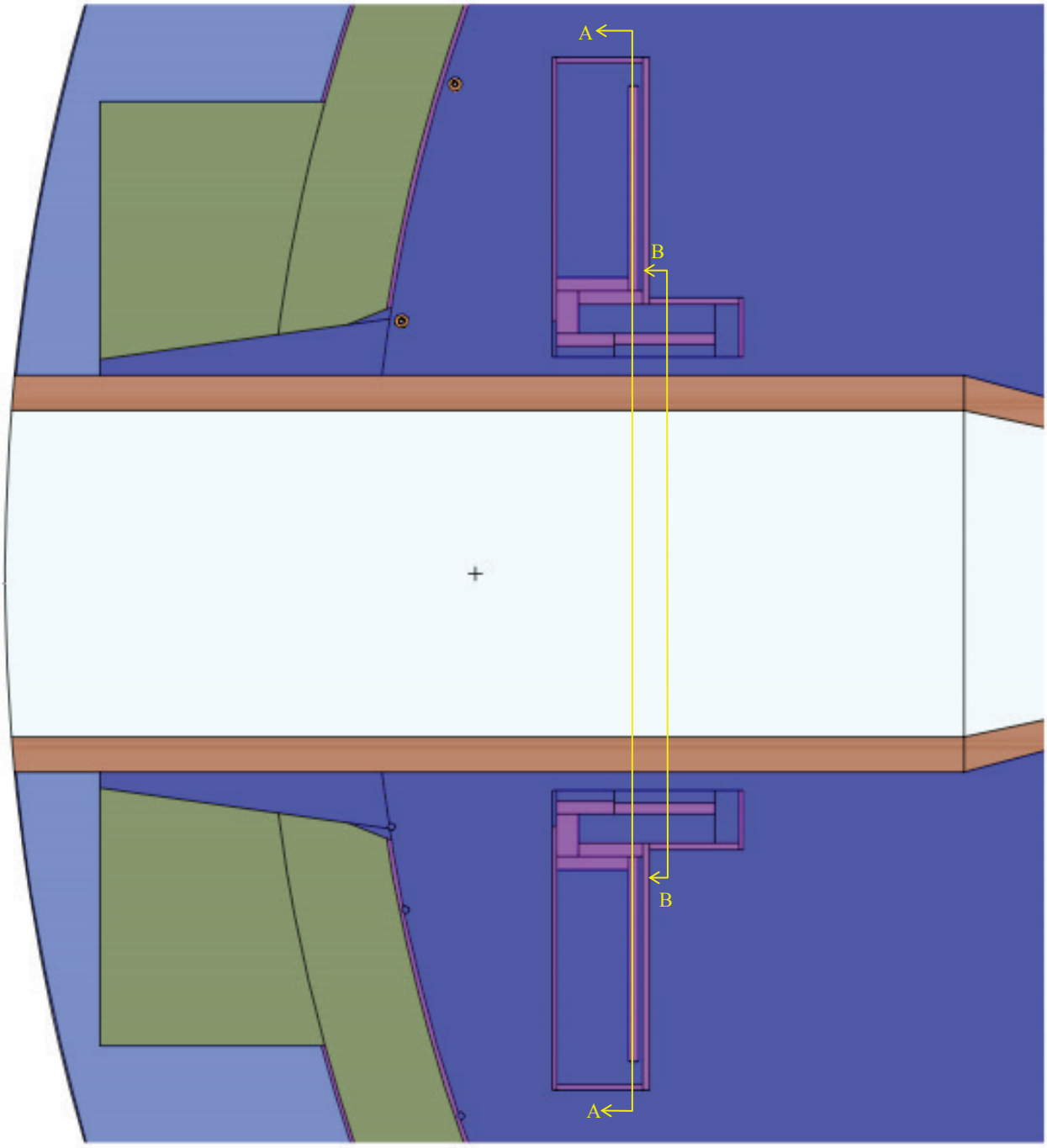

Fig. 3.2-4. Plan view (XY plane at Z=0 cm) showing detail of dosimetry locations around beam tube HB-2.
Sects. A-A and B-B are shown in Figs. 3.2-8 and 3.2-9, respectively.

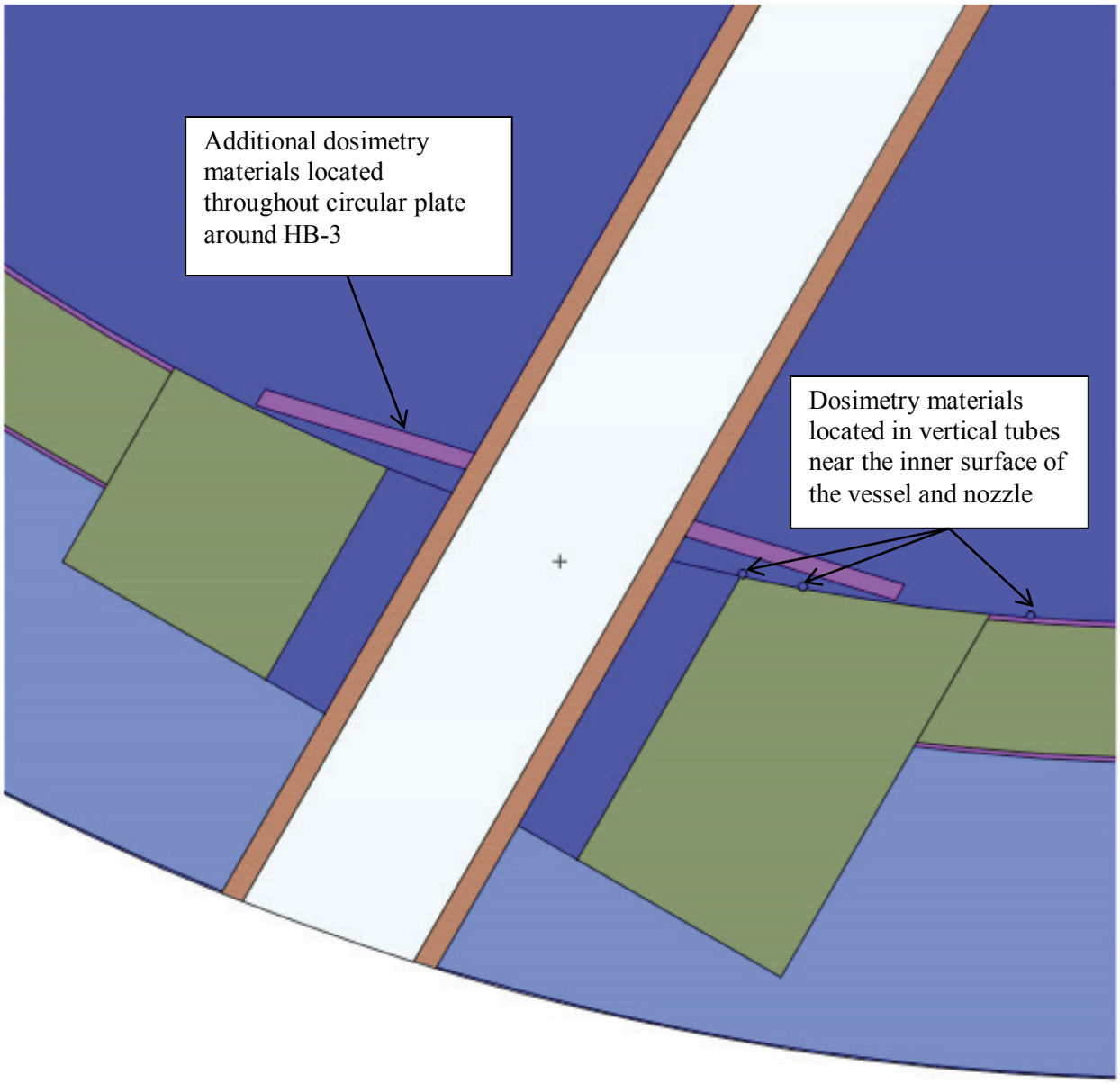

Fig. 3.2-5. Plan view (XY plane at Z=0 cm) showing detail of dosimetry locations around beam tube HB-3.

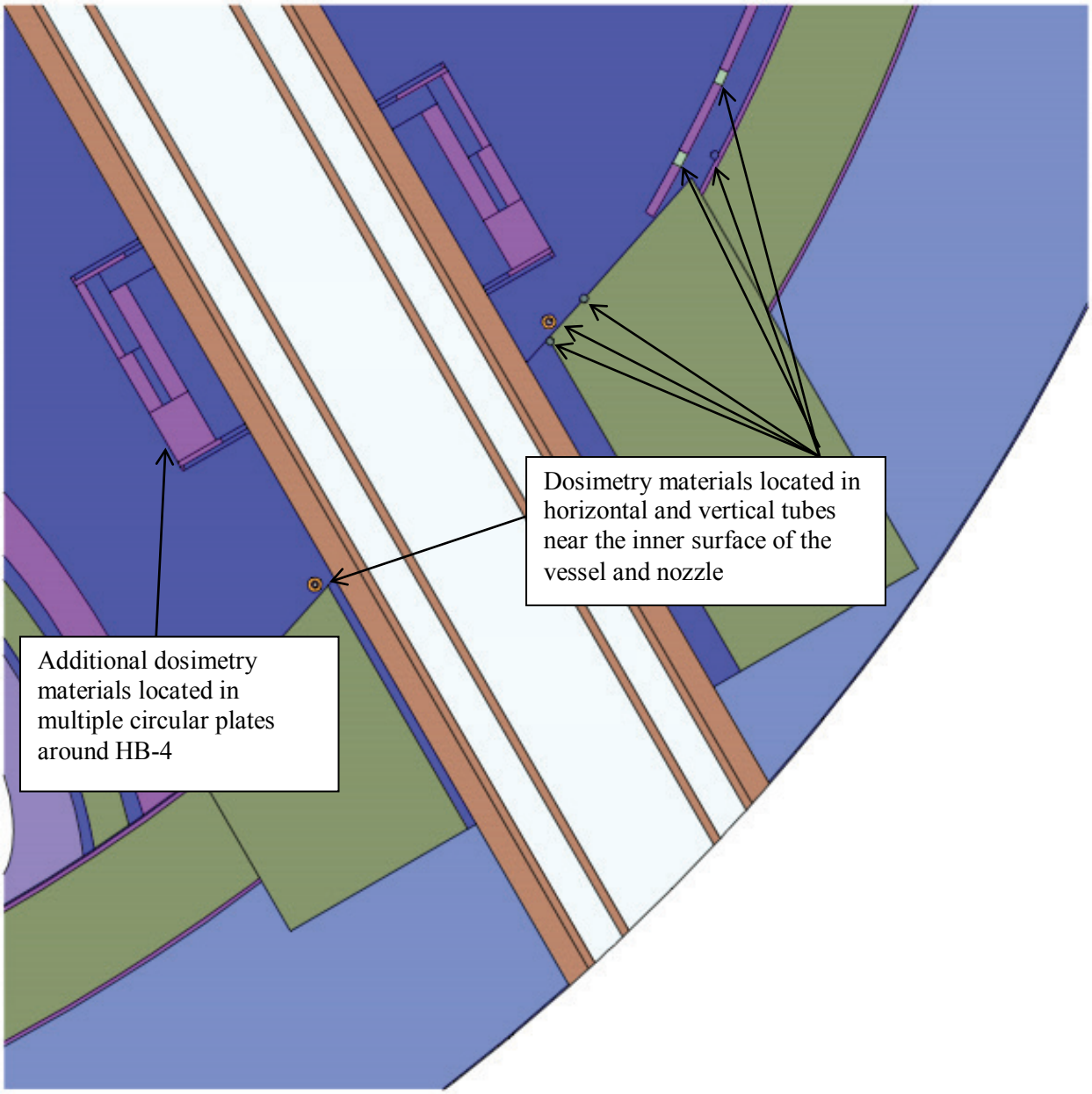

Fig. 3.2-6. Plan view (XY plane at Z=0 cm) showing detail of dosimetry locations around beam tube HB-4.

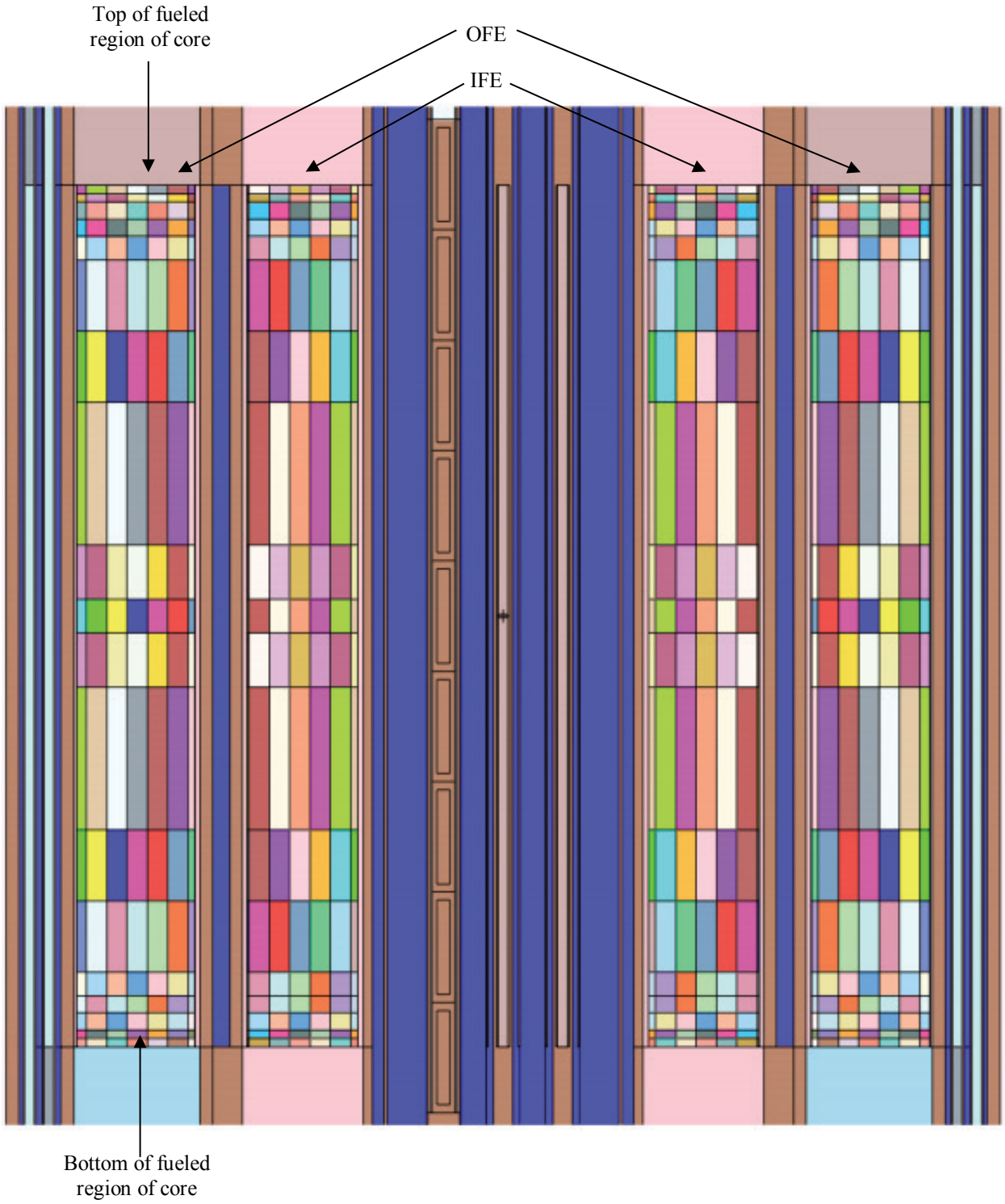

Fig. 3.2-7. Elevation view (XZ plane at Y=0 cm) through core radial centerline (BOC model).

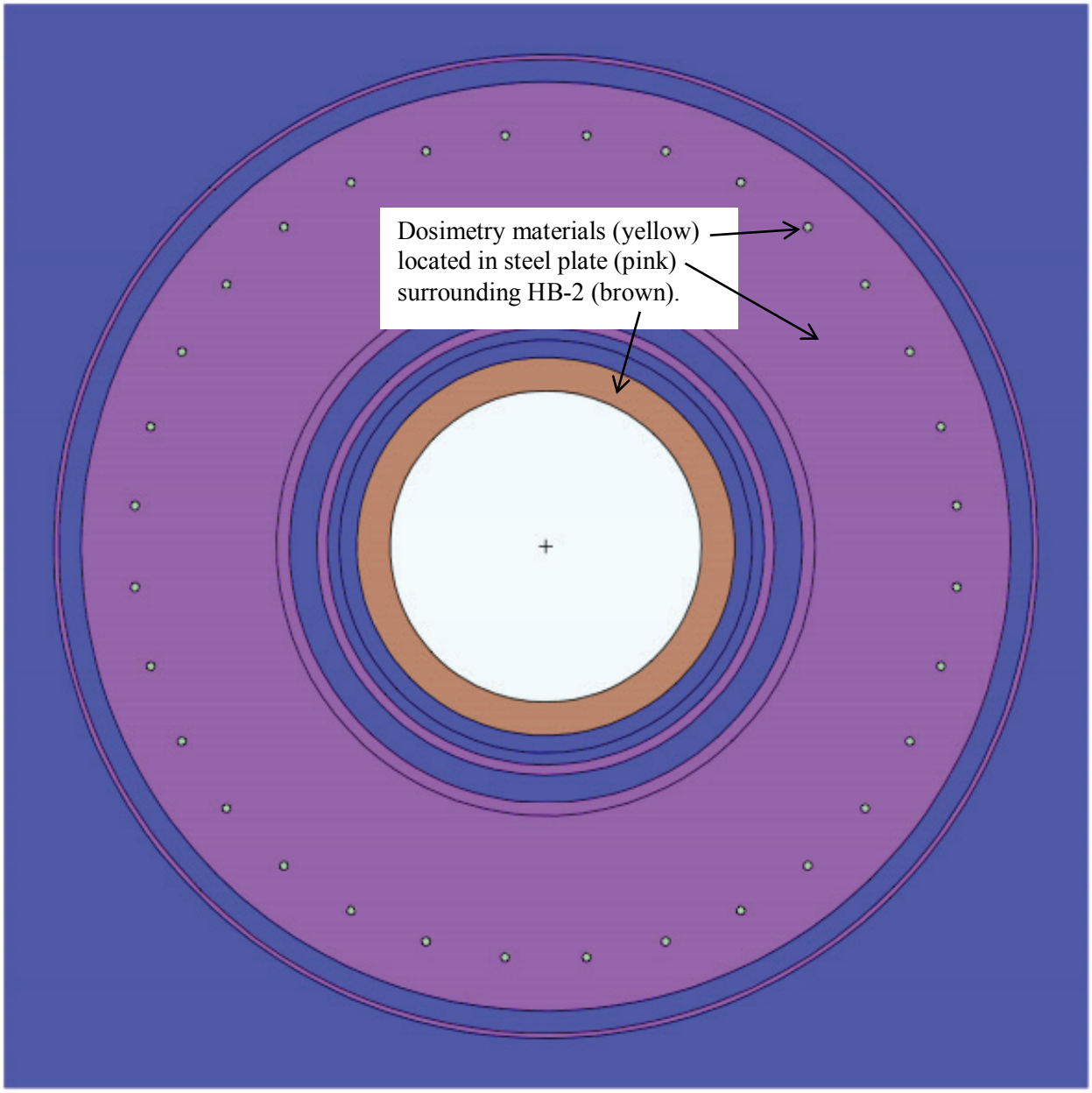

Fig. 3.2-8. Elevation view (YZ plane at X = -100.863 cm) showing dosimetry details around beam tube HB-2 (section A-A of Fig. 3.2-4).

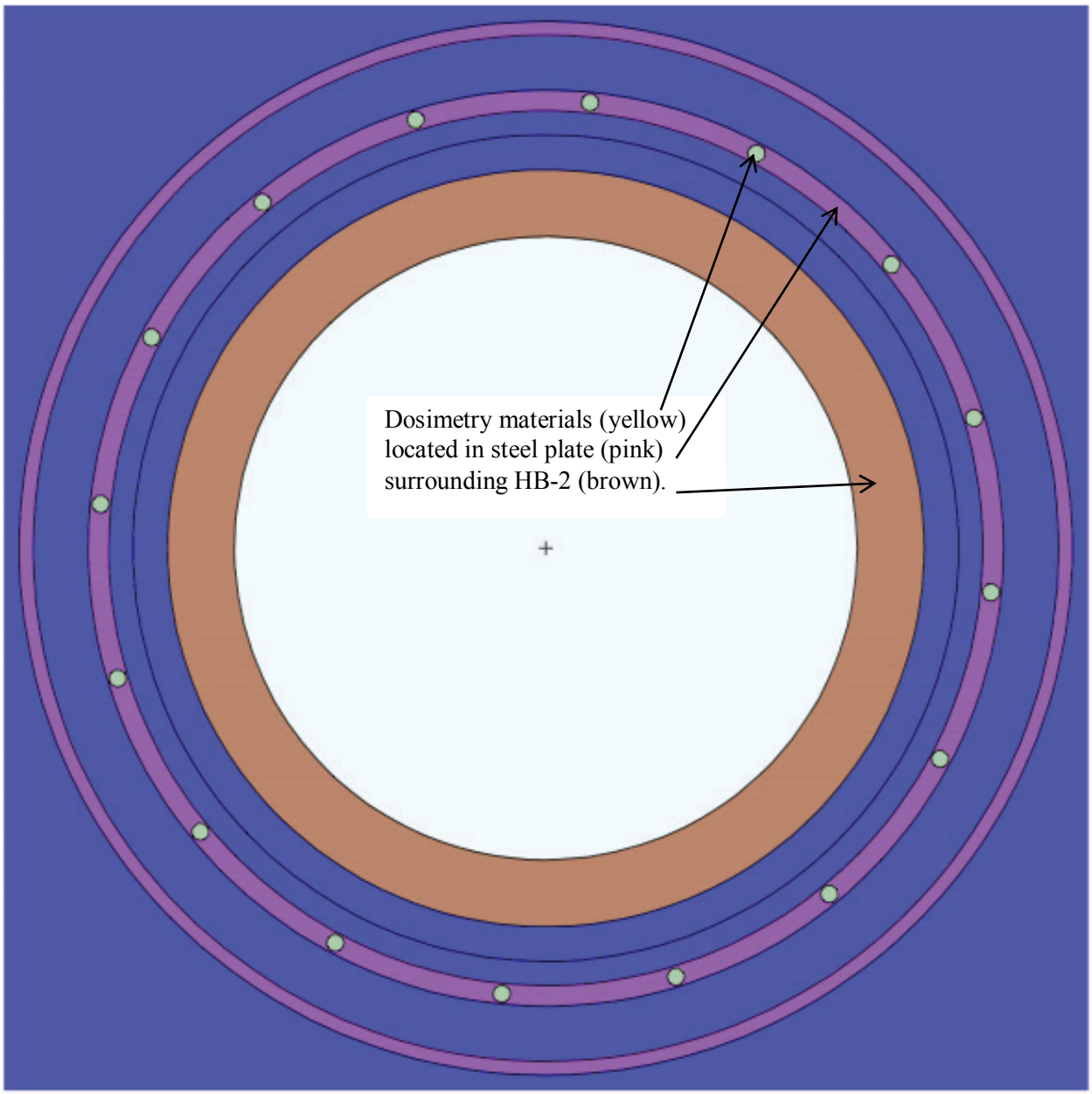

Fig. 3.2-9. Elevation view (YZ plane at X = -98.9076 cm) showing dosimetry details around beam tube HB-2 (section B-B of Fig. 3.2-4).

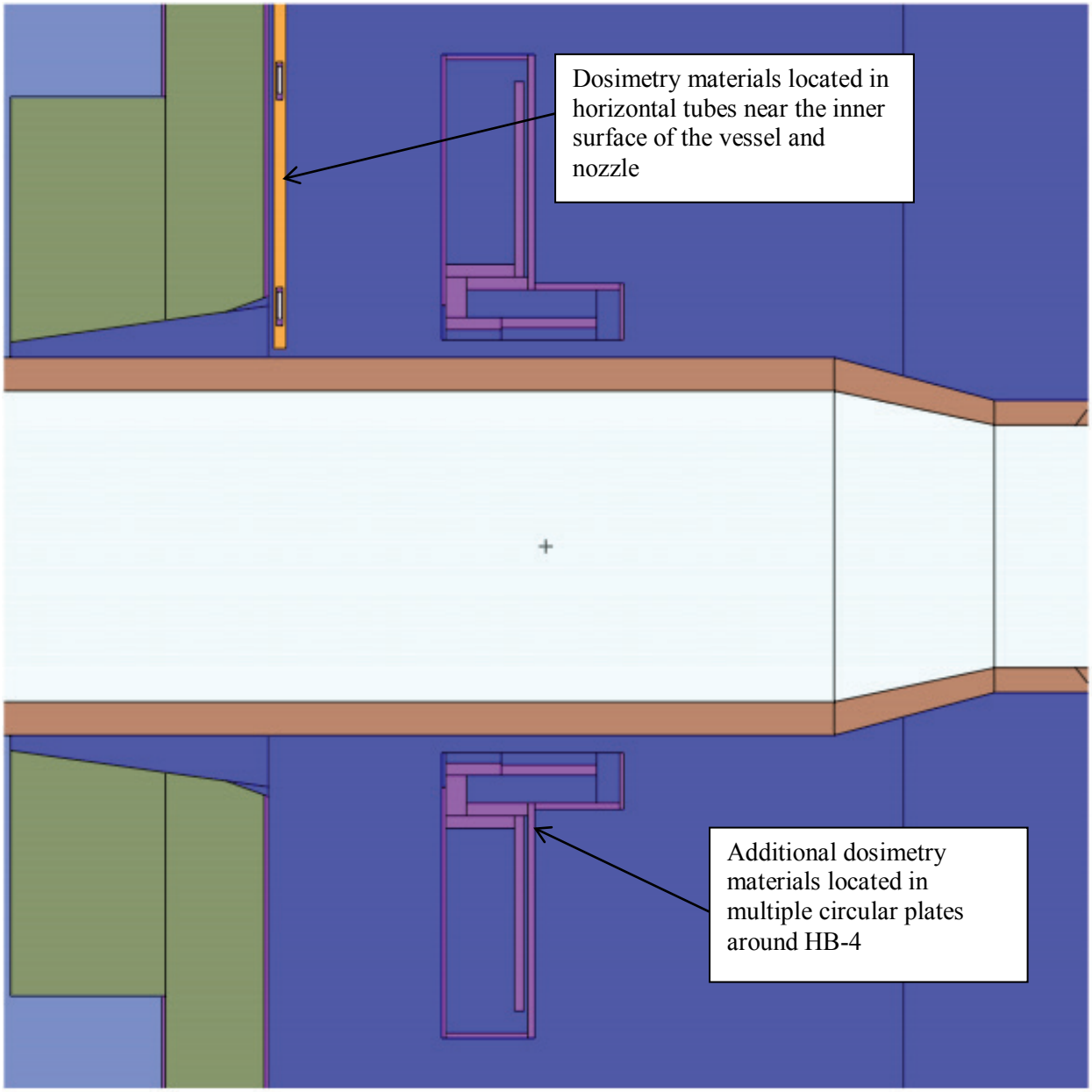

Fig. 3.2-10. Elevation view (XZ plane at Y=0 cm) showing dosimetry details around beam tube HB-2.

Figures 3.2-3 through 3.2-6 are plan views at the axial midplane of the core showing the details of the in situ dosimetry located around beam tubes HB-1 through HB-4, respectively. Figure 3.2-7 is an elevation view through the core radial midplane showing details of the radial and axial zoning of the proposed LEU core. As seen in Fig. 3.2-7, both the inner fuel element (IFE) and outer fuel element (OFE) are split into 19 axial zones. Each of these 19 axial zones are split into 8 radial zones in the IFE, while the OFE is split into 9 radial zones for a total of 323 core regions to which a unique material composition and source strength are assigned. While several unique homogenized source regions are assigned similar colors in Fig. 3.2-7, this is simply due to a limit on the number of unique colors available in the MCNP color palette. Each of the 323 source regions displayed in Fig. 3.2-7 are actually assigned unique material composition and source strength data. Table 3.2-1 lists the dimensions of each of these 323 core source

regions, while Table 3.2-2 and Table 3.2-3 list the volumes of the IFE and OFE core source regions, respectively.

Figure 3.2-8 is an elevation view passing through one of the disks containing numerous dosimetry capsules around beam tube HB-2 (section A-A of Fig. 4). Figure 3.2-9 is an elevation view through another disk containing dosimetry capsules around beam tube HB-2 (section B-B of Fig. 3.2-4). Figure 3.2-10 is another elevation view showing the vertical tubular dosimetry near the nozzle where beam tube HB-2 penetrates the RV.

While the LEU and HEU vessel damage analysis models are effectively identical with few exceptions, the analysis by Risner and Blakeman [2] is broader in scope than the vessel damage analysis covered in this report. Therefore, the model has been modified at various dosimetry locations. Several surfaces used in the definition of various tally cells have been added to provide more detailed results for ongoing dosimetry and materials surveillance analyses. These modifications do not affect the results of the RV damage analysis.

3.2.3 Materials

The materials used in the HFIR LEU RV damage analysis are consistent with those used in the Ilas and Primm analyses [1], as well as the Risner and Blakeman [2] analyses. Except for the core and the curium targets in the IFT, the HEU and LEU material descriptions are identical. The core, control elements, and curium target material descriptions are essentially equivalent to those developed for the Ilas and Primm [1] design study.

A minor change made to the EOC core material compositions was required due to a difference in nomenclature between VESTA and MCNP. The change only affected the ^{148}Pm and ^{148m}Pm fission product (FP) concentrations, and therefore was only required in the EOC calculations. Both VESTA and MCNP refer to each isotope in a composition by "ZAID," a unique identifier constructed from the atomic number (Z) and the mass number (A) of the subject isotope. The ZAID for most isotopes is obtained by multiplying Z by 1,000 and adding A. Thus, ^{148}Pm, an isotope of the element with Z=61, would have a ZAID of 61148. The ZAID also has an additional identifier to indicate the specific cross section evaluation within the global data library. The difference between VESTA and MCNP is in how metastable states of a given isotope are referenced. The latest ENDF/B-VII.0 cross section data are available in VESTA and MCNP, but the data are referenced differently by each code.

In the current MCNP data libraries, ENDF/B-VII-0 data for the ground state of an isotope at room temperature are referenced by appending a ".70c" identifier to the basic ZAID for an isotope, while a ".03c" identifier is used by VESTA. Thus, for most applications, ^{148}Pm at room temperature would be referenced by MCNP as 61148.70c and as 61148.03c in VESTA. In the current VESTA nomenclature, the ".73c" extension is used to point to data for the metastable state of an isotope, so, ^{148m}Pm would be referenced as 61148.73c by VESTA. For the ENDF/B-VII.0 data in the current MCNP library, the .70c–.73c extensions are used to refer to the ground state cross section data for isotopes at various temperatures, while the metastable states of an isotope are referred to using a scheme in which 400 is added to the ZAID for the ground state of the same isotope. Thus, in MCNP nomenclature, ^{148}Pm at room temperature (~300K) is referenced as 61148.70c, and ^{148m}Pm at room temperature is referenced as 61548.70c. In the current MCNP library, 61148.73c refers to the ENDF/B.VII.0 data for ^{148}Pm at a temperature of 1200K. Prior to using the VESTA-generated EOC composition cards in either the HEU or LEU analyses, all ".03c" extensions were replaced by ".70c" extensions in the Blakeman shielding models. Additionally, the VESTA-generated references to ^{148m}Pm were changed from 61148.73c to 61548.70c.

Table 3.2-1. HFIR LEU homogenized core source region dimensions

IFE radial dimensions		OFE radial dimensions		IFE and OFE axial dimensions		
Zone	**Extent (cm)**	**Zone**	**Extent (cm)**	**Zone**	**Lower boundary (cm)***	**Upper boundary (cm)***
1	7.14 – 7.50	9	15.15 – 15.16	1	24.9	25.4
2	7.50 – 8.50	10	15.16 – 15.50	2	24.4	24.9
3	8.50 – 9.50	11	15.50 – 16.50	3	23.4	24.4
4	9.50 – 10.50	12	16.50 – 17.50	4	22.4	23.4
5	10.50 – 11.50	13	17.50 – 18.50	5	21.0	22.4
6	11.50 – 12.50	14	18.50 – 19.50	6	16.8	21.0
7	12.50 – 12.59	15	19.50 – 20.50	7	12.6	16.8
8	12.59 – 12.60	16	20.50 – 20.99	8	4.2	12.6
		17	20.99 – 21.00	9	1.0	4.2
				10	-1.0	1.0
				11	-4.2	-1.0
				12	-12.6	-4.2
				13	-16.8	-12.6
				14	-21.0	-16.8
				15	-22.4	-21.0
				16	-23.4	-22.4
				17	-24.4	-23.4
				18	-24.9	-24.4
				19	-25.4	-24.9

*Relative to the core axial midplane, which is located at 0 cm in the model coordinate system

Table 3.2-2. IFE homogenized source region volumes (cm^3)

	Radial zones							
Axial zones	**1**	**2**	**3**	**4**	**5**	**6**	**7**	**8**
1	8.279	25.133	28.274	31.416	34.558	37.699	3.547	0.396
2	8.279	25.133	28.274	31.416	34.558	37.699	3.547	0.396
3	16.557	50.265	56.549	62.832	69.115	75.398	7.094	0.791
4	16.557	50.265	56.549	62.832	69.115	75.398	7.094	0.791
5	23.180	70.372	79.168	87.965	96.761	105.558	9.932	1.108
6	69.541	211.115	237.504	263.894	290.283	316.673	29.795	3.324
7	69.541	211.115	237.504	263.894	290.283	316.673	29.795	3.324
8	139.083	422.230	475.009	527.788	580.566	633.345	55.590	6.647
9	52.984	160.850	180.956	201.062	221.168	241.274	22.701	2.532
10	33.115	100.531	113.097	125.664	138.230	150.796	14.188	1.583
11	52.984	160.850	180.956	201.062	221.168	241.274	22.701	2.532
12	139.083	423.230	475.009	527.788	580.566	633.345	59.590	6.647
13	69.541	211.115	237.504	263.894	290.283	316.673	29.795	3.324
14	69.541	211.115	237.504	263.894	290.283	316.673	29.795	3.324
15	23.180	70.372	79.168	87.965	96.761	105.558	9.932	1.108
16	16.557	50.265	56.549	62.832	69.115	75.398	7.094	0.791
17	16.557	50.265	56.549	62.832	69.115	75.398	7.094	0.791
18	8.279	25.133	28.274	31.416	34.558	37.699	3.547	0.396
19	8.279	25.133	28.274	31.416	34.558	37.699	3.547	0.396

Table 3.2-3. OFE homogenized source region volumes (cm^3)

	Radial zones								
Axial zones	**1**	**2**	**3**	**4**	**5**	**6**	**7**	**8**	**9**
1	0.476	16.375	50.265	53.407	56.549	56.690	62.832	31.934	0.660
2	0.476	16.375	50.265	53.407	56.549	56.690	62.832	31.934	0.660
3	0.952	32.749	100.531	106.814	113.097	119.381	125.664	63.869	1.319
4	0.952	32.749	100.531	106.814	113.097	119.381	125.664	63.869	1.319
5	1.333	45.849	140.743	149.540	158.336	167.133	175.929	89.416	1.847
6	3.999	137.547	422.230	448.619	475.009	501.398	527.788	268.249	5.540
7	3.999	137.547	422.230	448.619	475.009	501.398	527.788	268.249	5.540
8	7.999	275.093	844.460	897.239	950.018	1002.796	1055.575	536.499	11.018
9	3.047	104.797	321.699	341.805	361.911	382.018	402.124	204.380	4.221
10	1.904	65.498	201.062	213.628	226.195	238.761	251.327	127.738	2.638
11	3.047	104.797	321.699	341.805	361.911	382.018	402.124	204.380	4.221
12	7.999	275.093	844.460	897.239	950.018	1002.796	1055.575	536.499	11.081
13	3.999	137.547	422.230	448.619	475.009	501.398	527.788	268.249	5.540
14	3.999	137.547	422.230	448.619	475.009	501.398	527.788	268.249	5.540
15	1.333	45.849	140.743	149.540	158.336	167.133	175.929	89.416	1.847
16	0.952	32.749	100.531	106.814	113.097	119.381	125.664	63.869	1.319
17	0.952	32.749	100.531	106.814	113.097	119.381	125.664	63.869	1.319
18	0.476	16.375	50.265	53.407	56.549	56.690	62.832	31.934	0.660
19	0.476	16.375	50.265	53.407	56.549	56.690	62.832	31.934	0.660

In addition to the ^{148m}Pm modification discussed above, a minor material modification was made to remove the isotope ^{248}Cm from any material containing curium. Initial runs with the LEU model would not execute to completion because a fatal error related to the generation of a negative particle weight occurred. After enabling additional debugging features in MCNP, it was determined that the job abort always occurred on the first particle history that contained an interaction with ^{248}Cm. The reason for this behavior is unknown, but after removing the ^{248}Cm from all material definitions, no further job aborts occurred. Removal of this minor constituent from the target regions in the IFT will have no significant impact on the results at the RV.

3.2.4 Fission Source

A multistep process is followed to create the biased source and variance reduction parameters used to optimize calculation of RV damage rates due to the neutrons and photons released by fission. First, MCNP is run in eigenvalue (KCODE) mode to generate a neutron flux distribution for the desired core condition (e.g., BOC or EOC). In the KCODE run, a mesh tally of the neutron flux in the core regions defined by the dimensions provided in Table 3.2-1 is created. This mesh tally is then processed by a Python script created for the Risner and Blakeman analysis [2] to generate a fixed neutron source description in MCNP source definition (SDEF) format. The original MCNP input file is then modified to include the associated SDEF, source information (SI), source probabilities (SP), and placeholder source bias (SB) cards output by the Python script. This modified file then becomes the MCNP input file used by ADVANTG. ADVANTG will run Denovo (in forward, and if required, adjoint mode[s]) to generate variance reduction parameters (weight windows file, weight-window parameter [WWP] cards, SB cards). ADVANTG will also modify the original input MCNP file to include the WWP cards and replace the placeholder SB cards. This modified MCNP input file produced by ADVANTG is then run as a fixed-source problem in coupled n-γ mode to calculate the RV dpa rates due to fission neutrons, fission photons, and capture photons.

The neutron fluxes in each of the 323 homogenized core source regions that form the basis for the ADVANTG calculations are listed in Tables 3.2-4 through 3.2-7. The average BOC and EOC source strengths for the IFE source regions are presented in Table 3.2-4 and Table 3.2-5, respectively. Similar data for the OFE source regions are presented in Table 3.2-6 and Table 3.2-7.

3.2.5 Fission Product Source

The RV dpa rates due to FP photons, which may also be referred to as delayed gammas, must be calculated separately. Because fission neutrons and FPs are created simultaneously during the fission process, the same spatial distribution can be used by ADVANTG for generating variance reduction parameters for the FP dpa rate calculation that was used for the prompt (fission source) calculation. The changes that must be made to the MCNP input file used by ADVANTG are to specify a photon-only calculation instead of a coupled n-γ calculation and to replace the SI, SP, and placeholder SB energy bin definitions from the coupled n-γ calculation with corresponding values to define the FP photon spectrum.

The energy bin boundaries and corresponding photon yields for the FP photon spectrum are obtained from an ORIGEN-S [22] calculation. The ORIGEN calculation is based on irradiating an arbitrarily small amount of the fissionable isotopes in the core (19.75 wt.% ^{235}U, 80.25 wt.% ^{238}U for LEU) at an arbitrarily low thermal flux. The material mass and thermal flux are chosen so that the fission rate calculated by ORIGEN-S for all time steps is 1 fission/second. This iterative process is the same one used to generate FP photon spectra for the McDuffee [24] analyses.

Table 3.2-4. IFE BOC source strengths by region (neutrons/sec at 100 megawatts (MW)*)

	Radial zones							
Axial zones	**1**	**2**	**3**	**4**	**5**	**6**	**7**	**8**
1	1.4613+14	1.9238+14	2.2985+14	2.2974+14	2.1855+14	1.9587+14	1.6639+14	1.6742+14
2	1.2628+14	1.4639+14	1.5046+14	1.4137+14	1.3863+14	1.4376+14	1.3928+14	1.4264+14
3	1.1518+14	1.2475+14	1.1841+14	1.0814+14	1.0889+14	1.2142+14	1.2255+14	1.2524+14
4	1.1162+14	1.1829+14	1.0961+14	1.0049+14	1.0212+14	1.1396+14	1.1363+14	1.1596+14
5	1.1392+14	1.2130+14	1.1367+14	1.0499+14	1.0673+14	1.1673+14	1.1345+14	1.1517+14
6	1.3046+14	1.4005+14	1.3287+14	1.2407+14	1.2586+14	1.3430+14	1.2774+14	1.2933+14
7	1.5913+14	1.7097+14	1.6249+14	1.5209+14	1.5425+14	1.6367+14	1.5468+14	1.5655+14
8	1.9056+14	2.0499+14	1.9526+14	1.8321+14	1.8635+14	1.9811+14	1.8715+14	1.8923+14
9	2.0579+14	2.2165+14	2.1128+14	1.9859+14	2.0253+14	2.1571+14	2.0381+14	2.0622+14
10	2.0661+14	2.2284+14	2.1246+14	1.9964+14	2.0343+14	2.1663+14	2.0482+14	2.0720+14
11	2.0378+14	2.1947+14	2.0918+14	1.9679+_14	2.0049+14	2.1346+14	2.0187+14	2.0422+14
12	1.8438+14	1.9842+14	1.8891+14	1.7711+14	1.8008+14	1.9135+14	1.8076+14	1.8286+14
13	1.4981+14	1.6079+14	1.5237+14	1.4236+14	1.4421+14	1.5312+14	1.4486+14	1.4665+14
14	1.2164+14	1.2961+14	1.2182+14	1.1323+14	1.1501+14	1.2339+14	1.1810+14	1.1967+14
15	1.0616+14	1.1254+14	1.0568+14	9.8070+13	1.0014+14	1.1094+14	1.0906+14	1.1125+14
16	1.0476+14	1.1419+14	1.0498+14	1.0344+14	1.0556+14	1.0761+14	1.0143+14	1.0213+14
17	1.1019+14	1.0549+14	7.8702+13	7.4667+13	7.4556+13	8.1203+13	8.0864+13	7.8142+13
18	9.8844+13	7.0669+13	5.4294+13	4.8118+13	4.6946+13	5.2983+13	6.3797+13	6.6154+13
19	1.1359+14	8.9165+13	7.3073+13	6.5792+13	6.3150+13	6.6127+13	7.3523+13	7.5603+13

*1.4613+13 = 1.4132×10^{13}

Table 3.2-5. OFE BOC source strengths by region (neutrons/sec at 100 MW*)

	Radial zones								
Axial zones	**1**	**2**	**3**	**4**	**5**	**6**	**7**	**8**	**9**
1	1.7632+14	1.8097+14	2.0446+14	1.9447+14	1.6902+14	1.5254+14	1.1615+14	6.8856+13	5.1521+13
2	1.4911+14	1.4548+14	1.4045+14	1.1764+14	9.9525+13	9.2515+13	7.8356+31	5.4195+13	4.3470+13
3	1.2975+14	1.2629+14	1.1729+14	9.3569+13	7.8161+13	7.3908+13	6.5365+13	4.7619+13	3.9112+13
4	1.2005+14	1.1729+14	1.1123+14	9.0138+13	7.5281+13	7.1812+13	6.3687+13	4.6297+13	3.7712+13
5	1.1859+14	1.1747+14	1.1503+14	9.5808+13	8.0515+13	7.7073+13	6.8640+13	4.9796+13	4.0398+13
6	1.3278+14	1.3309+14	1.3432+14	1.1488+14	9.7942+13	9.5959+13	9.1108+13	7.2015+13	6.0258+13
7	1.6069+14	1.6157+14	1.6507+14	1.4313+14	1.2346+14	1.2394+14	1.2537+15	1.0707+14	9.1778+13
8	1.9467+14	1.9605+14	2.0149+14	1.7616+14	1.5420+14	1.5898+14	1.7148+14	1.5736+14	1.3837+14
9	2.1275+14	2.1435+14	2.2103+14	1.9486+14	1.7278+14	1.8448+14	2.1691+14	2.1800+14	1.9716+14
10	2.1356+14	2.1541+14	2.2236+14	1.9624+14	1.7452+14	1.8706+14	2.2230+14	2.2563+14	2.0455+14
11	2.1038+14	2.1200+14	2.1865+14	1.9290+14	1.7121+14	1.8298+14	2.1691+14	2.1855+14	1.9817+14
12	1.8798+14	1.8942+14	1.9444+14	1.6975+14	1.4818+14	1.5215+14	1.6225+14	1.4653+14	1.2773+14
13	1.5037+14	1.5129+14	1.5412+14	1.3309+14	1.1436+14	1.1409+14	1.1415+14	9.5804+13	8.1320+13
14	1.2317+14	1.2296+14	1.2303+14	1.0410+14	8.7934+13	8.4831+13	7.7734+13	5.8748+13	4.8064+13
15	1.1507+14	1.1361+14	1.0983+14	9.0158+13	7.4649+13	6.9101+13	5.5929+13	3.5237+13	2.6932+13
16	1.0630+14	1.1011+14	1.1238+14	9.5572+13	7.9310+13	7.1578+13	5.5680+13	3.3403+13	2.3739+13
17	8.0103+13	9.3964+13	8.8833+13	7.3101+13	6.1686+13	5.3563+13	4.3241+13	3.1082+13	1.9959+13
18	6.6053+13	6.0718+13	4.9335+13	4.0355+13	3.4597+13	2.9454+13	2.4226+13	2.0250+13	1.9136+13
19	7.5053+13	7.0803+13	6.1551+13	5.2751+13	4.5601+13	3.8554+13	3.0794+13	2.4373+13	2.2199+13

*1.7632+13 = 1.7623×10^{13}

Table 3.2-6. IFE EOC source strengths by region (neutrons/sec at 100 MW*)

	Radial zones							
Axial zones	**1**	**2**	**3**	**4**	**5**	**6**	**7**	**8**
1	8.9312+14	4.2610+15	6.1887+15	6.8952+15	7.2651+15	6.9992+15	5.2866+14	6.0050+13
2	8.4551+14	3.6634+15	4.4898+15	4.5531+15	4.8886+15	5.4362+15	4.6233+14	5.3290+13
3	1.6211+15	6.1573+15	7.1594+15	6.9238+15	7.5921+15	9.1647+15	8.2375+14	9.5842+13
4	1.5895+15	6.1945+15	6.5437+15	6.2949+15	6.9608+15	8.4634+15	7.6631+14	8.9426+13
5	2.2679+15	8.8269+15	9.3748+15	9.0907+15	1.0026+16	1.1889+16	1.0589+15	1.2361+14
6	7.4105+15	2.9696+16	3.2298+16	3.1482+16	3.4591+16	3.9944+16	3.4795+15	4.0877+14
7	8.2737+15	3.4794+16	3.8855+16	3.7681+16	4.1207+16	4.6895+16	4.0314+15	4.7841+14
8	1.7830+16	7.9049+16	9.1133+16	8.8111+16	9.5842+16	1.0822+17	9,1995+15	1.0998+15
9	6.9647+15	3.1660+16	3.7093+16	3.5797+16	3.8937+16	4.3755+16	3.7034+15	4.4462+14
10	4.3500+15	1.9861+16	2.3314+16	2.2501+16	2.4456+16	2.7487+16	2.3218+15	2.7887+14
11	6.9306+15	3.1520+16	3.6922+16	3.5661+16	3.8734+16	4.3534+16	3.6834+15	4.4192+14
12	1.7450+16	7.7780+16	8.9592+16	8.6599+16	9.4368+16	1.0644+17	9.0552+15	1.0830+15
13	8.0191+15	3.3694+16	3.7606+16	3.6450+16	3.9864+16	4.5465+16	3.9108+15	4.6412+14
14	7.2183+15	2.8793+16	3.1084+16	3.0148+16	3.3165+16	3.8637+16	3.3919+15	3.9893+14
15	2.2525+15	8.8043+15	9.4368+15	9.1678+15	1.0194+16	1.2309+16	1.1044+15	1.2912+14
16	1.6250+15	6.6011+15	7.1213+15	7.4792+15	8.2798+15	8.9894+15	7.5414+14	8.6297+13
17	1.6860+15	6.0777+15	5.5547+15	5.8141+15	6.2789+15	7.0297+15	6.0663+14	6.5412+13
18	7.0951+14	1.8828+15	1.7974+15	1.8035+15	1.9233+15	2.2300+15	2.3156+14	2.6705+13
19	7.4185+14	2.0726+15	2.1030+15	2.1770+15	2.3180+15	2.5560+15	2.5312+14	2.9059+13

*8.9312+14 = 8.9312×10^{14}

Table 3.2-7. OFE EOC source strengths by region (neutrons/sec at 100 MW*)

	Radial zones								
Axial zones	**1**	**2**	**3**	**4**	**5**	**6**	**7**	**8**	**9**
1	7.6223+13	2.7084+15	1.0196+16	1.1019+16	1.0821+16	1.1501+16	1.1410+16	4.4077+15	6.7299+13
2	6.6937+13	2.2577+15	7.1800+15	6.6891+15	6.3642+15	7.0222+15	8.2586+15	3.9134+15	7.2635+13
3	1.1921+14	3.9375+15	1.1829+16	1.0391+16	9.7315+15	1.1140+16	1.4517+16	7.6094+15	1.4527+14
4	1.1121+14	3.6533+15	1.1059+16	9.8441+15	9.2524+15	1.0751+16	1.4539+16	7.8384+15	1.5096+14
5	1.5344+14	5.0556+15	1.5792+16	1.4482+16	1.3696+16	1.5975+16	2.1666+16	1.1675+16	2.2463+14
6	5.0552+14	1.6644+16	5.3652+16	5.0419+16	4.8031+16	5.6094+16	7.4581+16	3.9544+16	7.5549+14
7	5.9024+14	1.9303+16	6.3273+16	5.9984+16	5.7208+16	6.6903+16	8.9093+16	4.4539+16	8.3712+14
8	1.3608+15	4.4079+16	1.4611+17	1.3877+17	1.3246+17	1.5527+17	2.0535+17	9.8290+16	1.8214+15
9	5.4972+14	1.7745+16	5.9167+16	5.6201+16	5.3628+16	6.2924+16	8.2941+16	3.8961+16	7.1955+14
10	3.4499+14	1.1131+16	3.7131+16	3.5349+16	3.3681+16	3.9538+16	5.2115+16	2.4418+16	4.5039+14
11	5.4660+14	1.7661+16	5.8853+16	5.5957+16	5.3352+16	6.2659+16	8.2647+16	3.8838+16	7.1754+14
12	1.3398+15	4.3374+16	1.4388+17	1.3661+17	1.3033+17	1.5291+17	2.0265+17	9.7179+16	1.8023+15
13	5.7228+14	1.8708+16	6.1349+16	5.8084+16	5.5424+16	6.4980+16	8.7060+16	4.3728+16	8.2246+14
14	4.9460+14	1.6230+16	5.1845+16	4.8346+16	4.6064+16	5.4017+16	7.3640+16	3.9018+16	7.4733+14
15	1.6140+14	5.2845+15	1.6269+16	1.4710+16	1.3937+16	1.6264+16	2.2097+16	1.1916+16	2.2989+14
16	1.0639+13	3.7341+15	1.2345+16	1.1705+16	1.1155+16	1.2666+16	1.5888+16	7.9337+15	1.4173+14
17	7.8256+13	3.1352+15	9.7920+17	2.2592+15	9.0786+15	9.8638+15	1.1752+16	6.4561+15	1.0357+14
18	3.0623+13	9.7066+14	2.5951+17	2.4604+15	2.4669+15	2.6044+15	3.0049+15	1.8094+15	4.1938+13
19	3.3456+13	1.0845+15	3.0732+17	3.0458+15	3.0950+15	3.2264+15	3.5151+15	1.9407+15	4.3108+13

*7.6223+13 = 7.6223 x 10^{13}

Therefore, the power-by-time-step input from the McDuffee [24] input files was used as an initial guess for the current analysis, and the ^{235}U and ^{238}U initial masses were set to the same order of magnitude as those used in the McDuffee [24] analyses but were modified slightly to represent the appropriate isotopic ratios corresponding to the LEU core enrichment. Based on the calculated fission rates with these inputs, the power level at the first time step was modified by a ratio of 1/P (where P represents the calculated fission rate at the first time step), and ORIGEN-S was run again. Based on the results from this modified ORIGEN-S calculation, an updated value for the power at the second time step was determined. This process was repeated until input power levels at all time steps had been modified to yield a fission rate of 1 fission/second.

After a fission rate of 1 fission/second has been achieved for all time steps, the final calculated spectrum (photons/sec in each energy group) will represent the number of photons emitted per fission. This value of γ's/fission is then used in conjunction with the operating power of the reactor and a factor to convert power to fission rate (3.11×10^{10} fissions/Watt-sec) to generate the normalization factor that is applied to the MCNP to generate a dpa rate tally.

Once the new spectrum has been provided, ADVANTG is run to generate variance reduction parameters appropriate for this source, and the new ADVANTG-modified MCNP input file is run to calculate the RV dpa rates due to the FP photons. The FP photon spectrum calculated for the LEU core at BOC is presented in Table 3.2-8. For comparison, the HEU FP photon spectrum developed by McDuffee [24] and used in the Risner and Blakeman [2] calculation is also presented in Table 3.2-8. The LEU and HEU FP photon spectra for EOC are presented in Table 3.2-9.

3.2.6 Other

The calculation of vessel damage requires a detailed knowledge of the energy-dependent particle flux at the locations of interest. A corresponding energy-dependent response function is also required to convert the particle flux into an energy-integrated parameter, such as dpa, that can be correlated to a specific material effect, such as radiation-induced embrittlement. Separate energy group structures are used for the calculation of dpa induced by neutrons and photons. The neutron and photon displacement cross sections for iron have been obtained from ASTM Standard E693-12 [25] and Baumann [26], respectively. The energy group boundaries of the ASTM 640-group neutron displacement cross section for iron are presented in Table 3.2-10. The corresponding cross sections are presented in Table 3.2-11. The point-wise photon displacement cross sections as a function of energy are presented in Table 3.2-12. These response functions are identical to those presented in Appendix A of Risner and Blakeman [2].

Table 3.2-8. BOC FP photon energy spectra

Group	Energy (MeV)	LEU FP	HEU FP*	Group	Energy (MeV)	LEU FP	HEU FP
	E_{low} - E_{high}	γ/fission	γ/fission		E_{low} - E_{high}	γ/fission	γ/fission
1	0.00E+00 - 5.00E-03	0.3473	0.3409	30	4.54E-01 - 4.81E-01	0.1512	0.1508
2	5.00E-03 - 5.70E-03	0.1529	0.1505	31	4.81E-01 - 5.35E-01	0.2165	0.2150
3	5.70E-03 - 6.30E-03	0.2244	0.2205	32	5.35E-01 - 5.62E-01	0.1803	0.1800
4	6.30E-03 - 8.00E-03	0.2668	0.2622	33	5.62E-01 - 5.89E-01	7.043e-02	0.6992
5	8.00E-03 - 1.13E-02	0.3419	0.4246	34	5.89E-01 - 6.16E-01	0.2303	0.2296
6	1.13E-02 - 1.45E-02	0.3167	0.2841	35	6.16E-01 - 6.70E-01	0.2298	0.2288
7	1.45E-02 - 1.78E-02	0.3212	0.3177	36	6.70E-01 - 7.24E-01	0.1775	0.1765
8	1.78E-02 - 2.11E-02	0.2335	0.2291	37	7.24E-01 - 7.78E-01	0.2311	0.2302
9	2.11E-02 - 2.43E-02	0.1711	0.1684	38	7.78E-01 - 8.32E-01	0.1939	0.1930
10	2.43E-02 - 2.76E-02	9.434e-02	9.306E-02	39	8.32E-01 - 5.59E-01	0.1881	0.1876
11	2.76E-02 - 3.08E-02	0.2053	0.2027	40	5.59E-01 - 9.13E-01	0.2167	0.2161
12	3.08E-02 - 3.41E-02	0.2003	0.1984	41	9.13E-01 - 9.67E-01	0.1918	0.1915
13	3.41E-02 - 4.06E-02	0.1981	0.1963	42	9.67E-01 - 1.05E+00	0.2390	0.2382
14	4.06E-02 - 4.72E-02	0.1768	0.1704	43	1.05E+00 - 1.13E+00	0.1673	0.1671
15	4.72E-02 - 6.02E-02	0.1902	0.1875	44	1.13E+00 - 1.24E+00	0.1727	0.1720
16	6.02E-02 - 7.50E-02	0.2300	0.1993	45	1.24E+00 - 1.37E+00	0.2109	0.2101
17	7.50E-02 - 1.02E-01	0.3955	0.3664	46	1.37E+00 - 1.45E+00	0.2520	0.2521
18	1.02E-01 - 1.29E-01	0.2686	0.2523	47	1.45E+00 - 1.70E+00	0.1919	0.1913
19	1.29E-01 - 1.56E-01	0.2255	0.2239	48	1.70E+00 - 2.00E+00	0.2026	0.2022
20	1.56E-01 - 1.83E-01	0.2527	0.2510	49	2.00E+00 - 2.50E+00	0.2167	0.2161
21	1.83E-01 - 2.10E-01	0.2038	0.2019	50	2.50E+00 - 3.00E+00	0.1347	0.1344
22	2.10E-01 - 2.37E-01	0.1275	0.1237	51	3.00E+00 - 4.00E+00	9.786e-02	9.769E-02
23	2.37E-01 - 2.64E-01	0.2057	0.2053	52	4.00E+00 - 5.00E+00	3.227e-02	3.227E-02
24	2.64E-01 - 2.91E-01	0.1105	0.1061	53	5.00E+00 - 6.00E+00	9.639e-03	9.649E-03
25	2.91E-01 - 3.18E-01	0.1942	0.1929	54	6.00E+00 - 7.00E+00	1.297e-03	1.297E-03
26	3.18E-01 - 3.72E-01	0.2090	0.2068	55	7.00E+00 - 8.00E+00	2.759e-05	2.759E-05
27	3.72E-01 - 3.99E-01	0.1650	0.1644	56	8.00E+00 - 9.00E+00	4.423e-02	4.373E-07
28	3.99E-01 - 4.27E-01	0.1004	0.1003	57	9.00E+00 - 1.00E+01	1.465e-08	1.452E-08
29	4.27E-01 - 4.54E+01	0.1495	0.1487				

*Fission product photon spectrum data are from McDuffee [24].

Table 3.2-9. EOC FP photon energy spectra

Group	Energy (MeV) E_{low} - E_{high}	LEU FP γ/fission	HEU FP* γ/fission	Group	Energy (MeV) E_{low} - E_{high}	LEU FP γ/fission	HEU FP γ/fission
1	0.00E+00 - 5.00E-03	0.4037	0.3888	30	4.54E-01 - 4.81E-01	0.1528	0.1509
2	5.00E-03 - 5.70E-03	0.1693	0.1666	31	4.81E-01 - 5.35E-01	0.2984	0.2928
3	5.70E-03 - 6.30E-03	0.2448	0.2389	32	5.35E-01 - 5.62E-01	0.1958	0.1983
4	6.30E-03 - 8.00E-03	0.2898	0.2834	33	5.62E-01 - 5.89E-01	7.144E-02	6.999E-02
5	8.00E-03 - 1.13E-02	0.4677	0.4580	34	5.89E-01 - 6.16E-01	0.2294	0.2313
6	1.13E-02 - 1.45E-02	0.4325	0.3130	35	6.16E-01 - 6.70E-01	0.3100	0.3075
7	1.45E-02 - 1.78E-02	0.3373	0.3322	36	6.70E-01 - 7.24E-01	0.1892	0.1870
8	1.78E-02 - 2.11E-02	0.2710	0.2487	37	7.24E-01 - 7.78E-01	0.3379	0.3376
9	2.11E-02 - 2.43E-02	0.1860	0.1811	38	7.78E-01 - 8.32E-01	0.2088	0.2106
10	2.43E-02 - 2.76E-02	0.1016	9.896E-02	39	8.32E-01 - 5.59E-01	0.1885	0.1888
11	2.76E-02 - 3.08E-02	0.2579	0.2546	40	5.59E-01 - 9.13E-01	0.2227	0.2216
12	3.08E-02 - 3.41E-02	0.2274	0.2278	41	9.13E-01 - 9.67E-01	0.2012	0.2037
13	3.41E-02 - 4.06E-02	0.2407	0.2408	42	9.67E-01 - 1.05E+00	0.2439	0.2437
14	4.06E-02 - 4.72E-02	0.1994	0.1871	43	1.05E+00 - 1.13E+00	0.1653	0.1685
15	4.72E-02 - 6.02E-02	0.2213	0.2138	44	1.13E+00 - 1.24E+00	0.1766	0.1766
16	6.02E-02 - 7.50E-02	0.2672	0.2104	45	1.24E+00 - 1.37E+00	0.2125	0.2149
17	7.50E-02 - 1.02E-01	0.4849	0.4149	46	1.37E+00 - 1.45E+00	0.2468	0.2552
18	1.02E-01 - 1.29E-01	0.3519	0.2627	47	1.45E+00 - 1.70E+00	0.2363	0.2383
19	1.29E-01 - 1.56E-01	0.2916	0.2891	48	1.70E+00 - 2.00E+00	0.2007	0.2038
20	1.56E-01 - 1.83E-01	0.2646	0.2630	49	2.00E+00 - 2.50E+00	0.21178	0.2167
21	1.83E-01 - 2.10E-01	0.2157	0.2086	50	2.50E+00 - 3.00E+00	0.1316	0.1354
22	2.10E-01 - 2.37E-01	0.1805	0.1591	51	3.00E+00 - 4.00E+00	9.377E-02	9.726E-02
23	2.37E-01 - 2.64E-01	0.2100	0.2102	52	4.00E+00 - 5.00E+00	3.015E-02	3.211E-02
24	2.64E-01 - 2.91E-01	0.1386	0.1105	53	5.00E+00 - 6.00E+00	8.964E-03	9.602E-03
25	2.91E-01 - 3.18E-01	0.2190	0.2118	54	6.00E+00 - 7.00E+00	1.215E-03	1.290E-03
26	3.18E-01 - 3.72E-01	0.2589	0.2452	55	7.00E+00 - 8.00E+00	2.554E-05	2.745E-05
27	3.72E-01 - 3.99E-01	0.1661	0.1661	56	8.00E+00 - 9.00E+00	4.216E-07	4.353E-07
28	3.99E-01 - 4.27E-01	0.1015	0.1024	57	9.00E+00 - 1.00E+01	1.392E-08	1.445E-08
29	4.27E-01 - 4.54E+01	0.1544	0.1531				

*Fission product photon spectrum data is from McDuffee [24].

Table 3.2-10. Neutron energy group boundaries for the 640-group ASTM neutron dpa cross sections

Boundary numbers			Energy group boundaries (MeV)					
1	to	6	1.000E-10	1.050E-10	1.100E-10	1.150E-10	1.200E-10	1.275E-10
7	to	12	1.350E-10	1.425E-10	1.500E-10	1.600E-10	1.700E-10	1.800E-10
13	to	18	1.900E-10	2.000E-10	2.100E-10	2.200E-10	2.300E-10	2.400E-10
19	to	24	2.550E-10	2.700E-10	2.800E-10	3.000E-10	3.200E-10	3.400E-10
25	to	30	3.600E-10	3.800E-10	4.000E-10	4.250E-10	4.500E-10	4.750E-10
31	to	36	5.000E-10	5.250E-10	5.500E-10	5.750E-10	6.000E-10	6.300E-10
37	to	42	6.600E-10	6.900E-10	7.200E-10	7.600E-10	8.000E-10	8.400E-10
43	to	48	8.800E-10	9.200E-10	9.600E-10	1.000E-09	1.050E-09	1.100E-09
49	to	54	1.150E-09	1.200E-09	1.275E-09	1.350E-09	1.425E-09	1.500E-09
55	to	60	1.600E-09	1.700E-09	1.800E-09	1.900E-09	2.000E-09	2.100E-09
61	to	66	2.200E-09	2.300E-09	2.400E-09	2.550E-09	2.700E-09	2.800E-09
67	to	72	3.000E-09	3.200E-09	3.400E-09	3.600E-09	3.800E-09	4.000E-09
73	to	78	4.250E-09	4.500E-09	4.750E-09	5.000E-09	5.250E-09	5.500E-09
79	to	84	5.750E-09	6.000E-09	6.300E-09	6.600E-09	6.900E-09	7.200E-09
85	to	90	7.600E-09	8.000E-09	8.400E-09	8.800E-09	9.200E-09	9.600E-09
91	to	96	1.000E-08	1.050E-08	1.100E-08	1.150E-08	1.200E-08	1.275E-08
97	to	102	1.305E-08	1.425E-08	1.500E-08	1.600E-08	1.700E-08	1.800E-08
103	to	108	1.900E-08	2.000E-08	2.100E-08	2.200E-08	2.300E-08	2.400E-08
109	to	114	2.550E-08	2.700E-08	2.800E-08	3.000E-08	3.200E-08	3.400E-08
115	to	120	3.600E-08	3.800E-08	4.000E-08	4.250E-08	4.500E-08	4.750E-08
121	to	126	5.000E-08	5.250E-08	5.500E-08	5.750E-08	6.000E-08	6.300E-08
127	to	132	6.600E-08	6.900E-08	7.200E-08	7.600E-08	8.000E-08	8.400E-08
133	to	138	8.800E-08	9.200E-08	9.600E-08	1.000E-07	1.050E-07	1.100E-07
139	to	144	1.150E-07	1.200E-07	1.275E-07	1.350E-07	1.425E-07	1.500E-07
145	to	150	1.600E-07	1.700E-07	1.800E-07	1.900E-07	2.000E-07	2.100E-07
151	to	156	2.200E-07	2.300E-07	2.400E-07	2.550E-07	2.700E-07	2.800E-07
157	to	162	3.000E-07	3.200E-07	3.400E-07	3.600E-07	3.800E-07	4.000E-07
163	to	168	4.250E-07	4.500E-07	4.750E-07	5.000E-07	5.250E-07	5.500E-07
169	to	174	5.750E-07	6.000E-07	6.300E-07	6.600E-07	6.900E-07	7.200E-07
175	to	180	7.600E-07	8.000E-07	8.400E-07	8.800E-07	9.200E-07	9.600E-07
181	to	186	1.000E-06	1.050E-06	1.100E-06	1.150E-06	1.200E-06	1.275E-06
187	to	192	1.350E-06	1.425E-06	1.500E-06	1.600E-06	1.700E-06	1.800E-06
193	to	198	1.900E-06	2.000E-06	2.100E-06	2.200E-06	2.300E-06	2.400E-06
199	to	204	2.550E-06	2.700E-06	2.800E-06	3.000E-06	3.200E-06	3.400E-06
205	to	210	3.600E-06	3.800E-06	4.000E-06	4.250E-06	4.500E-06	4.750E-06
211	to	216	5.000E-06	5.250E-06	5.500E-06	5.750E-06	6.000E-06	6.300E-06
217	to	222	6.600E-06	6.900E-06	7.200E-06	7.600E-06	8.000E-06	8.400E-06
223	to	228	8.800E-06	9.200E-06	9.600E-06	1.000E-05	1.050E-05	1.100E-05

Table 3.2-11. Neutron energy group boundaries for the 640-group ASTM neutron dpa cross sections (continued)

Boundary numbers			Energy group boundaries (MeV)					
229	to	234	1.150E-05	1.200E-05	1.275E-05	1.350E-05	1.425E-05	1.500E-05
235	to	240	1.600E-05	1.700E-05	1.800E-05	1.900E-05	2.000E-05	2.100E-05
241	to	246	2.200E-05	2.300E-05	2.400E-05	2.550E-05	2.700E-05	2.800E-05
247	to	252	3.000E-05	3.200E-05	3.400E-05	3.600E-05	3.800E-05	4.000E-05
253	to	258	4.250E-05	4.500E-05	4.750E-05	5.000E-05	5.250E-05	5.500E-05
259	to	264	5.750E-05	6.000E-05	6.300E-05	6.600E-05	6.900E-05	7.200E-05
265	to	270	7.600E-05	8.000E-05	8.400E-05	8.800E-05	9.200E-05	9.600E-05
271	to	276	1.000E-04	1.050E-04	1.100E-04	1.150E-04	1.200E-04	1.275E-04
277	to	282	1.350E-04	1.425E-04	1.500E-04	1.600E-04	1.700E-04	1.800E-04
283	to	288	1.900E-04	2.000E-04	2.100E-04	2.200E-04	2.300E-04	2.400E-04
289	to	294	2.550E-04	2.700E-04	2.800E-04	3.000E-04	3.200E-04	3.400E-04
295	to	300	3.600E-04	3.800E-04	4.000E-04	4.250E-04	4.500E-04	4.750E-04
301	to	306	5.000E-04	5.250E-04	5.500E-04	5.750E-04	6.000E-04	6.300E-04
307	to	312	6.600E-04	6.900E-04	7.200E-04	7.600E-04	8.000E-04	8.400E-04
313	to	318	8.800E-04	9.200E-04	9.600E-04	1.000E-03	1.050E-03	1.100E-03
319	to	324	1.150E-03	1.200E-03	1.275E-03	1.350E-03	1.425E-03	1.500E-03
325	to	330	1.600E-03	1.700E-03	1.800E-03	1.900E-03	2.000E-03	2.010E-03
331	to	336	2.200E-03	2.300E-03	2.400E-03	2.550E-03	2.700E-03	2.800E-03
337	to	342	3.000E-03	3.200E-03	3.400E-03	3.600E-03	3.800E-03	4.000E-03
343	to	348	4.250E-03	4.500E-03	4.750E-03	5.000E-03	5.250E-03	5.500E-03
349	to	354	5.750E-03	6.000E-03	6.300E-03	6.600E-03	6.900E-03	7.200E-03
355	to	360	7.600E-03	8.000E-03	8.400E-03	8.800E-03	9.200E-03	9.600E-03
361	to	366	1.000E-02	1.050E-02	1.100E-02	1.150E-02	1.200E-02	1.275E-02
367	to	372	1.350E-02	1.425E-02	1.500E-02	1.600E-02	1.700E-02	1.800E-02
373	to	378	1.900E-02	2.000E-02	2.100E-02	2.200E-02	2.300E-02	2.400E-02
379	to	384	2.550E-02	2.700E-02	2.800E-02	3.000E-02	3.200E-02	3.400E-02
385	to	390	3.600E-02	3.800E-02	4.000E-02	4.250E-02	4.500E-02	4.750E-02
391	to	396	5.000E-02	5.250E-02	5.500E-02	5.750E-02	6.000E-02	6.300E-02
397	to	402	6.600E-02	6.900E-02	7.200E-02	7.600E-02	8.000E-02	8.400E-02
403	to	408	8.800E-02	9.200E-02	9.600E-02	1.000E-01	1.050E-01	1.100E-01
409	to	414	1.150E-01	1.200E-01	1.275E-01	1.350E-01	1.425E-01	1.500E-01
415	to	420	1.600E-01	1.700E-01	1.800E-01	1.900E-01	2.000E-01	2.100E-01
421	to	426	2.200E-01	2.300E-01	2.400E-01	2.550E-01	2.700E-01	2.800E-01
427	to	432	3.000E-01	3.200E-01	3.400E-01	3.600E-01	3.800E-01	4.000E-01
433	to	438	4.250E-01	4.500E-01	4.750E-01	5.000E-01	5.250E-01	5.500E-01
439	to	444	5.750E-01	6.000E-01	6.300E-01	6.600E-01	6.900E-01	7.200E-01
445	to	450	7.600E-01	8.000E-01	8.400E-01	8.800E-01	9.200E-01	9.600E-01
451	to	456	1.000E+00	1.100E+00	1.200E+00	1.300E+00	1.400E+00	1.500E+00
457	to	462	1.600E+00	1.700E+00	1.800E+00	1.900E+00	2.000E+00	2.100E+00
463	to	468	2.200E+00	2.300E+00	2.400E+00	2.500E+00	2.600E+00	2.700E+00

Table 3.2-11. Neutron energy group boundaries for the 640-group ASTM neutron dpa cross sections (continued)

Boundary numbers			Energy group boundaries (MeV)					
469	to	474	2.800E+00	2.900E+00	3.000E+00	3.100E+00	3.200E+00	3.300E+00
475	to	480	3.400E+00	3.500E+00	3.600E+00	3.700E+00	3.800E+00	3.900E+00
481	to	486	4.000E+00	4.100E+00	4.200E+00	4.300E+00	4.400E+00	4.500E+00
487	to	492	4.600E+00	4.700E+00	4.800E+00	4.900E+00	5.000E+00	5.100E+00
493	to	498	5.200E+00	5.300E+00	5.400E+00	5.500E+00	5.600E+00	5.700E+00
499	to	504	5.800E+00	5.900E+00	6.000E+00	6.100E+00	6.200E+00	6.300E+00
505	to	510	6.400E+00	6.500E+00	6.600E+00	6.700E+00	6.800E+00	6.900E+00
511	to	516	7.000E+00	7.100E+00	7.200E+00	7.300E+00	7.400E+00	7.500E+00
517	to	522	7.600E+00	7.700E+00	7.800E+00	7.900E+00	8.000E+00	8.100E+00
523	to	528	8.200E+00	8.300E+00	8.400E+00	8.500E+00	8.600E+00	8.700E+00
529	to	534	8.800E+00	8.900E+00	9.000E+00	9.100E+00	9.200E+00	9.300E+00
535	to	540	9.400E+00	9.500E+00	9.600E+00	9.700E+00	9.800E+00	9.900E+00
541	to	546	1.000E+01	1.010E+01	1.020E+01	1.030E+01	1.040E+01	1.050E+01
547	to	552	1.060E+01	1.070E+01	1.080E+01	1.090E+01	1.100E+01	1.110E+01
553	to	558	1.120E+01	1.130E+01	1.140E+01	1.150E+01	1.160E+01	1.170E+01
559	to	564	1.180E+01	1.190E+01	1.200E+01	1.210E+01	1.220E+01	1.230E+01
565	to	570	1.240E+01	1.250E+01	1.260E+01	1.270E+01	1.280E+01	1.290E+01
571	to	576	1.300E+01	1.310E+01	1.320E+01	1.330E+01	1.340E+01	1.350E+01
577	to	582	1.360E+01	1.370E+01	1.380E+01	1.390E+01	1.400E+01	1.410E+01
583	to	588	1.420E+01	1.430E+01	1.440E+01	1.450E+01	1.460E+01	1.470E+01
589	to	594	1.480E+01	1.490E+01	1.500E+01	1.510E+01	1.520E+01	1.530E+01
595	to	600	1.540E+01	1.550E+01	1.560E+01	1.570E+01	1.580E+01	1.590E+01
601	to	606	1.600E+01	1.610E+01	1.620E+01	1.630E+01	1.640E+01	1.650E+01
607	to	612	1.660E+01	1.670E+01	1.680E+01	1.690E+01	1.700E+01	1.710E+01
613	to	618	1.720E+01	1.730E+01	1.740E+01	1.750E+01	1.760E+01	1.770E+01
619	to	624	1.780E+01	1.790E+01	1.800E+01	1.810E+01	1.820E+01	1.830E+01
625	to	630	1.840E+01	1.850E+01	1.860E+01	1.870E+01	1.880E+01	1.890E+01
631	to	636	1.900E+01	1.910E+01	1.920E+01	1.930E+01	1.940E+01	1.950E+01
637	to	641	1.960E+01	1.970E+01	1.980E+01	1.990E+01	2.000E+01	

Table 3.2-12. ASTM 640-group iron displacement cross sections for neutrons

Bin numbers			Energy bin midpoint dpa cross sections (10^{-24} cm^2)					
1	to	6	158.3543	154.6209	151.1395	147.8895	144.1054	139.9202
7	to	12	136.086	132.5445	128.7502	124.786	121.1728	117.8527
13	to	18	114.8137	111.9561	109.3199	106.8646	104.5694	101.893
19	to	24	98.93331	96.65981	94.12717	91.05218	88.24872	85.68787
25	to	30	83.33912	81.17265	78.92472	76.63646	74.53734	72.5993
31	to	36	70.81827	69.1479	67.59222	66.13822	64.64189	63.12039
37	to	42	61.70157	60.37332	58.92732	57.39681	55.97892	54.65984
43	to	48	53.4322	52.28703	51.21545	50.07727	48.89598	47.79609
49	to	54	46.7687	45.57125	44.25006	43.03653	41.91761	40.71708
55	to	60	39.46333	38.32018	37.26968	36.30967	35.4071	34.57391
61	to	66	33.79705	33.06956	32.22424	31.28942	30.57002	29.76999
67	to	72	28.79791	27.91048	27.10139	26.35879	25.67357	24.96309
73	to	78	24.2396	23.57548	22.96268	22.3992	21.87094	21.37982
79	to	84	20.91994	20.44705	19.96509	19.51724	19.0967	18.63984
85	to	90	18.15581	17.70708	17.29049	16.90205	16.54074	16.20166
91	to	96	15.84242	15.46908	15.12094	14.79594	14.41855	14.00095
97	to	102	13.61661	13.26338	12.88403	12.48759	12.12633	11.79428
103	to	108	11.49039	11.2076	10.94298	10.69745	10.46804	10.20132
109	to	114	9.90672	9.67945	9.42704	9.11875	8.83882	8.58293
115	to	120	8.34796	8.13162	7.90753	7.67881	7.4688	7.27681
121	to	126	7.0976	6.93077	6.77561	6.6307	6.48208	6.33043
127	to	132	6.18896	6.05663	5.91315	5.7603	5.61862	5.4869
133	to	138	5.36434	5.25003	5.14317	5.02925	4.91143	4.80194
139	to	144	4.69971	4.58158	4.45036	4.32961	4.21822	4.09919
145	to	150	3.9743	3.8604	3.75605	3.66076	3.57131	3.4887
151	to	156	3.41162	3.33947	3.25605	3.16328	3.09163	3.01315
157	to	162	2.91695	2.8294	2.74981	2.67675	2.60884	2.52793
163	to	168	2.4409	2.37438	2.31361	2.25746	2.20533	2.15411
169	to	174	2.10873	2.06013	2.01173	1.96605	1.92359	1.87739
175	to	180	1.8286	1.78301	1.74125	1.70342	1.66779	1.63208
181	to	186	1.59575	1.55872	1.52229	1.4902	1.45155	1.40959
187	to	192	1.37025	1.33464	1.2963	1.25614	1.21982	1.18762
193	to	198	1.15603	1.12675	1.09998	1.07523	1.05188	1.02622
199	to	204	0.99657	0.97222	0.94767	0.91571	0.88768	0.8612
205	to	210	0.83773	0.81538	0.79288	0.76959	0.74817	0.72866
211	to	216	0.71075	0.69416	0.67789	0.6635	0.64808	0.63272
217	to	222	0.61821	0.60474	0.59004	0.57456	0.56003	0.5467
223	to	228	0.5346	0.52324	0.51187	0.50029	0.48849	0.47691
229	to	234	0.46669	0.45436	0.44098	0.42842	0.41706	0.40481
235	to	240	0.39195	0.3803	0.36995	0.35982	0.35045	0.34186

Table 3.2-13. ASTM 640-group iron displacement cross sections for neutrons (continued)

Bin numbers			Energy bin midpoint dpa cross sections (10^{-24} cm^2)					
241	to	246	0.3339	0.32638	0.3181	0.30854	0.30069	0.29277
247	to	252	0.28246	0.27339	0.26483	0.25722	0.24997	0.24265
253	to	258	0.23508	0.22809	0.2217	0.21585	0.2104	0.20506
259	to	264	0.20034	0.19527	0.19021	0.18542	0.18098	0.17611
265	to	270	0.17097	0.16615	0.1617	0.15765	0.15385	0.15005
271	to	276	0.14616	0.14219	0.1383	0.13485	0.13068	0.12615
277	to	282	0.12189	0.11802	0.11383	0.10943	0.10543	0.10186
283	to	288	0.09838	0.09515	0.09225	0.10485	0.10283	0.08397
289	to	294	0.08057	0.07783	0.07506	0.07148	0.06843	0.15817
295	to	300	0.07452	0.0602	0.05753	0.05485	0.0524	0.05017
301	to	306	0.04855	0.0475	0.08634	0.36846	0.72307	1.08517
307	to	312	1.43306	1.75376	2.10054	2.42889	2.72279	2.99877
313	to	318	3.25846	3.46537	3.61897	3.78708	3.96427	13.13789
319	to	324	10.69382	4.26269	4.33839	4.43537	4.53423	4.59258
325	to	330	4.78318	4.70162	4.84122	4.99901	5.11134	5.18399
331	to	336	5.27907	5.40891	5.52374	5.69544	5.82685	5.97541
337	to	342	6.17352	6.39541	6.65858	7.18394	10.01168	9.19449
343	to	348	8.17827	8.22966	8.50853	8.91088	9.52539	10.59739
349	to	354	13.20411	21.17466	19.6734	18.59203	24.36627	39.42936
355	to	360	56.38621	48.66102	35.1179	27.24892	23.52159	20.66808
361	to	366	19.98392	18.41869	18.51923	16.80365	16.40945	16.00651
367	to	372	16.06792	15.55876	15.0897	14.61809	13.99511	13.21823
373	to	378	12.01959	10.6153	8.88871	6.85769	4.4353	4.03428
379	to	384	51.58856	462.4204	374.2036	138.8582	91.99242	75.21491
385	to	390	66.92896	62.40611	65.56062	59.51893	61.42897	55.61853
391	to	396	80.54994	84.93746	61.63473	61.83547	61.39486	51.44463
397	to	402	41.0552	35.18787	195.2115	72.9727	139.3801	276.0543
403	to	408	138.4568	104.0743	113.716	105.5489	78.43095	78.06753
409	to	414	60.44543	70.4743	134.1587	255.363	293.0161	133.09
415	to	420	122.7596	156.0143	244.41	370.7627	205.3339	101.0349
421	to	426	307.5111	146.9613	171.8077	135.3387	282.5501	187.6945
427	to	432	142.0391	315.5791	166.553	302.1184	545.7117	528.401
433	to	438	400.4412	309.7825	351.4453	381.0001	327.4008	316.9469
439	to	444	264.2091	190.8042	255.5292	529.8745	389.0167	680.431
445	to	450	627.3019	427.2328	461.2467	327.1398	278.1719	479.7678
451	to	456	498.4922	477.6893	707.1735	616.464	716.4101	734.1659
457	to	462	758.8353	784.558	819.3325	989.3265	928.7681	923.3754
463	to	468	969.48	1079.716	1143.224	1348.954	1192.105	1263.538
469	to	474	1277.801	1271.578	1364.006	1387.724	1358.466	1346.851
475	to	480	1398.034	1334.743	1424.447	1440.708	1483.88	1464.868
481	to	486	1526.371	1560.443	1530.309	1582.916	1523.34	1626.724
487	to	492	1600.863	1617.455	1653.609	1642.833	1600.075	1682.554

Table 3.2-13. ASTM 640-group iron displacement cross sections for neutrons (continued)

Bin numbers	Energy bin midpoint dpa cross sections (10^{-24} cm^2)					
493 to 498	1687.286	1716.469	1731.089	1729.785	1760.852	1760.538
499 to 504	1768.656	1792.105	1811.511	1800.94	1811.547	1859.081
505 to 510	1859.125	1879.237	1890.037	1891.762	1909.485	1909.076
511 to 516	1914.442	1936.414	1941.75	1966.663	1963.306	1986.044
517 to 522	1976.213	1989.243	2003.646	2006.771	2009.093	2013.259
523 to 528	2032.588	2064.755	2063.837	2061.365	2059.507	2072.344
529 to 534	2089.976	2107.525	2122.58	2135.077	2147.577	2160.074
535 to 540	2172.482	2185.892	2199.95	2213.918	2226.698	2238.281
541 to 546	2250.482	2263.392	2276.22	2288.971	2301.725	2313.91
547 to 552	2325.628	2337.342	2348.869	2360.301	2371.744	2383.112
553 to 558	2395.212	2407.952	2421.344	2434.325	2446.243	2458.956
559 to 564	2471.205	2482.247	2493.659	2506.016	2519.598	2534.971
565 to 570	2549.086	2562.977	2576.115	2586.936	2600.011	2615.468
571 to 576	2630.343	2644.455	2658.475	2672.218	2685.52	2698.683
577 to 582	2711.99	2725.313	2738.112	2750.418	2763.164	2775.98
583 to 588	2788.331	2800.214	2811.915	2824.208	2837.183	2849.781
589 to 594	2862.184	2874.421	2877.552	2871.084	2864.617	2858.147
595 to 600	2851.581	2844.839	2837.641	2830.538	2823.427	2816.329
601 to 606	2813.386	2814.819	2816.344	2817.782	2819.124	2819.92
607 to 612	2819.883	2819.846	2819.725	2819.631	2823.437	2831.455
613 to 618	2839.475	2847.22	2855.056	2862.956	2870.913	2878.96
619 to 624	2886.826	2894.594	2903.983	2914.913	2925.791	2936.34
625 to 630	2946.712	2956.448	2965.448	2974.45	2983.453	2992.455
631 to 636	2999.561	3004.583	3009.698	3014.721	3019.741	3025.406
637 to 640	3031.526	3037.737	3043.95	3050.161		

Table 3.2-14. Iron displacement cross sections for photons

Energy (MeV)	dpa cross section (10^{-24} cm^2)	Energy (MeV)	dpa cross section (10^{-24} cm^2)
1.0	0.0052	6.0	2.834
1.5	0.0754	6.5	3.318
2.0	0.2158	7.0	3.838
2.5	0.4108	7.5	4.384
3.0	0.6448	8.0	4.971
3.5	0.9178	8.5	5.585
4.0	1.227	9.0	6.627
4.5	1.576	9.5	6.900
5.0	1.960	10.0	7.600
5.5	2.379	14.0	7.600

4. RESULTS

Neutron and photon dpa rates have been computed in the HFIR RV. These calculated dpa rates are based on computer models that use a homogenized description of the core. Newer, more detailed models have subsequently been developed. These newer models, as described in Ilas and Chandler [27], incorporate an explicit representation of the individual fuel plates in the core. For the HEU cycle 400 model of Ilas and Chandler [27], the relative fission density distribution in the core and the broad-group (fast, epi-thermal, and thermal) neutron flux at various locations in the reflector are virtually unchanged between the simplified and explicit models. This indicates that the source term for the HEU cycle 400 vessel damage calculations is not significantly changed by using the newer, explicit core model. Therefore, the HEU results presented below, which are based on the older, homogenized core model, will not be significantly impacted by the choice of core model. It is anticipated that similar trends will be seen for LEU models using the explicit core model. However, if ongoing LEU core design analyses show a larger sensitivity to the choice of core representation (i.e., simplified versus explicit), then the LEU vessel damage results presented below will need to be revisited. Additionally, future cycle-specific models with various isotope-production targets located near the beam tube openings in the reflector will likely result in changes to the flux spectrum entering the beam tubes. Because the flux exiting the beam tubes near the corresponding nozzle penetrations in the RV contributes to the damage in the vicinity of each of these penetrations, the effects of target loading in the reflector on vessel damage should be considered for both HEU and LEU core operations.

The ADVANTG code was used to generate weight windows and biased sources optimized for the calculation of the dpa rates in a cylindrical shell beginning at the inner surface of the HFIR RV and extending ⅛" into the RV base metal. This cylindrical shell extended from 21.5" below the core axial midplane to 21.5" above the core axial midplane. To quantify dpa rates at the interface between the RV and the RV inner liner, a cylindrical mesh tally consisting of 1 radial (0.125" thick), 43 axial (1" tall), and 360 radial (1° of arc) bins was superimposed on this cylindrical shell. The average neutron and photon dpa rates were tallied in each of the 15,480 bins of this cylindrical mesh tally. With this mesh structure, one row of tally bins was axially centered on the lower girth weld, which is located 17" below the core axial midplane, and one row of tally bins was axially centered on the core axial midplane. This mesh tally configuration is consistent with that used in the HEU damage rate assessments of Risner and Blakeman [2]. The statistical uncertainty (1σ relative error) in the calculated dpa rates over the mesh tally region described above is typically below 1% for all cases (BOC, EOC, neutron, photon). At some select locations that are heavily shielded by the lead and steel of the ion chambers, the statistical uncertainty in the photon dpa rates is higher (up ~6% for the fission photons at the core midplane and directly behind the ICs). However, the actual magnitude of the dpa rate is quite low (2–3 orders of magnitude below the dpa rates on either side of an IC) in these locations.

The calculated dpa rates discussed below are based on an operating power of 100 MW. BOC and EOC dpa rates have been calculated. The neutron and prompt (fission plus capture) photon dpa rates for an LEU core at EOC are discussed in Sect. 4.1. Ratios of the EOC to BOC dpa rates for the LEU core are discussed in Sect. 4.2, while Sect. 4.3 compares the LEU damage rates (both neutron and prompt photon) to the latest (Risner and Blakeman [2]) dpa rates calculated for an HEU core. Dpa rates in the RV due to photons emitted by FPs are discussed in Sect. 4.4.

The neutron-induced dpa rates at the HFIR RV are generally quite consistent, regardless of time in life (i.e., BOC or EOC) or core configuration (i.e., HEU or LEU) The change between EOC and BOC neutron dpa rates for the LEU core is typically no more than ±5%, regardless of axial or azimuthal location in the mesh tally described above. Similarly, the LEU/HEU neutron dpa rate ratios at EOC are typically in the 0.9–0.95 range.

The effect of configuration on the prompt photon-induced dpa rates is typically larger. For the LEU core, the EOC/BOC prompt photon-dpa rate ratios are generally between 1.15 and 1.25 in the region of the mesh tally described above. This behavior is expected given the changes in control element configuration throughout an operational cycle. At BOC, two cylindrical control elements completely surround the core with significant quantities of high Z materials (Eu and Ta). Throughout the operational cycle, the two control elements are withdrawn in opposite directions until at EOC, only the aluminum portion of each of the control elements is surrounding the core. In this configuration, the control elements are more transparent to the prompt photons being produced in the core. This leads to the increase in prompt-photon-induced dpa rates at EOC. Conversely, at a given time in life, the prompt photon dpa rates for an LEU core are typically around 20–30% lower than those predicted for the HEU core. This behavior arises from multiple causes. First, the quantity of high Z materials in the LEU core is greater than in the HEU core. Although the LEU and HEU cores have the same overall volume, the LEU core contains roughly 127 kg of uranium as opposed to 10.1 kg of uranium in the HEU core. Additionally, the LEU fuel consists of an aluminum-clad U-Mo alloy (with 10% molybdenum by weight), while the HEU fuel is made of U_3O_8 dispersed in aluminum. The increased quantity of high Z materials in the LEU fuel leads to a significant increase in the self-attenuation of prompt photons generated in the LEU core. This leads to a reduction in the core-generated prompt photon energy deposited in the RV. Finally, changes in the neutron spectrum outside the core region can lead to changes in the quantity and spectrum of prompt photons generated through neutron capture or inelastic reactions. Atomic displacements in the HFIR RV that are caused by delayed (FP) photons represent a small contribution to the overall vessel dpa rates. The FP photon contribution to vessel dpa rates is typically around 3.5–4% of the prompt photon contribution.

4.1 LEU EOC NEUTRON AND PHOTON DPA RATES

The LEU EOC dpa rates over the mesh tally region described above in Section 4 are presented in Figs. 4.1-1 through 4.1-16. Figure 4.1-1 (a) presents a simplified 3D view of the geometry and neutron dpa rates over the 180° arc of the RV containing beam lines HB-1, HB-2, and HB-3, as well as the ion chamber (IC) near HB-1. Figure 4.1-1 (b) presents the geometry and neutron dpa rates over the opposite 180° arc of the RV. In both sections of Fig. 4.1-1, all geometry inside the outer radius of the permanent reflector, except for the beam tubes, has been removed. Additionally, the various dosimetry keys and RV inner liner have been removed from view. The only geometric entities remaining in Fig. 4.1-1 are the RV, the nozzle bosses, and the beam lines. Figure 4.1-1 shows that for a significant azimuthal extent, the neutron dpa rates in the RV are affected by the presence of the various beam lines. Near the beam lines, the neutron dpa rate contours in the RV are nearly circular, indicating that neutrons traveling down the beam tubes to near the RV before exiting the beam tubes are responsible for a significant portion of the calculated neutron dpa rates in the vessel. These contours become more oblate farther away from the beam tubes. This indicates that away from the influence of the beam tubes, the axial power shape in the core, which is generally center peaked (e.g., Figs. 11 and 12 in Ilas and Primm [1]), has an increased significance on the RV neutron dpa rates. What is less obvious from Fig. 4.1-1 is the influence the ion chamber near beam tube HB-1 has on the dpa rates around beam tube HB-2. The effect of the ion chambers on the neutron dpa rates near beam tubes HB-1 and HB-2 is more clearly seen in Figures. 4.1-3 through 4.1-5.

Similar 3D plots of the photon dpa rates are presented in Fig. 4.1-2, which clearly shows a significant decrease in the photon dpa rates behind the ICs and the effects of the dosimetry key located around beam tube HB-2. The shape of the photon dpa rates in the shadow of this dosimetry key is a function of several factors. First, photons traveling down the inner volume of the beam tube can exit the beam tube outboard of the dosimetry key and contribute to photon dpa rate in a narrow cone surrounding the beam tube. Secondly, neutrons traveling down the inner volume of the beam tube can have an inelastic interaction with the beam tube outboard of the dosimetry key and generate secondary photons that can contribute to photon dpa rate in a narrow cone surrounding the beam tube. Third, photons generated anywhere inboard

of the dosimetry key will be more highly attenuated by the steel of the dosimetry key than they would have if the key were not there. However, neutrons generated inboard of the dosimetry key can interact with the steel of the dosimetry key and generate secondary photons that will increase the photon dpa rate in the RV. Additionally, neutrons outboard of the dosimetry key can generate secondary photons in the water between the dosimetry key and the RV, in the RV itself, or in the RV inner liner, all of which can contribute to the photon dpa rate in the RV. The pattern in the photon dpa rate in the vessel near the HB-2 beam tube is a complicated function of all these sources of primary and secondary photons. Finally, in Fig. 4.1-2 (b), the shielding effect of the lead and steel in the ion chamber near beam tube HB-4 can be seen. The decrease in the photon dpa rates on the side of beam tube HB-3 that is opposite from the ion chamber is clearly noticeable. Although not seen in section (a) or (b) of Fig. 4.1-2, there is a similar decrease in the photon dpa rates opposite the ion chamber located near beam tube HB-1. Figures 4.1-6 and 4.1-7 show this more clearly.

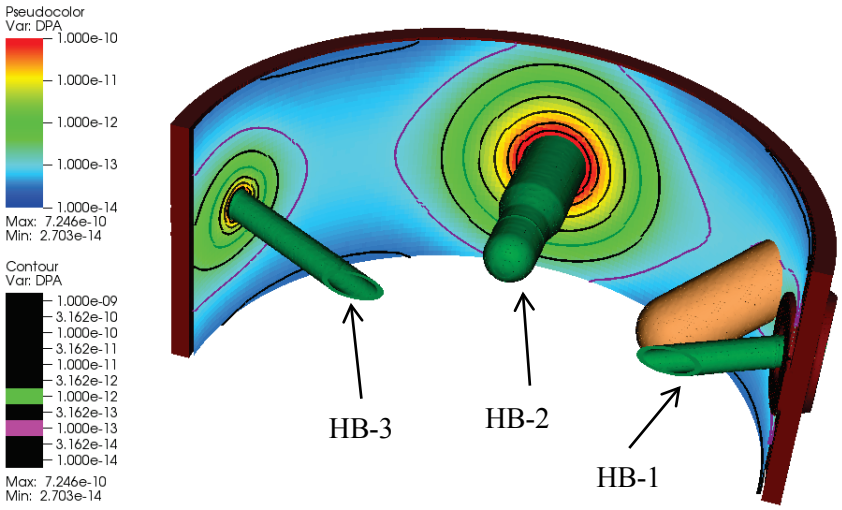

(a)
Azimuthal arc showing portions of beam tubes HB-1, HB-2, and HB-3.

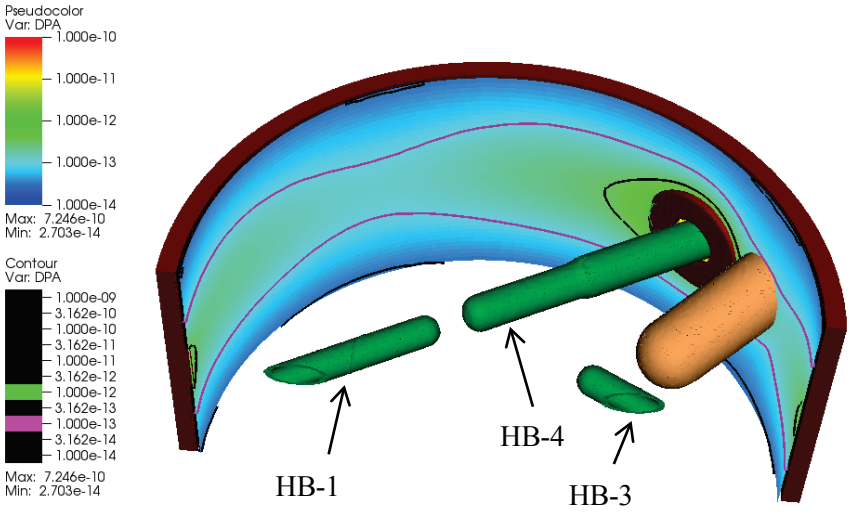

(b)
Azimuthal arc showing portions of beam tubes HB-1, HB-3, and HB-4.

Fig. 4.1-1. Neutron dpa rates averaged over the first 1/8" of RV base metal. (dpa rates are for an LEU core at EOC operating at 100 MW.)

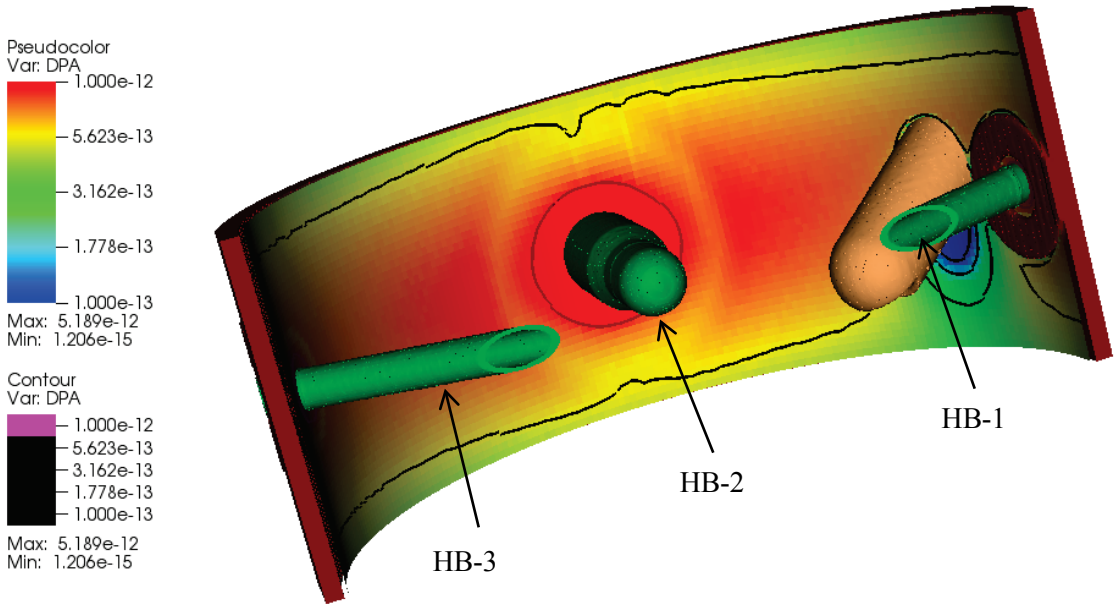

(a)
Azimuthal arc showing portions of beam tubes HB-1, HB-2, and HB-3.

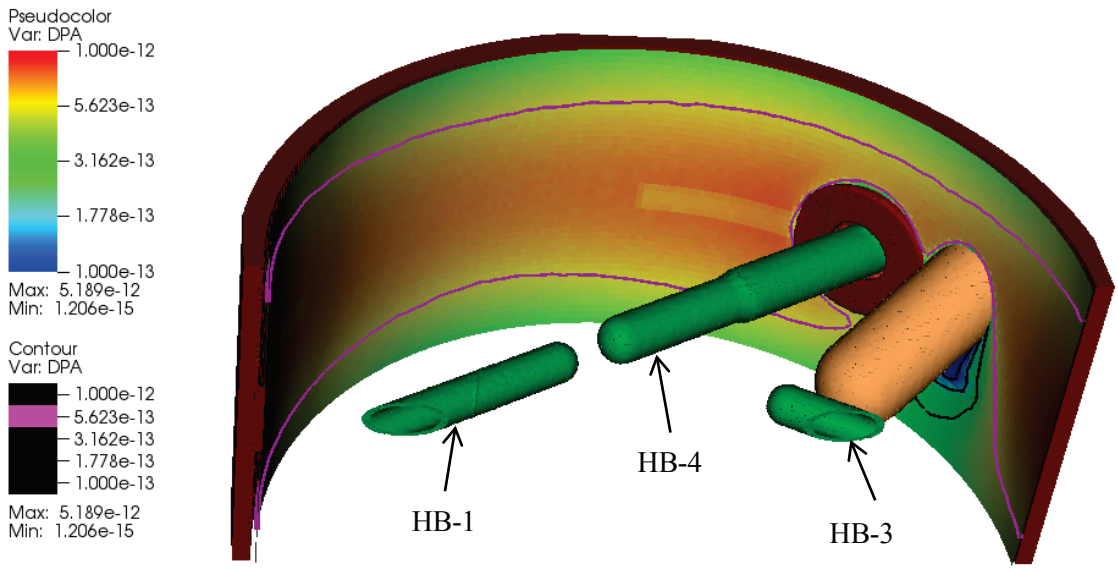

(b)
Azimuthal arc showing portions of beam tubes HB-1, HB-3, and HB-4

Fig. 4.1-2. Photon dpa rates averaged over the first 1/8" of RV base metal. (dpa rates are for an LEU core at EOC, operating at 100 MW.)

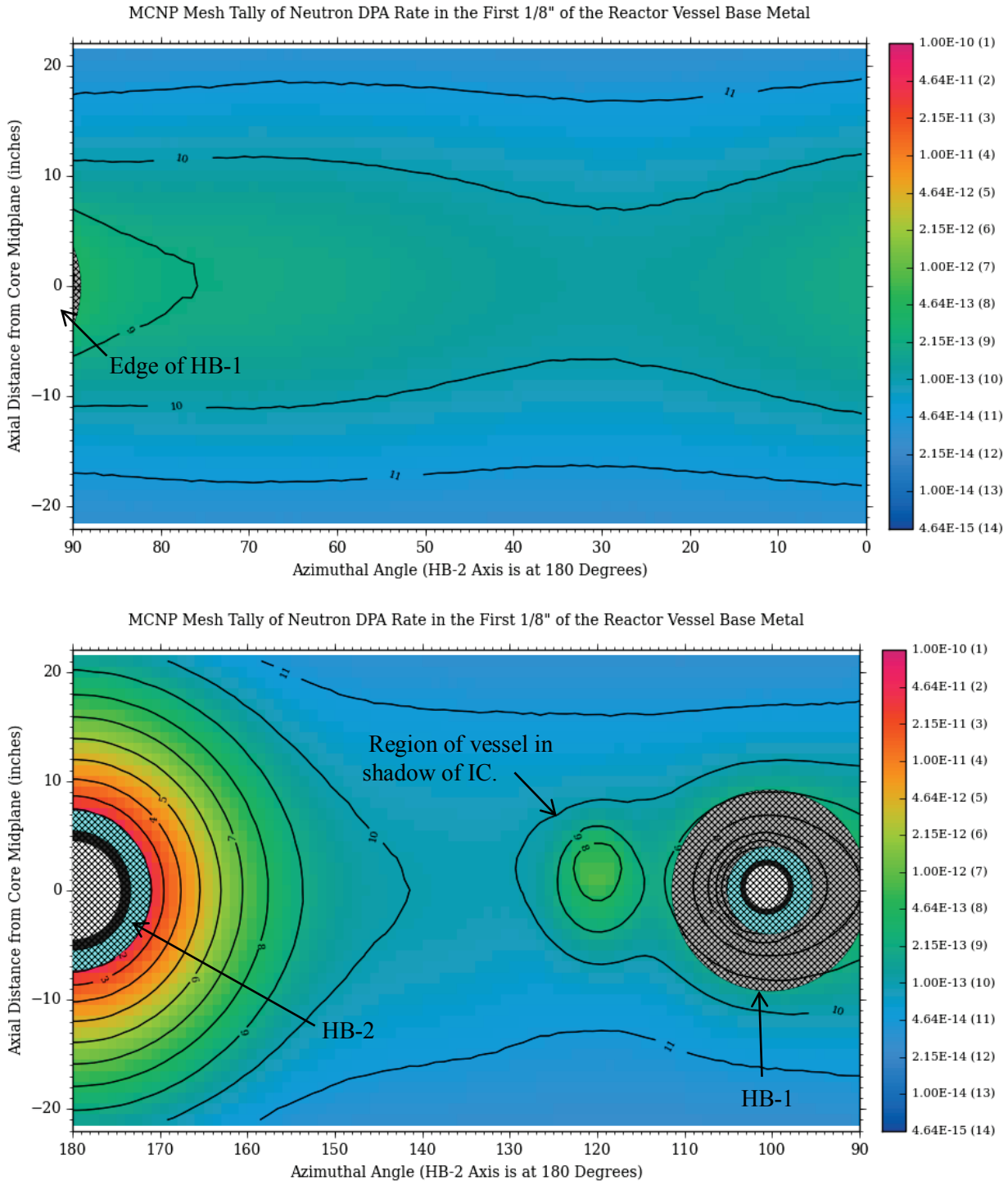

Fig. 4.1-3. Calculated EOC neutron dpa rates in the first (upper plot) and second (lower plot) quadrants of the HFIR model. The azimuthal angle is measured with respect to the +X axis as shown in Fig. 3.2-1. The cross-hatched circles around HB-1 represent the nozzle boss (light gray), water between the boss and the beam line (light blue), and the beam line itself (dark gray). The cross-hatched circles around HB-2 indicate the water between the nozzle and the beam line and the beam line itself.

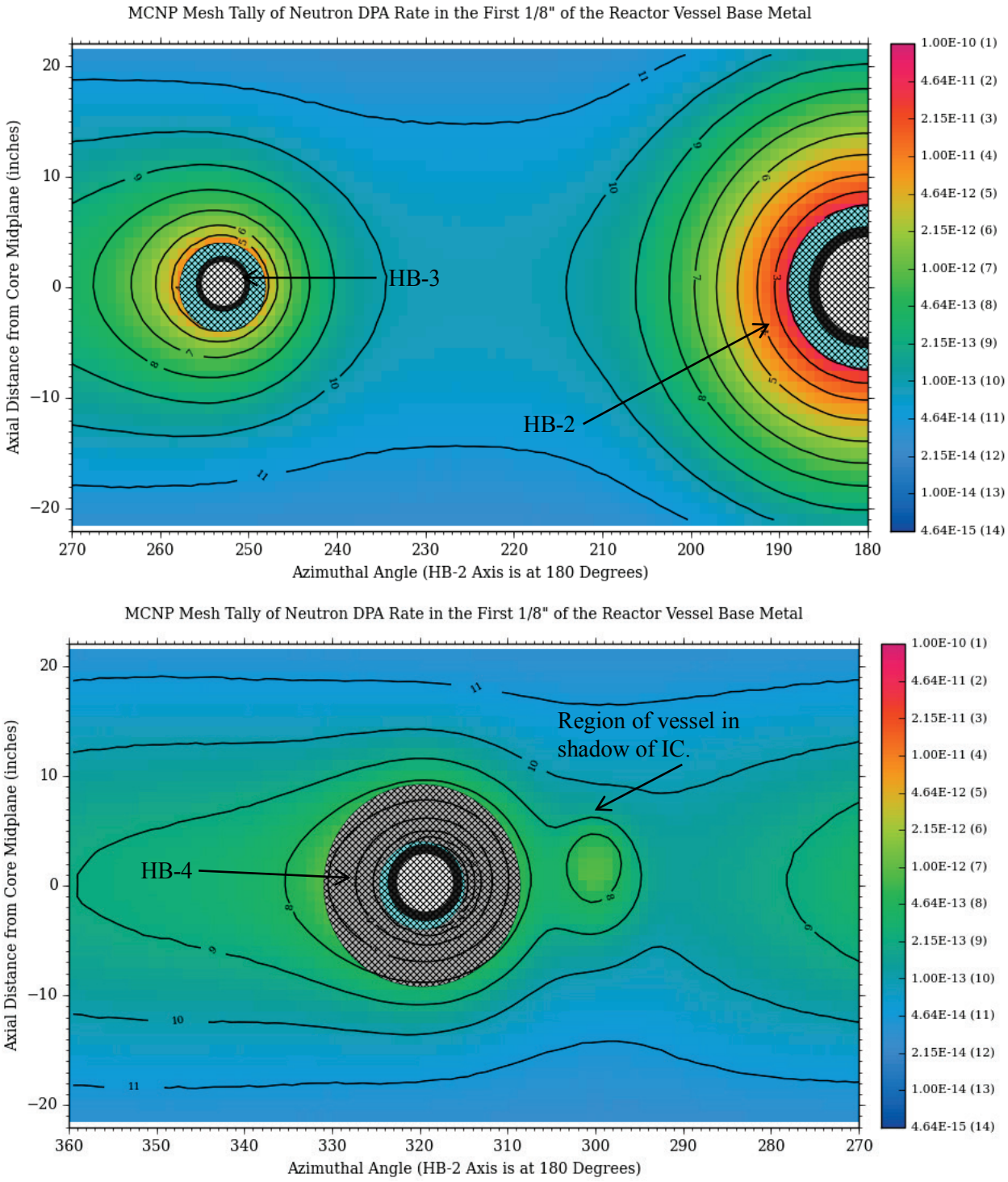

Fig. 4.1-4. Calculated EOC neutron dpa rates in the third (upper plot) and fourth (lower plot) quadrants of the HFIR model. The azimuthal angle is measured with respect to the +X axis as shown in Fig. 3.2-1. The cross-hatched circles around HB-4 represent the nozzle boss (light gray), water between the boss and the beam line (light blue), and the beam line itself (dark gray). The cross-hatched circles around HB-2and HB-3 indicate the water between the nozzle and the beam line and the beam line itself.

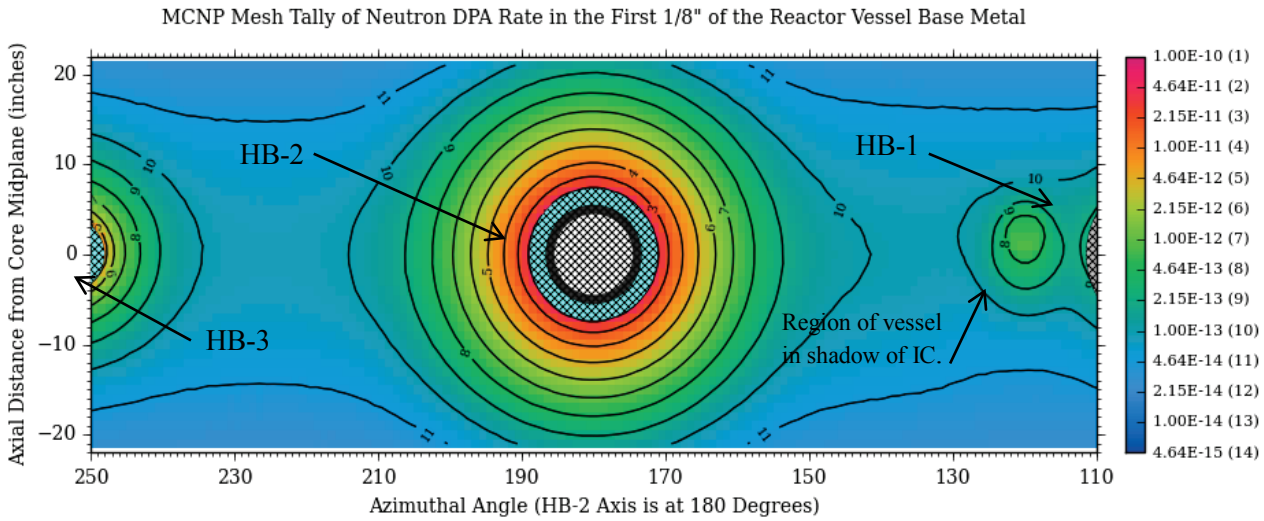

Fig. 4.1-5. Calculated EOC neutron dpa between beam tubes HB-1 and HB-3. The azimuthal angle is measured with respect to the +X axis as shown in Fig. 3.2-1. The cross-hatched circles around HB-2and HB-3 indicate the water between the nozzle and the beam line and the beam line itself.

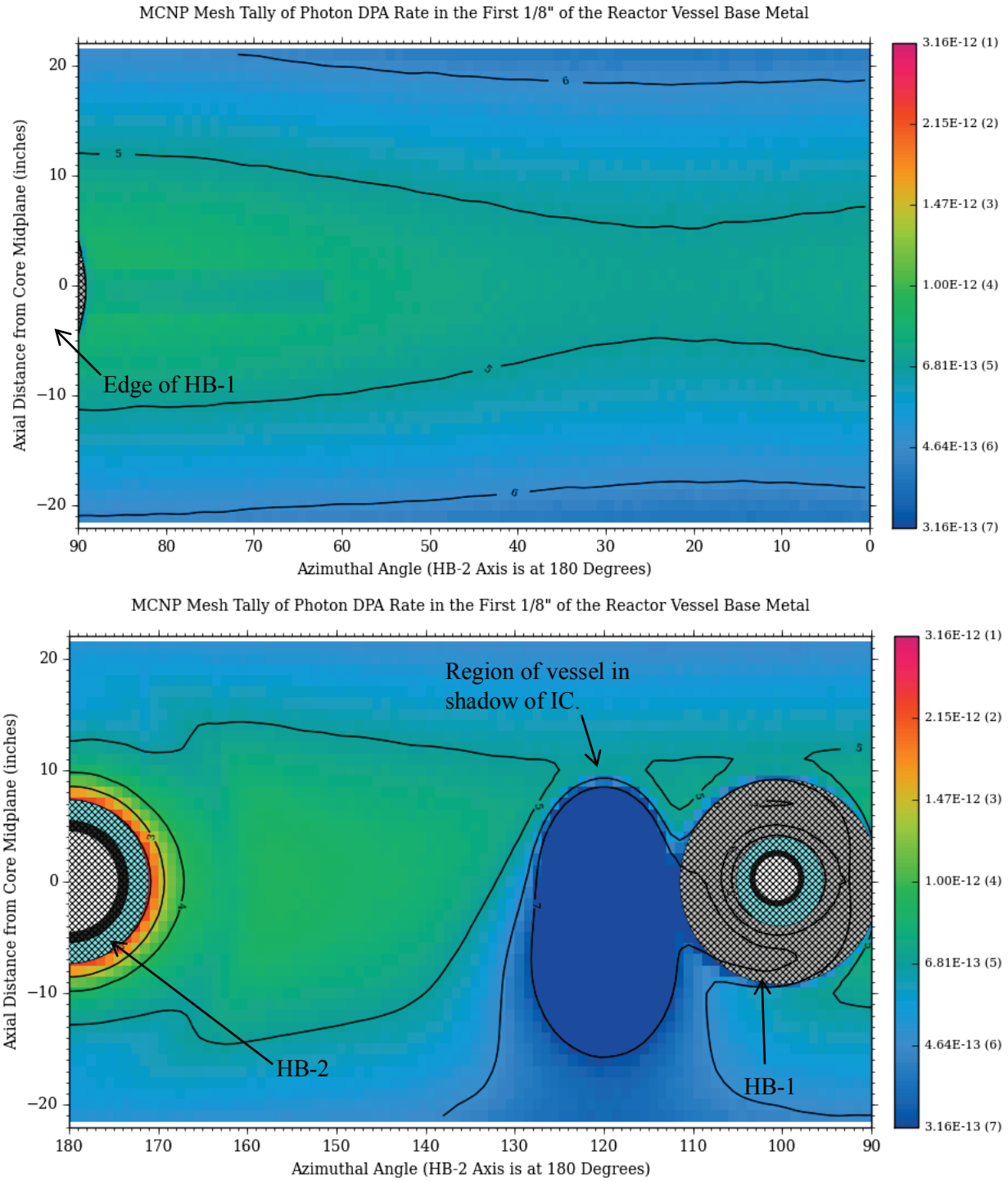

Fig. 4.1-6. Calculated EOC photon dpa rates in the first (upper plot) and second (lower plot) quadrants of the HFIR model. The azimuthal angle is measured with respect to the +X axis as shown in Fig. 3.2-1. The cross-hatched circles around HB-1 represent the nozzle boss (light gray), water between the boss and the beam line (light blue), and the beam line itself (dark gray). The cross-hatched circles around HB-2 indicate the water between the nozzle and the beam line and the beam line itself.

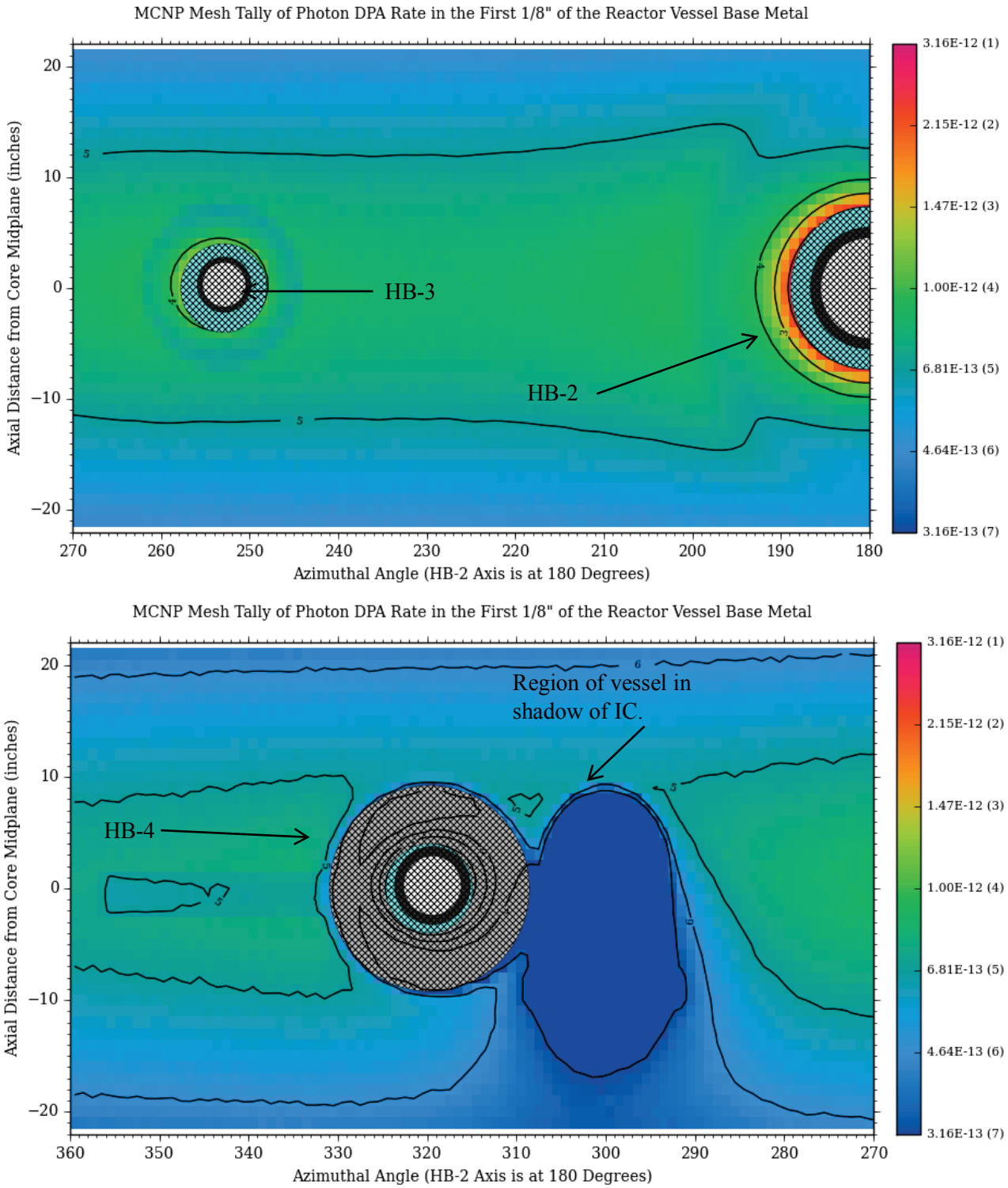

Fig. 4.1-7. Calculated EOC neutron dpa rates in the third (upper plot) and fourth (lower plot) quadrants of the HFIR model. The azimuthal angle is measured with respect to the +X axis as shown in Fig. 3.2-1. The cross-hatched circles around HB-4 represent the nozzle boss (light gray), water between the boss and the beam line (light blue), and the beam line itself (dark gray). The cross-hatched circles around HB-2and HB-3 indicate the water between the nozzle and the beam line and the beam line itself.

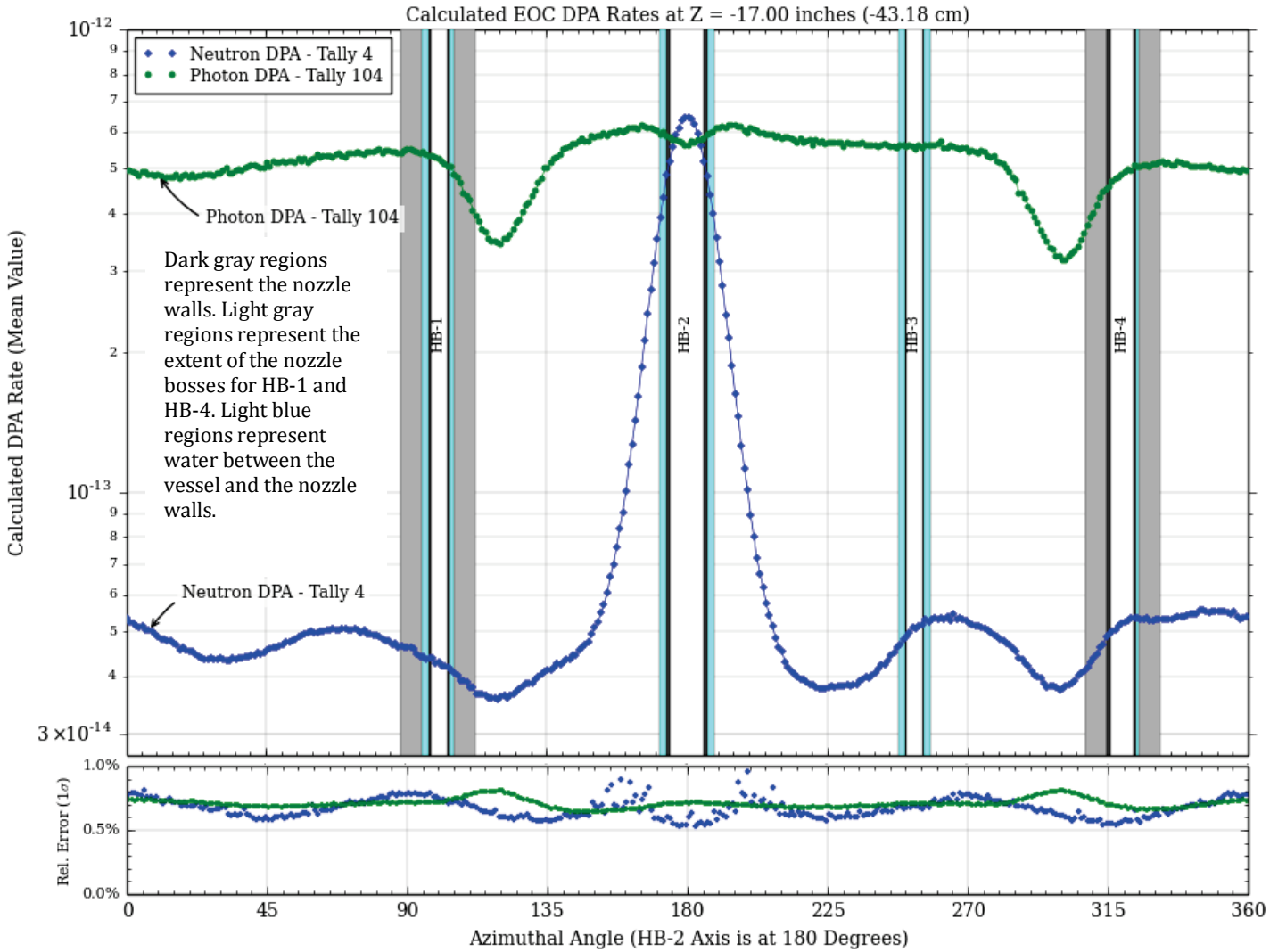

Fig. 4.1-8. Calculated EOC neutron and photon dpa rates at the elevation of the girth weld (17 inches below the HFIR core midplane). The presence of beam tubes HB-1 through HB-4 affect the calculated in-vessel dpa rates for several inches above/below the physical extent of these vessel penetrations. Therefore, the azimuthal extent of all four beam tubes at the core axial midplane is depicted on all dpa rate plots, regardless of axial location.

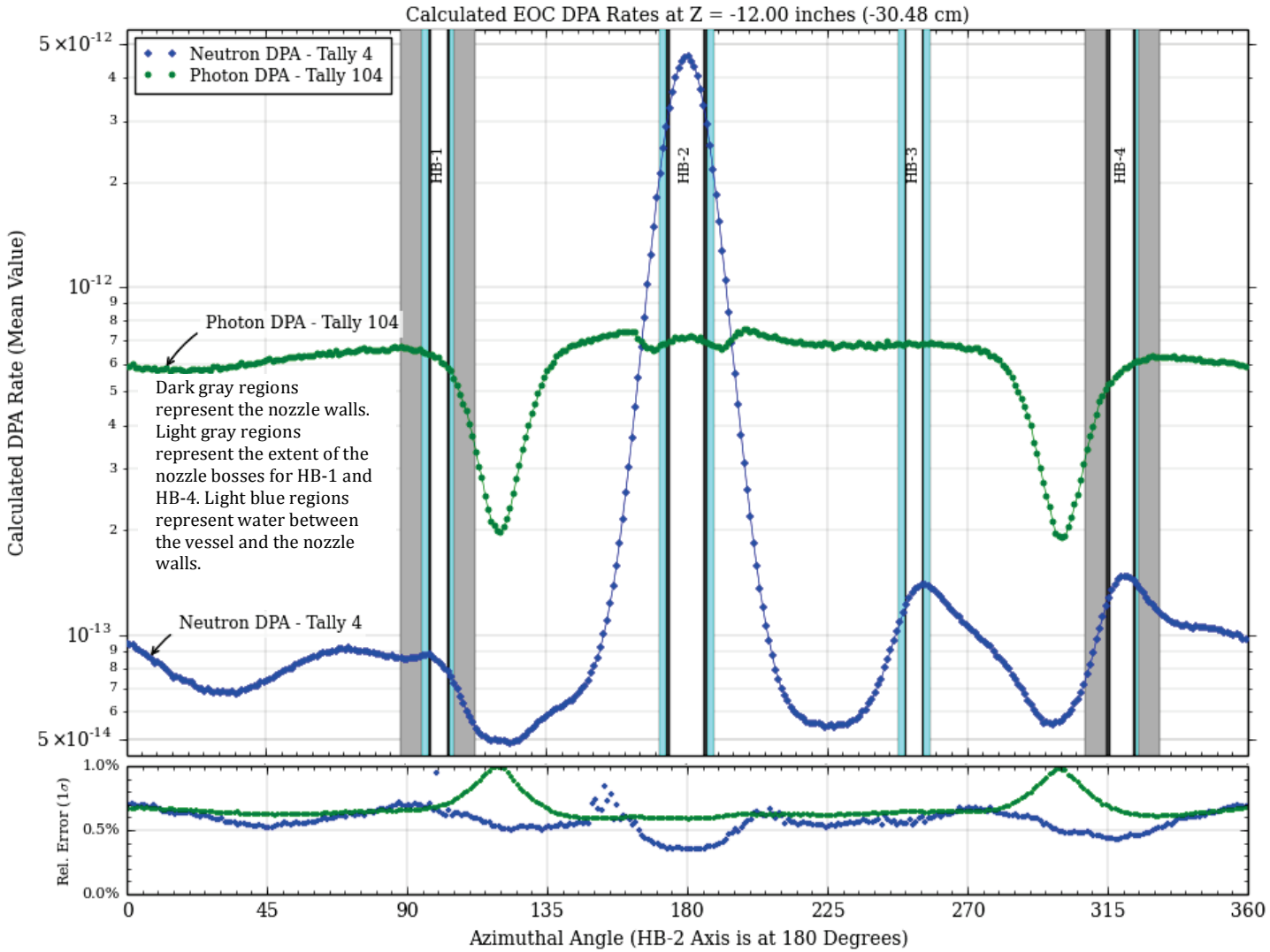

Fig. 4.1-9. Calculated EOC neutron and photon dpa rates at 12 inches below the HFIR core midplane. The presence of beam tubes HB-1 through HB-4 affect the calculated in-vessel dpa rates for several inches above/below the physical extent of these vessel penetrations. Therefore, the azimuthal extent of all four beam tubes at the core axial midplane is depicted on all dpa rate plots, regardless of axial location.

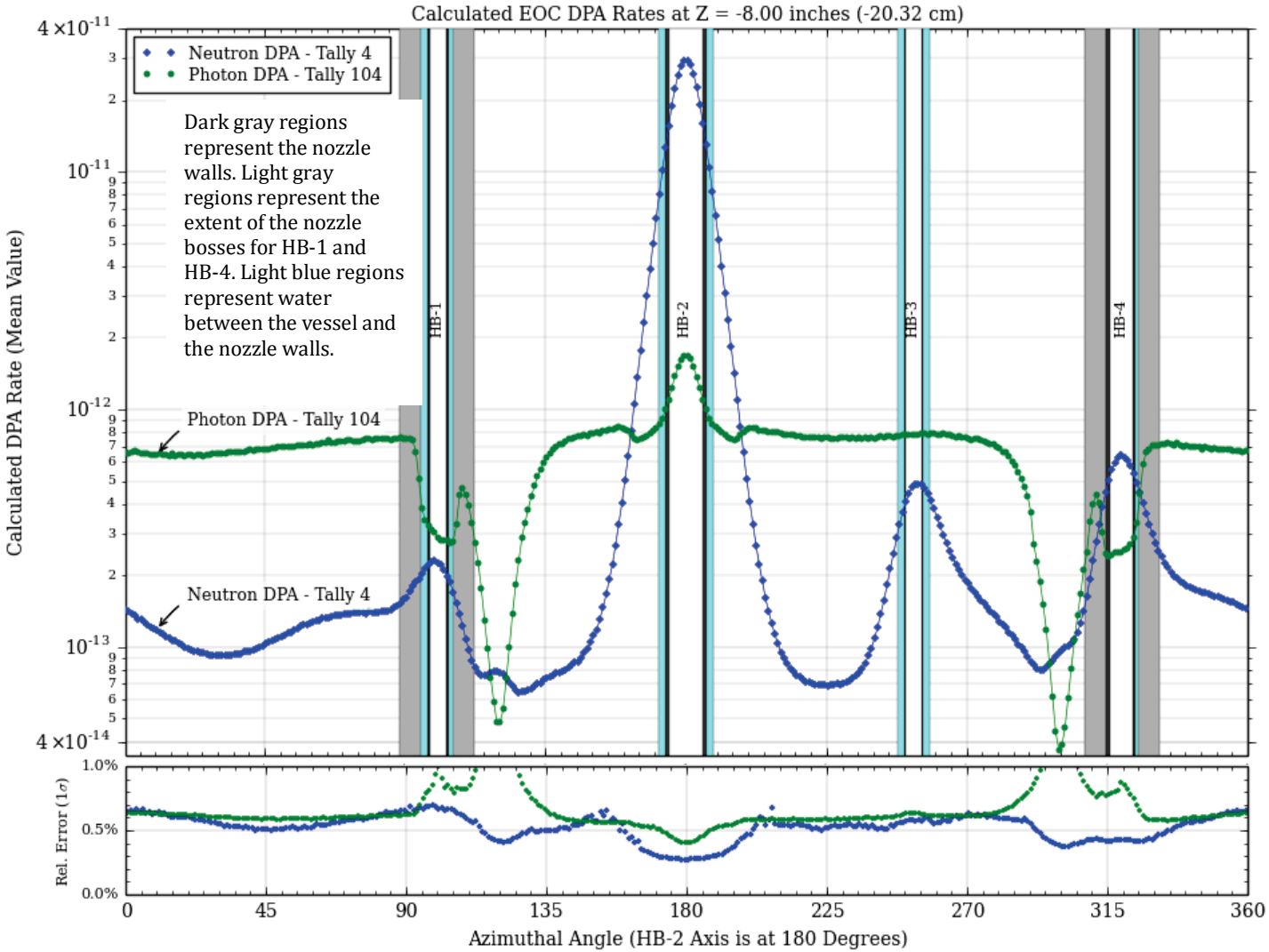

Fig. 4.1-10. Calculated EOC neutron and photon dpa rates at 8 inches below the HFIR core midplane. The presence of beam tubes HB-1 through HB-4 affect the calculated in-vessel dpa rates for several inches above/below the physical extent of these vessel penetrations. Therefore, the azimuthal extent of all four beam tubes at the core axial midplane is depicted on all dpa rate plots, regardless of axial location.

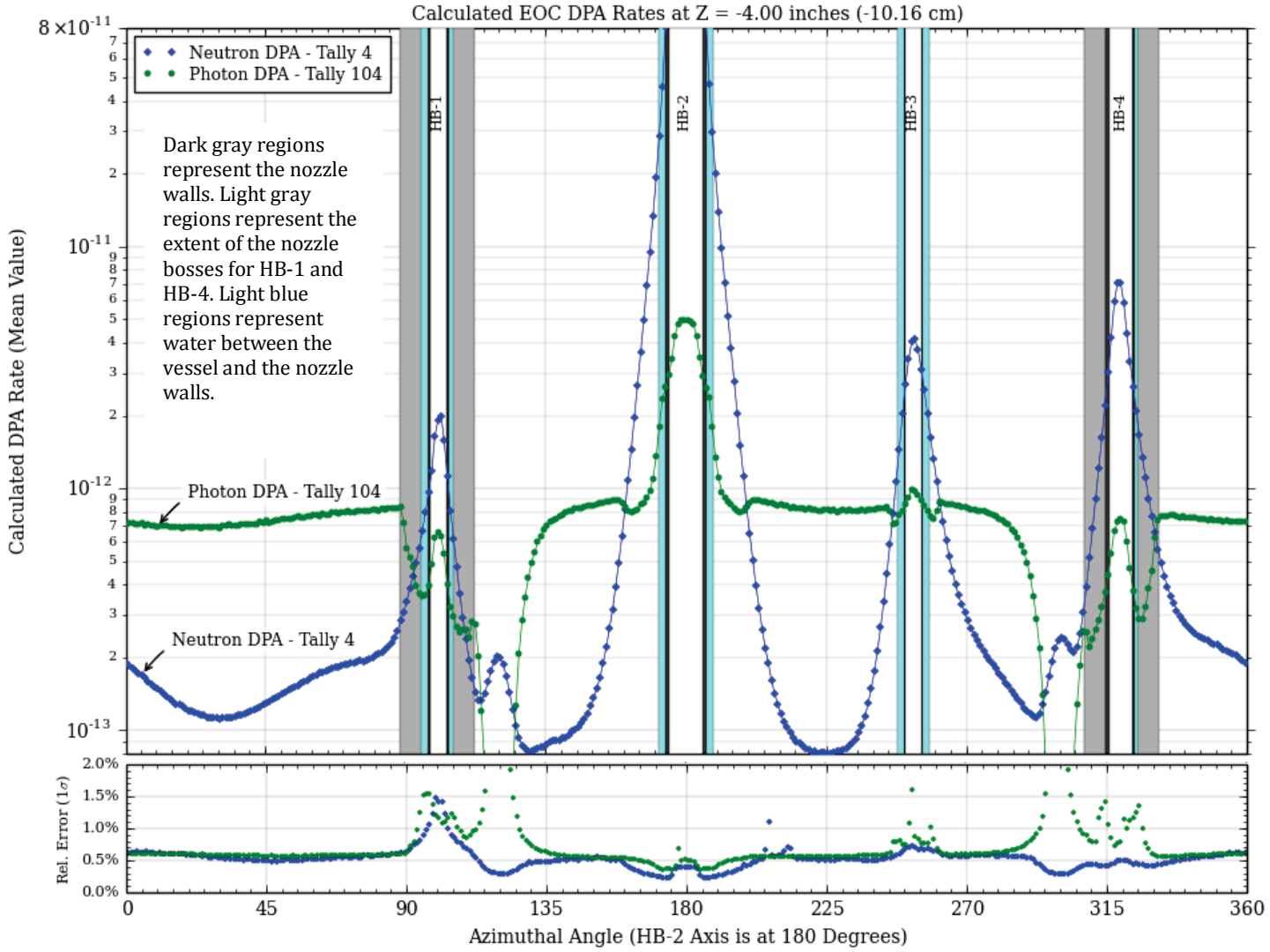

Fig. 4.1-11. Calculated EOC neutron and photon dpa rates at 4 inches below the HFIR core midplane. The presence of beam tubes HB-1 through HB-4 affect the calculated in-vessel dpa rates for several inches above/below the physical extent of these vessel penetrations. Therefore, the azimuthal extent of all four beam tubes at the core axial midplane is depicted on all dpa rate plots, regardless of axial location.

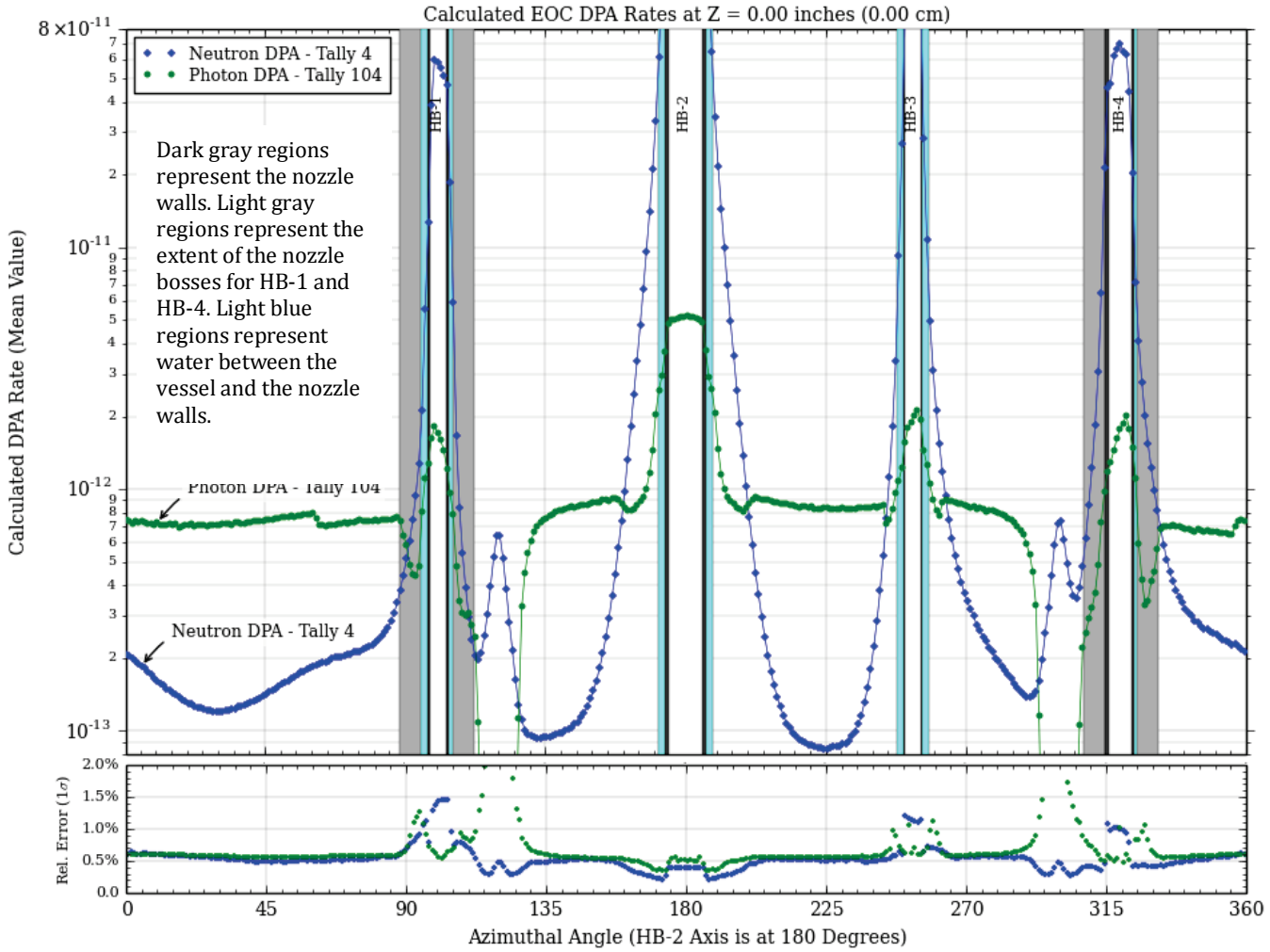

Fig. 4.1-12. Calculated EOC neutron and photon dpa rates at the HFIR core midplane. The presence of beam tubes HB-1 through HB-4 affect the calculated in-vessel dpa rates for several inches above/below the physical extent of these vessel penetrations. Therefore, the azimuthal extent of all four beam tubes at the core axial midplane is depicted on all dpa rate plots, regardless of axial location.

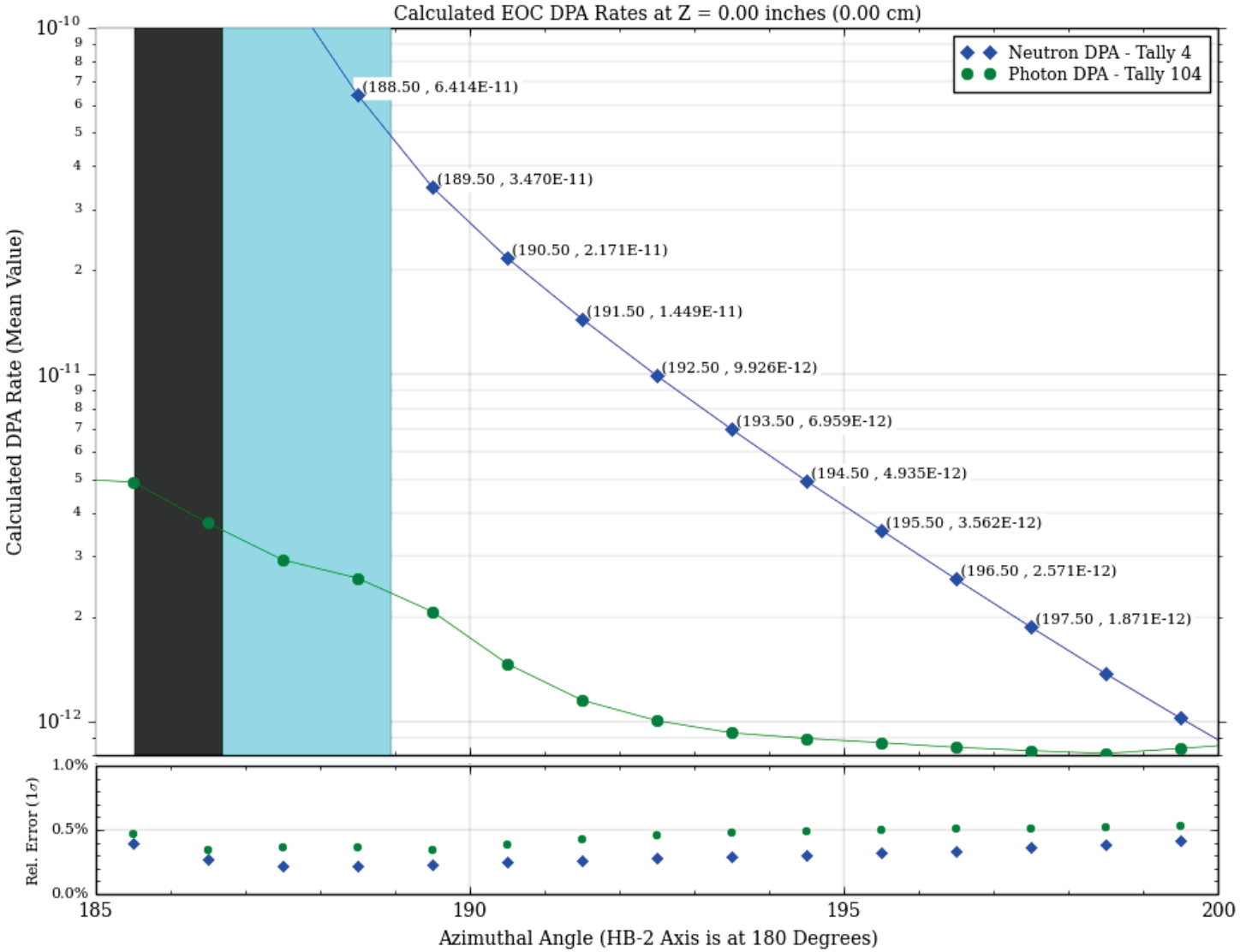

Fig. 4.1-13. Calculated EOC neutron and photon dpa rates showing added detail in the vicinity of beam tube HB-2 at the HFIR core midplane.

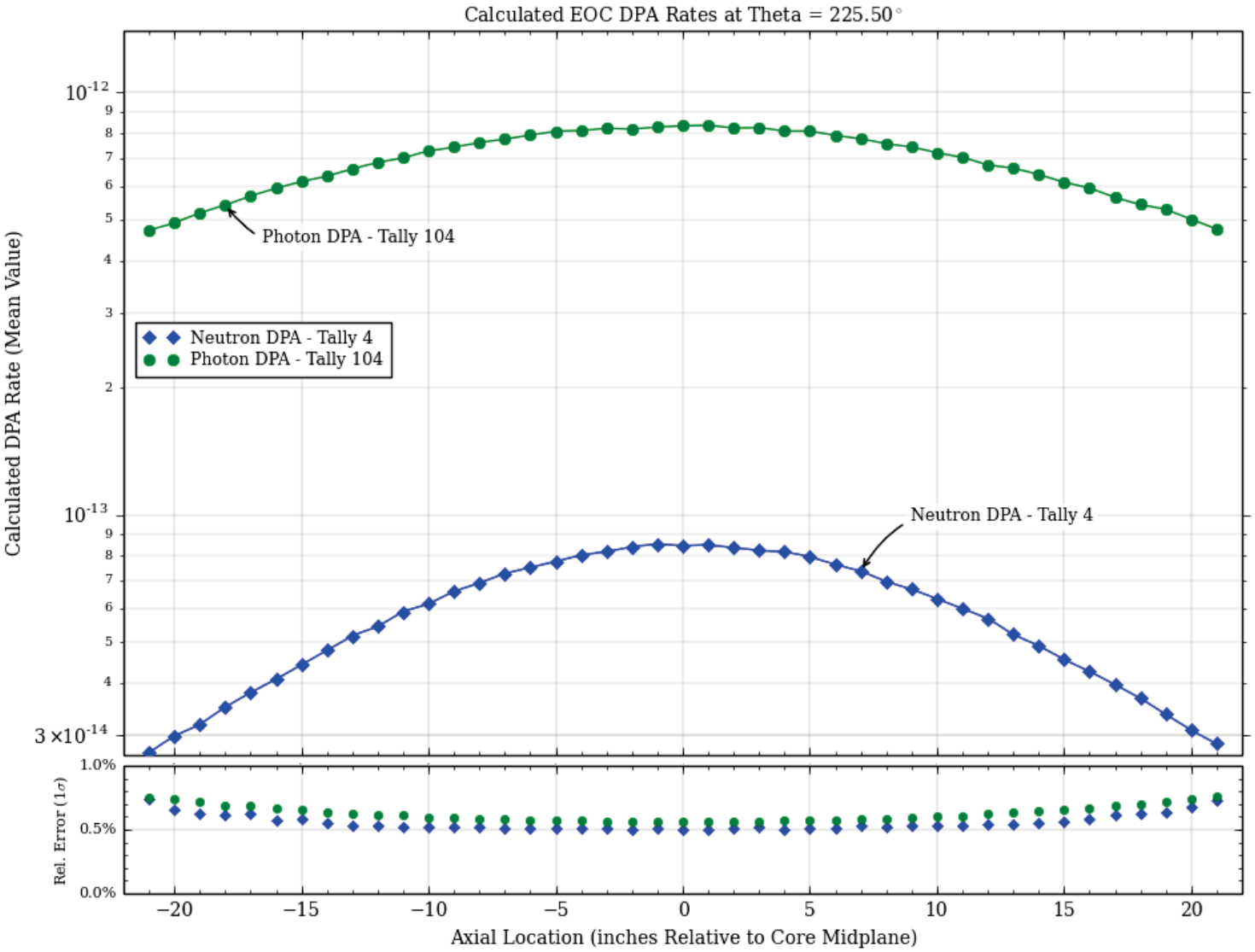

Fig. 4.1-14. Calculated EOC neutron and photon dpa rates in the HFIR RV at 225.5° from the +x axis.

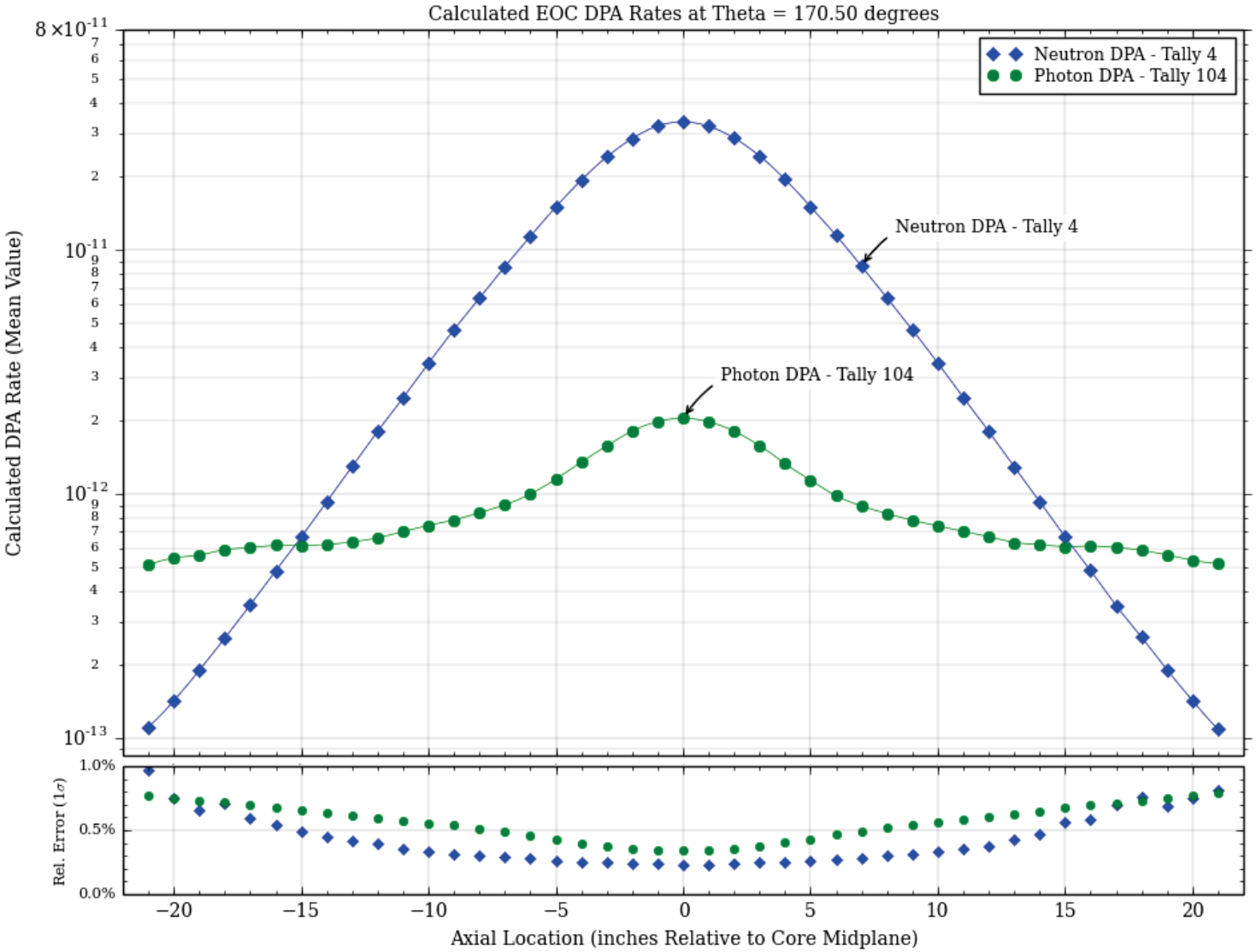

Fig. 4.1-15. Calculated EOC neutron and photon dpa rates in the HFIR RV at 170.5° from the +x axis.

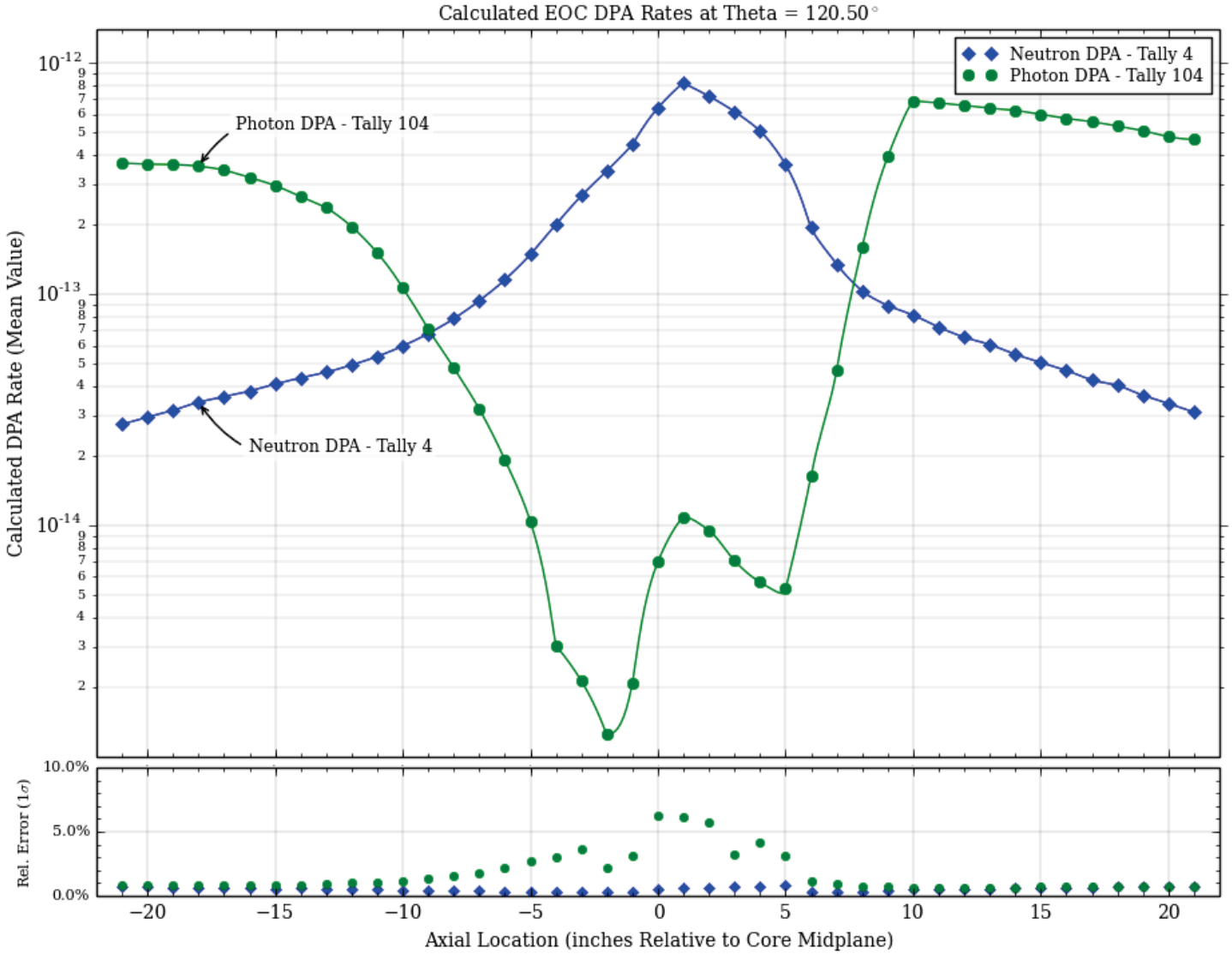

Fig. 4.1-16. Calculated EOC neutron and photon dpa rates in the HFIR RV at 120.5° from the +x axis.

Figures 4.1-3 through 4.1-5 present 2D contours of the LEU EOC neutron dpa rates averaged over the first ⅛" radial shell of RV base metal. Figures 4.1-3 and 4.1-4 contain subplots depicting a 90° arc of the neutron dpa rates at the RV inner surface. Figure 4.1-5 consists of a 140° arc of the RV inner surface showing all or parts of beam tubes HB-1 through HB-3 and the effect that these beam tubes have on the neutron dpa rates around the neighboring beam tube. As previously noted, the neutron dpa rate contours around beam tube HB-2 are nearly circular close to the beam tube and more oblate farther away from the beam tube. Similar behavior can be seen around beam tube HB-3. In the absence of the ion chamber near beam tube HB-1, the neutron dpa rate contour labeled with a *10* (equivalent to 1e-13 dpa/sec) would be expected to be nearly symmetric. However, as seen in Fig. 4.1-5, neutrons that exit beam tube HB-1 and travel toward beam tube HB-2 have a slightly larger effect on the 1e-13 contour line than neutrons traveling toward beam tube HB-2 after exiting beam tube HB-3. This is attributed to the reduced neutron attenuation (relative to water) of the lead and steel in the ion chamber adjacent to beam tube HB-1.

Plots of the photon dpa rates are presented in Figs. 4.1-6 and 4.1-7. These figures show a clear and significant (orders of magnitude) increase in both neutron and photon dpa rates in the vicinity of each of the four beam tubes that penetrate the RV. This is expected, because the material (typically air) inside each beam tube provides very little attenuation compared to any other path on which the core neutrons and photons could travel to reach the RV. This increase is most significant around the HB-2 beam tube. As seen in Fig. 3.2-1, this tube is oriented so that neutrons and photons produced in the core can stream from the core to the RV with very little scattering. In the other three beam tubes, the neutrons and photons generated in the core must make significant directional changes due to scattering inside the tube to travel in a direction that will allow them to transport through the minimally attenuating material in the beam tubes and eventually scatter into the RV. Figures 4.1-6 and 4.1-7 also show a smaller increase in the neutron dpa rates behind the ICs due to the reduced neutron attenuation capability of steel and lead relative to the water filling most of the region between the outer reflector and the RV. The ICs do, however, provide a significant (again, orders of magnitude) reduction in the photon dpa rates in the regions of the RV behind the ICs due to the enhanced photon attenuation capability of the steel and lead in the ICs relative to water. Also, as previously discussed, the effect of the ion chambers near beam tubes HB-1 and HB-4 on the photon dpa rates on the opposite side of these beam tubes can be seen in the upper portion of Fig. 4.1-6 and the lower portion of Fig. 4.1-7.

Figures 4.1-8 through 4.1-13 present detailed 1-D azimuthal traces of the neutron and photon dpa rates, as well as the associated 1σ relative error in the calculated dpa rates, at various axial heights of interest in the RV. In these figures, the azimuthal extent of the beam line internal material (typically air), the beam line wall (aluminum), the gap between the beam line and the associated RV nozzle opening (water) and, if present, the nozzle boss (steel) are each depicted by vertical bars of unique colors. The material internal to each beam line is shown in white, the beam tube walls are black, the water between the beam tube wall and the associated RV nozzle is teal, and the nozzle bosses around beam lines HB-1 and HB-4 are presented in gray. Most of these 1-D plots cover the full 360° azimuthal extent of the RV inner radius. However, Fig. 4.1-13 covers a limited azimuthal extent to provide additional detail for the individual tally bins near the vicinity of beam tube HB-2.

The results in Figs. 4.1-8 through 4.1-13 demonstrate that over most of the azimuthal extent of the RV and at all heights, the photon dpa rates are significantly higher than the neutron dpa rates. At the height of the lower girth weld, the photon dpa rates are roughly an order of magnitude larger than the corresponding neutron values. As previously discussed, the exceptions to this trend are the areas adjacent to the beam tubes and the areas behind the ICs. This is a peculiar aspect of HFIR that is contrary to the behavior in typical power reactors. The large volumes of beryllium and water between the core and the RV significantly reduce the neutron flux at the RV relative to a typical power reactor configuration where the RV is in closer proximity to the core. Additionally, the reflector and water between the core and the RV are both significant sources of photons that cause atomic displacements in the RV. As seen in Fig. 4.1-17, approximately 70%

of the photon dpa rate in the HFIR RV is due to neutron capture or neutron inelastic scattering that takes place in the various components of the beryllium reflector or the water between the reflector and the RV.

Figures 4.1-14 through 4.1-16 show the axial variation in neutron and photon dpa rates in the HFIR RV for various azimuthal locations. In all three of these figures, 0° is coincident with the +x axis of the MCNP model. This places the longitudinal axis of beam tube HB-2 at 180°. Figure 4.1-14 presents a 1-D trace of the neutron and photon dpa rates in the first 1/8" of the RV at an azimuthal location of 225.5°. This azimuthal location is located between beam tubes HB-2 and HB-3 and is representative of the axial shape of the neutron and photon dpa rates at azimuthal locations around the RV where the influence of the beam tubes and ICs is minimal. In these locations, the neutron dpa rates do not vary much more than a factor of 2 between the core midplane and the axial location of the lower RV girth weld (17" below core midplane). Figure 4.1-15 presents a 1-D trace of the neutron and photon dpa rates in the first ⅛" of the RV at an azimuthal location of 170.5°. This azimuthal location is just outboard of the RV nozzle penetration for beam tube HB-2. The significant effect of the beam tube on neutron dpa rates in the RV can be seen in this figure. Between the core midplane and the lower girth weld, there is a difference of nearly 2 orders of magnitude in the neutron dpa rates. Figure 4.1-16 presents a 1-D trace of the neutron and photon dpa rates in the first ⅛" of the RV at an azimuthal location of 120.5°. This azimuthal location is located behind the IC adjacent to beam tube HB-1. The increased photon attenuation of the lead and steel in the IC relative to the water it displaces leads to a decrease of more than 2 orders of magnitude in the photon dpa rates relative to nearby locations in the RV not shielded by the IC. Similarly, the reduced neutron attenuation of the lead and steel in the IC relative to the water it displaces leads to nearly a factor of 30 increase in the neutron dpa rates behind the IC compared to nearby locations in the RV not shielded by the IC.

In addition to quantifying the neutron and photon dpa rates in the vicinity of the RV/RV inner liner interface, calculations were performed to rank various HFIR components in terms of their importance to the dpa rates observed in the RV. An alternate version of the MCNP code (MCNPX) provides enhanced tally tagging capabilities to determine how much of a specific tallied response was due to a neutron or photon that originated in a specific cell of the model. Technically, all of the neutrons or photons that induce dpa in the RV are byproducts of a fission that occurred in one of the fueled zones of the core. However, the interactions these fission-induced neutrons and photons have with materials between their birth site in the core and the RV may define new birth regions for secondary neutrons or photons that subsequently deposit enough of their energy in the RV to displace an atom from its current lattice position. Essentially, any nonelastic (neutron) or nonCompton (photon) interaction that occurs between the fission-induced birth of a particle and the contribution of one of that particle's progeny to the response of interest results in the location of the nonelastic or nonCompton interaction being tagged as the birth region for a secondary particle. These secondary particles may also undergo nonelastic or nonCompton events, in which case they would cease to exist, and the cell in which they gave rise to new secondary particles would become the current birth cell associated with the given particle's history. For any given particle history, the last cell in which a nonelastic or nonCompton event occurs is tagged as being the birth cell for the fraction of the response of interest associated with that specific history.

For example, a neutron that is released as the result of a fission event and travels all the way to the RV having nothing but elastic scattering events before displacing an atom in the RV from its current lattice position is considered to have been born in the core. However, if a fission neutron travels all the way to the RV undergoing nothing but elastic scattering events, and then it undergoes an inelastic scattering event in the RV and the secondary neutron emitted as part of the (n,n') reaction subsequently causes an atomic displacement in the RV, then the RV is considered the birth cell for a fraction of the total dpa tallied in the RV. Similarly for photons, a fission photon that undergoes nothing but Compton scattering between

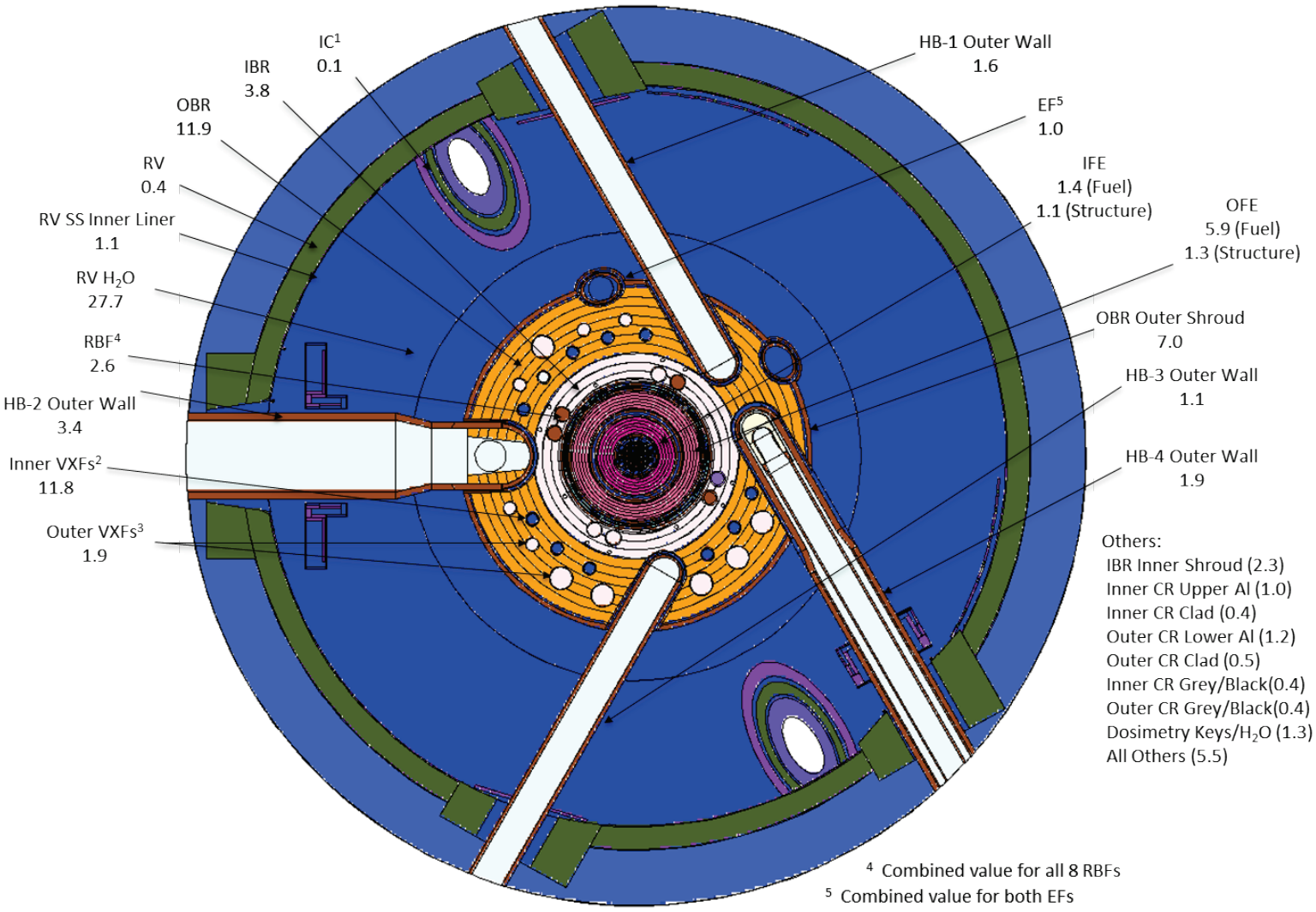

Fig. 4.1-17. Contributions to photon dpa rates in the HFIR RV by component. Values are from operations with an LEU core. Some values represent the total contribution to the RV photon dpa rate tally arising from multiple identical components (e.g., two geometrically equivalent ICs are located on opposite sides of the RV, near beam tubes HB-1 and HB-3. The IC contribution of 0.1% represents the sum of the contributions from both ICs**).**

the fission site and the RV before causing an atomic displacement would be tallied as having been born in the core. If a photon (either a fission photon or a photon created by any nonfission neutron interaction anywhere in the model) that was involved in a pair production reaction in the beryllium reflector resulted in one or both of the subsequent photons traveling to the RV without having any other nonCompton events and eventually depositing enough energy in the RV to cause an atomic displacement, then the cell in the outer reflector where the original pair production event occurred would be tagged as the birth cell for a fraction of the RV photon-induced dpa rate tally. In general, the last geometric cell in which a neutron undergoes a nonelastic interaction (or a photon undergoes a nonCompton event) before contributing to the response of interest is tagged as the birth cell for a fraction of the response of interest.

Figure 4.1-17 shows how much of the photon dpa rate tally in the RV inner liner at EOC for an LEU core is born in various regions of HFIR. Figure 4.1-18 presents the same cell-by-cell contribution fraction for the RV inner liner neutron dpa rate tally. As previously mentioned, Fig. 4.1-17 shows that the water inboard of the RV and the components contained between the inner and outer shrouds of the beryllium reflector (including the shrouds themselves) are responsible for nearly 70% of the photon-induced atomic displacements in the RV. Conversely, the fueled regions of the core only contribute slightly more than 7% of the photon dpa rate in the RV. The low core contribution to the photon dpa rates in the RV is driven by the presence of significant quantities of heavy, dense elements in the LEU core: 127 kg of uranium in a U-Mo alloy as opposed to 10.1 kg of uranium (as U_3O_8) in an aluminum matrix for the HEU core. The self-shielding effect of these heavy metals in the LEU core, combined with the large volume of light materials (e.g., beryllium, aluminum, water) between the core and the RV lead to the rather peculiar situation in which the photon dpa rates are typically dominant relative to the neutron dpa rates in the RV, because the lighter materials are significant sources of photons. Both capture (n,γ) and inelastic ([n,n'], $[n,\alpha]$, [n,p], etc.) reactions in these lighter elements are excellent sources of secondary photons.

Figure 4.1-18 demonstrates that nearly ⅔ (65.3%) of the neutron dpa rate tally in the first ⅛" of the RV base metal is due to fission neutrons that experience nothing other than elastic scattering from the time they are born until they contribute to the tally. Several neutron inelastic interactions are disappearance events (e.g., $[n,\alpha]$, [n,p],[n,d). While these interactions are excellent sources of secondary gammas, the interacting neutron is absorbed. Other neutron inelastic interactions such as inelastic scattering (n,n') or (n,2n) or (n,3n) reactions, do produce secondary neutrons. However, the product neutrons from these reactions are generally significantly degraded in energy relative to the neutron initiating the reaction (which is also removed from consideration through absorption). These lower energy secondary neutrons are significantly attenuated in the light elements inboard of the RV. As seen in Fig. 4.1-18, only 3.6% of the neutron dpa rate tally in the RV is due to neutrons born in the inner (2.5%) and outer (1.1) regions of the beryllium reflector. However, neutrons that survive the journey from the core to the vicinity of the RV liner can have inelastic interactions with the steels of the RV, the RV liner, the RV nozzles, or the aluminum of the beam tube walls. When a neutron inelastic event occurs locally in some portion of the RV, the recoil energy of the atom involved in the inelastic event can be greater than the relatively small (25 eV for iron) amount of energy required to displace an atom from its original lattice location. If the recoil energy of the displaced atom is more than twice the displacement threshold energy, this displaced atom, generally referred to as a *primary knock-on atom* (PKA) can displace an additional atom. Because the secondary neutrons released in the inelastic event will have a spectrum of energies, the recoil energy of the displaced atoms will also have varying energies. Both the secondary neutrons from inelastic interactions and the PKAs they generate, as well as any neutron interacting elastically in the RV, can induce an entire cascade of atomic displacements. Also, neutron inelastic interactions occurring in the portion of a beam tube wall that is very near the RV can yield secondary neutrons that will have a very short path through any water to reach the RV and contribute to the dpa rate tally in the RV. As seen from Fig. 4.1–18, more than ¼ (27.8%) of all neutron-induced atomic displacements in the RV are caused by neutrons that are born locally in either the RV, the RV liner, the beam tube walls, the beam tube nozzles, or the various dosimetry keys around any of the beam tubes.

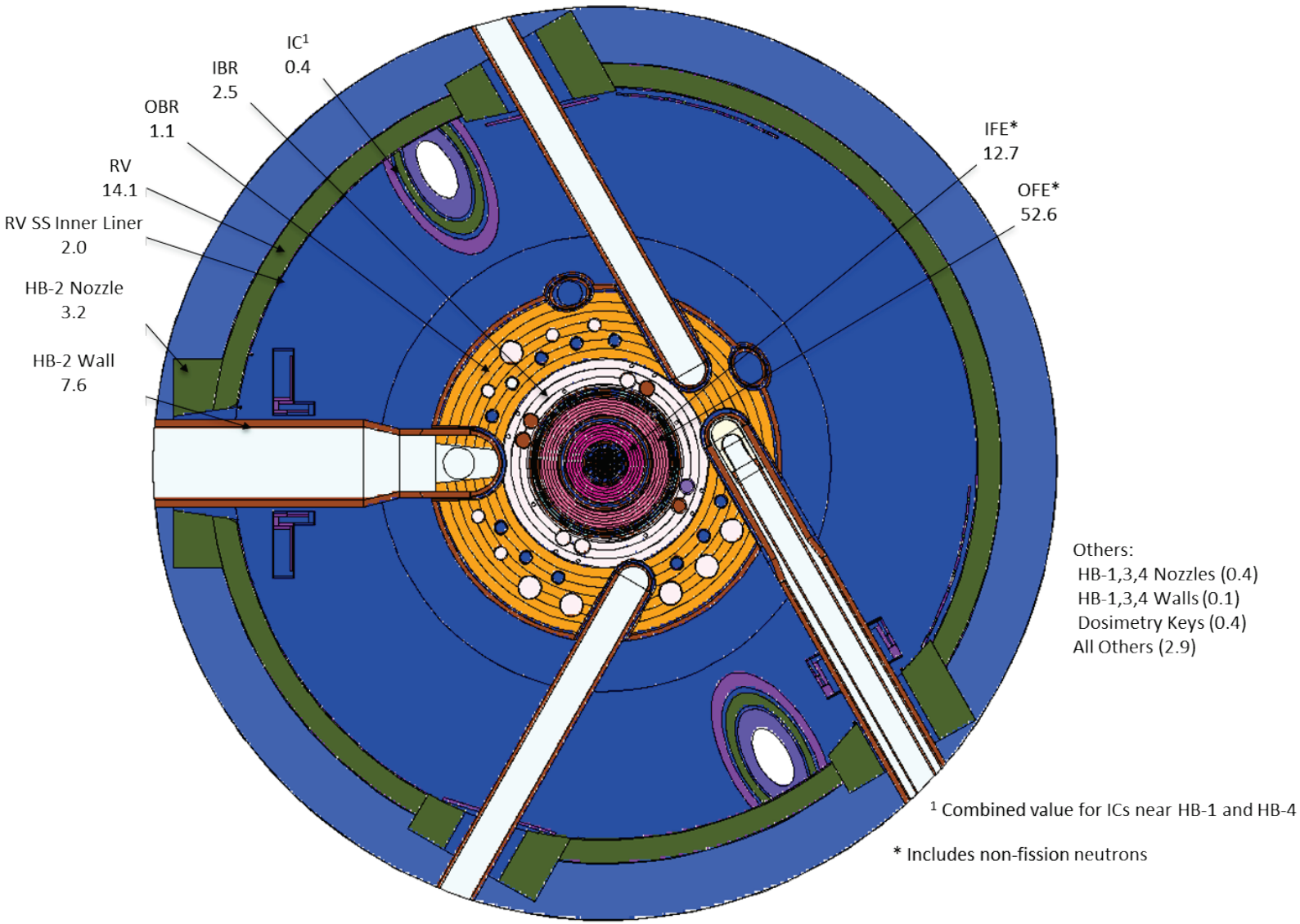

Fig. 4.1-18. Contributions to neutron dpa rates in the HFIR RV by component. Values are from operations with an LEU core. The IC contribution of 0.4% represents the sum of the contributions from the IC near beam tube HB-1 and the IC near beam tube HB-3.

4.2 LEU EOC/BOC DPA RATE RATIOS

With the exception of the magnitude of the prompt photon dpa rates, the shape of the BOC dpa rates tallies (both neutron and prompt photon) are quite similar to those seen in the EOC dpa rate tallies. Therefore, no separate set of LEU BOC neutron and photon dpa rate plots is given.

Figures 4.2-1 through 4.2-5 present 1-D azimuthal traces of the EOC/BOC ratio of the neutron and prompt photon dpa rates at a various axial heights in the HFIR RV. Although not shown explicitly, the statistical uncertainty in the BOC results is consistent with EOC results presented in the plots of Sect. 4.1 (i.e., predominantly below 1%). The error bars at each azimuthal location on these figures represent the 95% confidence intervals appropriate for a ratio, because they are calculated by taking the square root of the sum of the square of the EOC relative error and the square of the BOC relative error. From Figs. 4.2-1 through 4.2-5, it is obvious that the neutron dpa rates are much less affected by time-in-cycle than are the prompt photon dpa rates. The neutron dpa rates at 360 azimuthal locations for 5 separate axial heights generally do not vary by more than $\pm 5\%$ between BOC and EOC. Although the thermal flux in the core must increase from BOC and EOC in order to maintain a constant power throughout the cycle, this increase in thermal neutron population should have no noticeable impact on RV damage, because thermal neutrons that leak out of the core have very little chance of migrating to the RV and causing atomic displacements. This is due to the large volume of highly reflecting materials (beryllium) and highly attenuating materials (water and control elements) between the core and the RV.

The larger population of thermal neutrons in and around the core at EOC will, however, lead to an increase in the prompt photon production rate from capture reactions in and around the core. Furthermore, as the control elements move throughout the cycle, the heavy elements (Eu and Ta) in the control elements are relocated to positions above or below the axial extent of the core. This leaves a material (Al) that is much less effective at attenuating photons in the direct transport path between the core and the RV. Therefore, the prompt photon dpa rate in the RV will increase. For the LEU core analyzed, this increase is typically between 15–20% in the axial portion of the RV that extends from the height of the core axial midplane down to the lower RV girth weld.

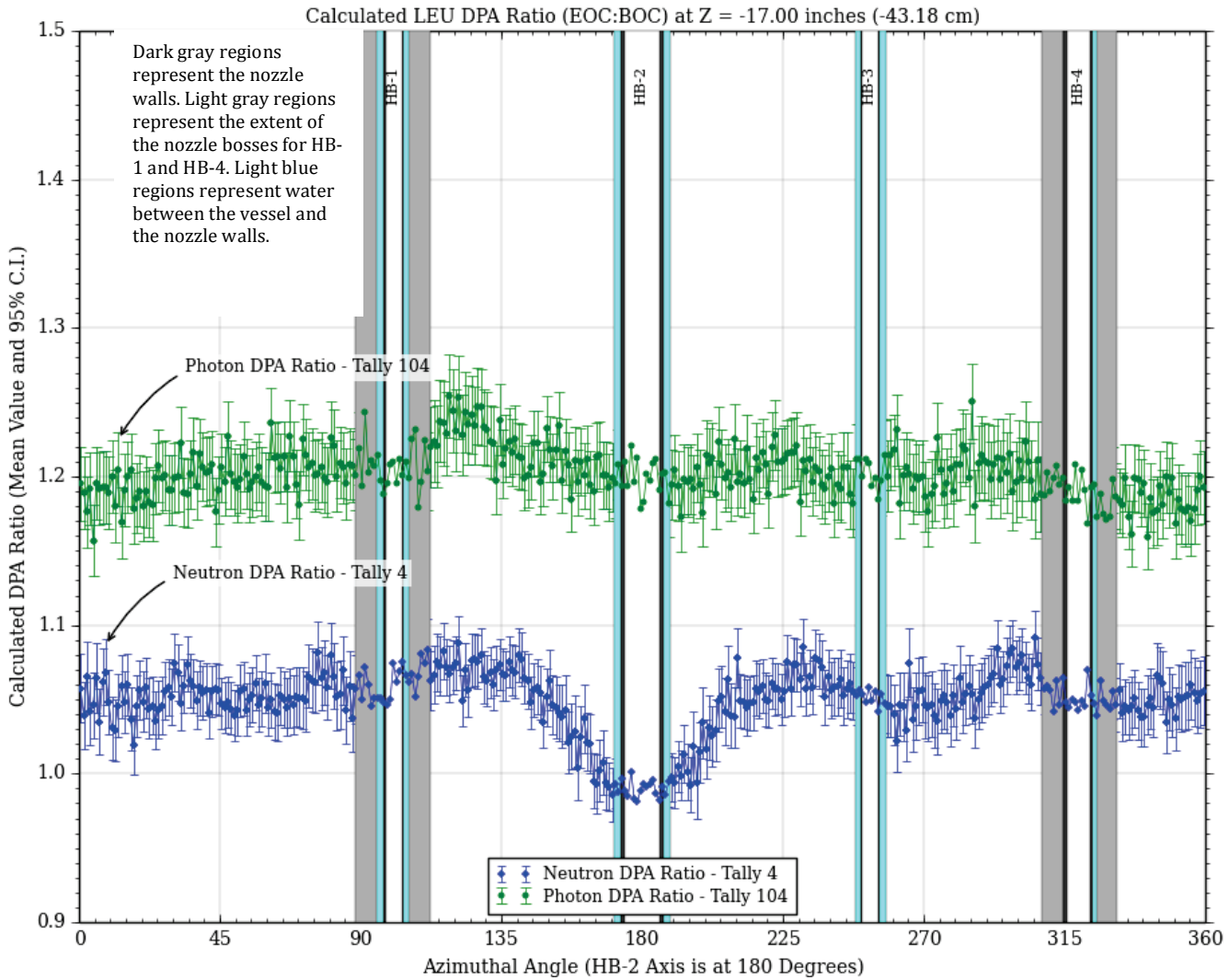

Fig. 4.2-1. LEU EOC/BOC neutron and photon dpa rate ratios at the elevation of the girth weld (17 inches below the HFIR core midplane). The presence of beam tubes HB-1 through HB-4 affect the calculated in-vessel dpa rates for several inches above/below the physical extent of these vessel penetrations. Therefore, the azimuthal extent of all four beam tubes at the core axial midplane is depicted on all dpa rate plots regardless of axial location.

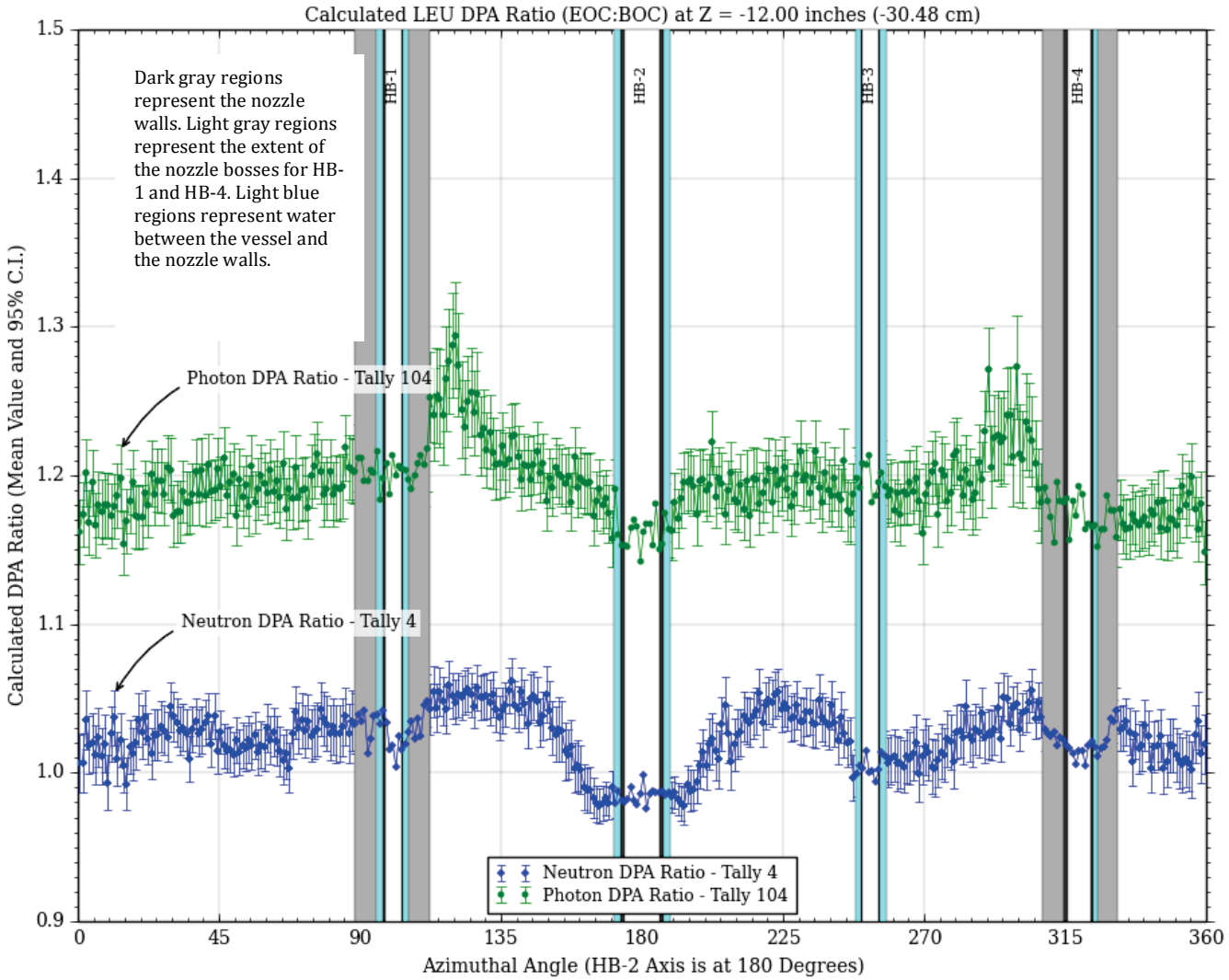

Fig. 4.2-2. LEU EOC/BOC neutron and photon dpa rate ratios at 12 inches below the HFIR core midplane. The presence of beam tubes HB-1 through HB-4 affect the calculated in-vessel dpa rates for several inches above/below the physical extent of these vessel penetrations. Therefore, the azimuthal extent of all four beam tubes at the core axial midplane is depicted on all dpa rate plots, regardless of axial location.

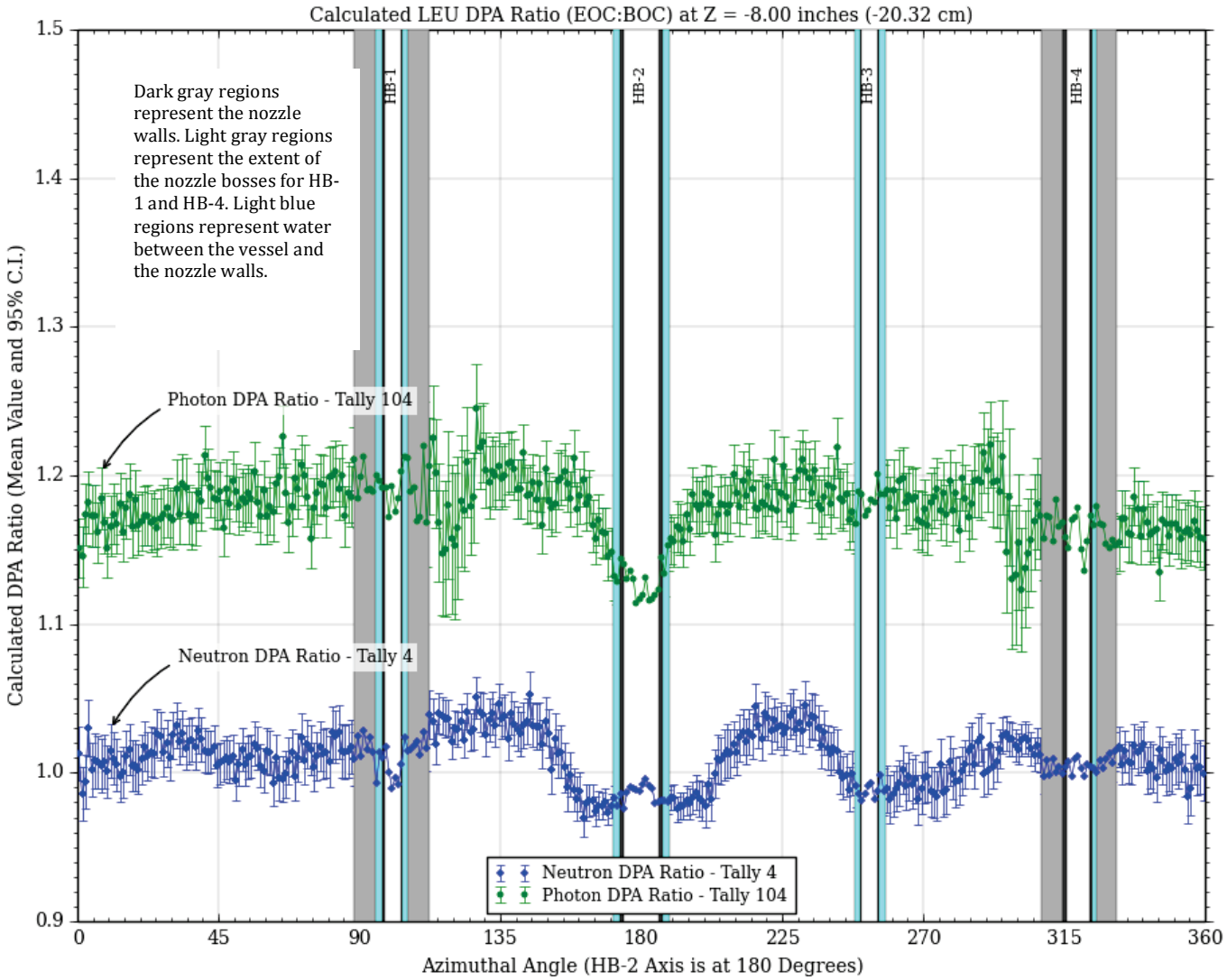

Fig. 4.2-3. LEU EOC/BOC neutron and photon dpa rate ratios at 8 inches below the HFIR core midplane. The presence of beam tubes HB-1 through HB-4 affect the calculated in-vessel dpa rates for several inches above/below the physical extent of these vessel penetrations. Therefore, the azimuthal extent of all four beam tubes at the core axial midplane is depicted on all dpa rate plots, regardless of axial location.

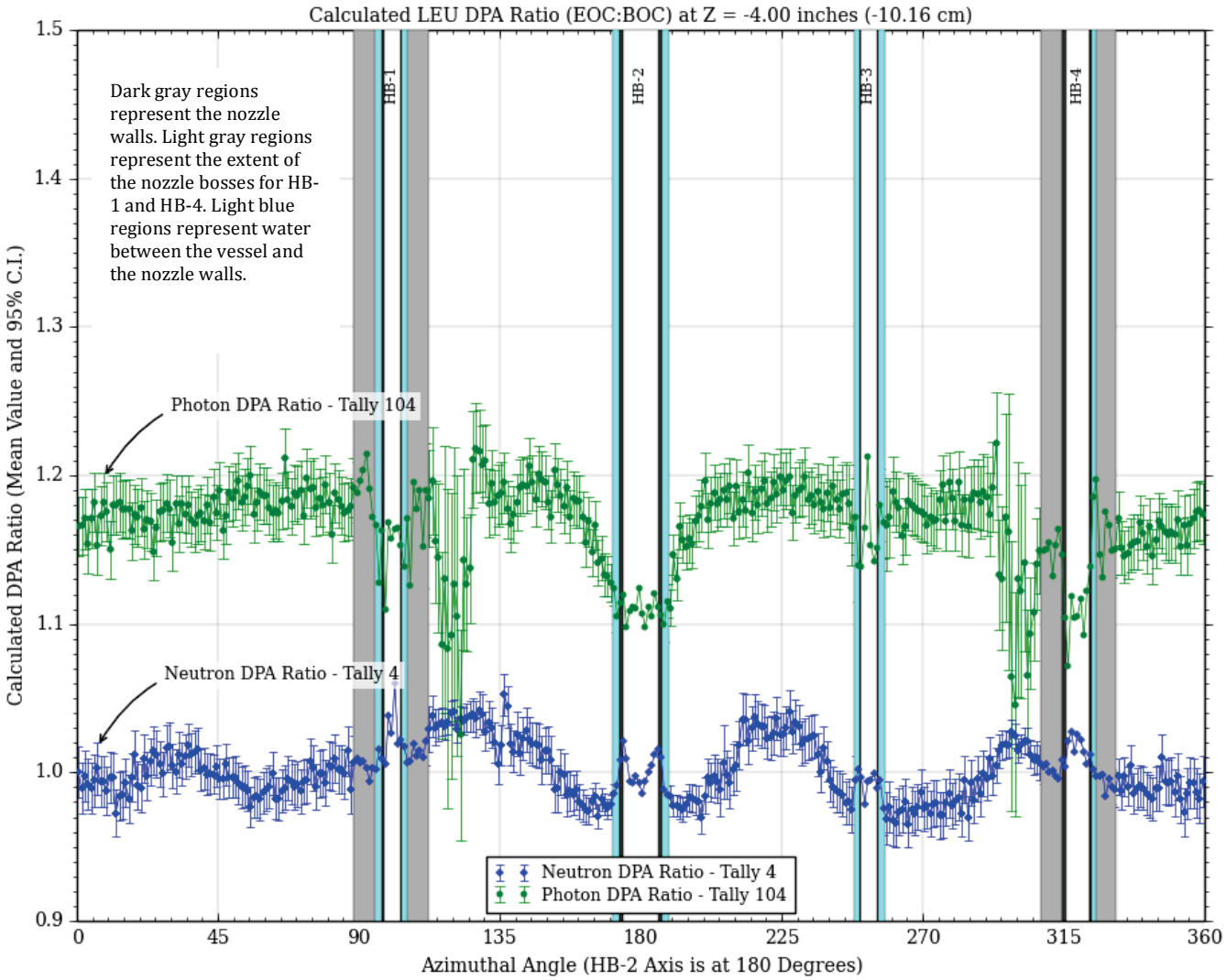

Fig. 4.2-4. LEU EOC/BOC neutron and photon dpa rate ratios at 4 inches below the HFIR core midplane. The presence of beam tubes HB-1 through HB-4 affect the calculated in-vessel dpa rates for several inches above/below the physical extent of these vessel penetrations. Therefore, the azimuthal extent of all four beam tubes at the core axial midplane is depicted on all dpa rate plots, regardless of axial location.

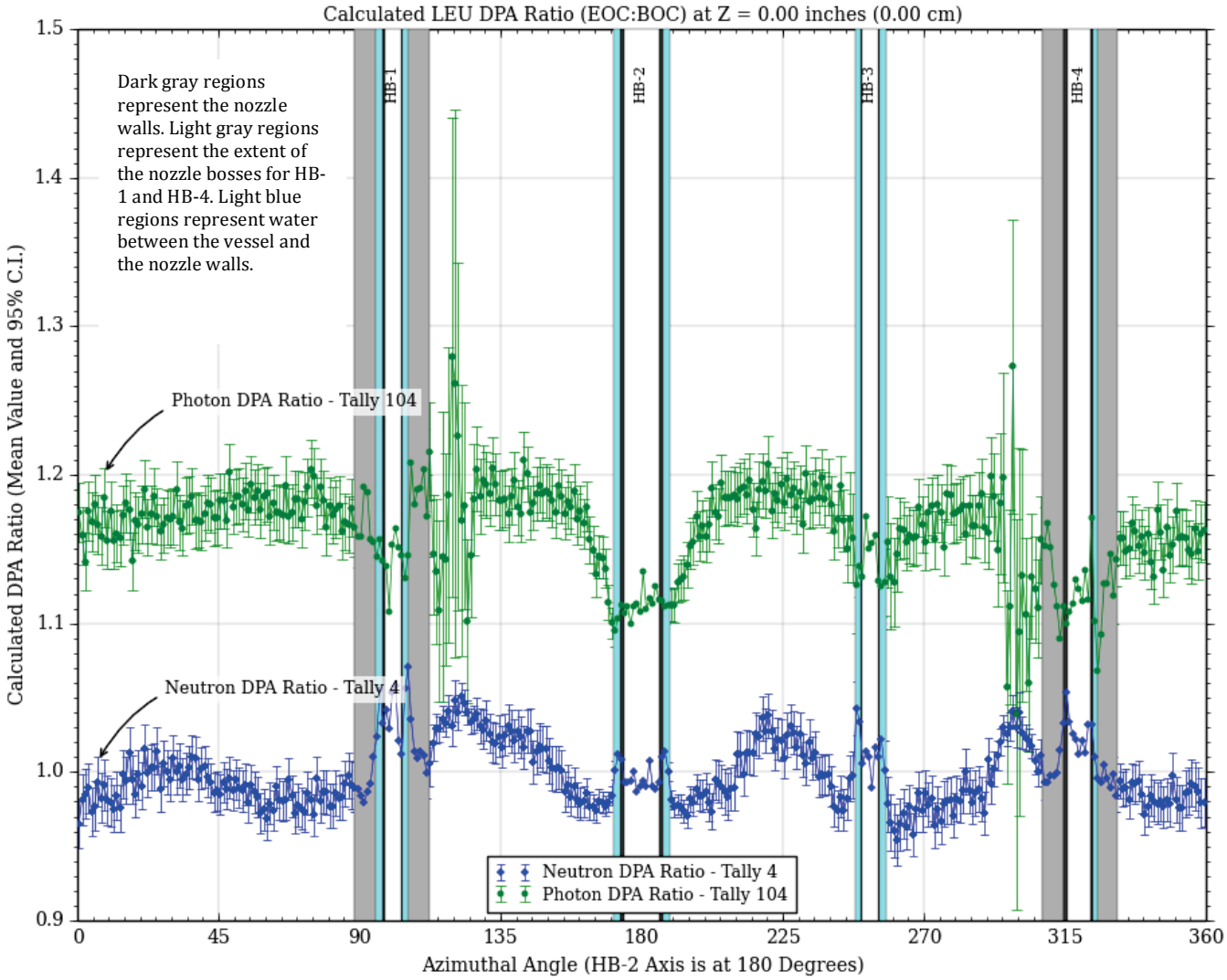

Fig. 4.2-5. LEU EOC/BOC neutron and photon dpa rate ratios at the HFIR core midplane. The presence of beam tubes HB-1 through HB-4 affect the calculated in-vessel dpa rates for several inches above/below the physical extent of these vessel penetrations. Therefore, the azimuthal extent of all four beam tubes at the core axial midplane is depicted on all dpa rate plots, regardless of axial location.

4.3 LEU/HEU DPA RATE RATIOS

Figures 4.3-1 through 4.3-10 present 1-D azimuthal traces of the LEU/HEU ratio of the neutron and photon dpa rates at a various axial heights in the HFIR RV. The LEU/HEU ratios at BOC are presented in Figs. 4.3-1 through 4.3-5. The same ratios at EOC are given in Figs. 4.3-6 through 4.3-10. The error bars on these figures represent a 95% confidence interval for a ratio that is already based on a root-mean-square (RMS) combination of both the LEU and HEU results. Although not shown explicitly, the statistical uncertainty in the HEU results is consistent with LEU results (i.e., predominantly below 1%). The HEU results were obtained from the same MCNP output files generated for the Risner and Blakeman [2] calculations.

From Figs. 4.3-1 through 4.3-10, it can be seen that the LEU/HEU neutron dpa rate ratios change very little throughout the cycle. At BOC and EOC, the LEU neutron dpa rates in the first ⅛" of the RV are roughly 5–7% lower than the HEU values. An increase in fast fissions due to the increased quantity of ^{238}U in the LEU core should lower the fast neutron population leaving the core and is thus the likely cause of the slight reduction in neutron dpa rates at the RV.

Figures 4.3-1 through 4.3-10 show that the LEU/HEU photon dpa rate ratios are affected more significantly than the LEU/HEU neutron dpa rate ratios. At BOC, the LEU/HEU photon dpa rate ratios are typically around 0.8. This ~20% reduction in photon dpa rates in the RV is attributed to the increased self-attenuation of photons in the LEU core relative to the HEU core. As previously discussed, the LEU core contains ~127 Kg of uranium in a U-Mo alloy as opposed to ~10.1 Kg of uranium (as U_3O_8) in an aluminum matrix for the HEU core. Both the increased mass of uranium (in the same core volume) and the use of molybdenum as opposed to aluminum in the fuel plates lead to an increased amount of high Z materials in the core, which will increase the photon attenuation of the core.

At EOC, the LEU/HEU photon dpa rate ratios in the RV are roughly 0.7. As previously discussed, the photon dpa rates in the RV increase by 15–20% over the course of an operational cycle (see Figs. 4.2-1 through 4.2-5). Conversely, as seen in Figs. 4.3-11 through 4.3-15, the HEU EOC photon dpa rates in the RV are typically 30–40% higher than the corresponding values at BOC. This is consistent with the changes in thermal flux in the reflector region over the considered LEU operating cycle. From Tables 8 and 9 of Ilas and Primm [1], it can be seen that the increase in thermal flux in the reflector regions is greater for the existing HEU core design (~30–40%) than for the proposed LEU core design (~10–15%). In these same regions, the epithermal and fast fluxes change by <5% over the cycle for both HEU and LEU cores. Because of the greater change in thermal flux over an operating cycle of an HEU core relative to the proposed LEU core, the increase in photon production from thermal captures over a typical HEU operating cycle should also be more pronounced than for operations with the proposed LEU core. This increased production of high- energy photons from thermal capture will result in the observed increase in photon dpa rates in the RV due to HEU core operations relative to LEU core operations.

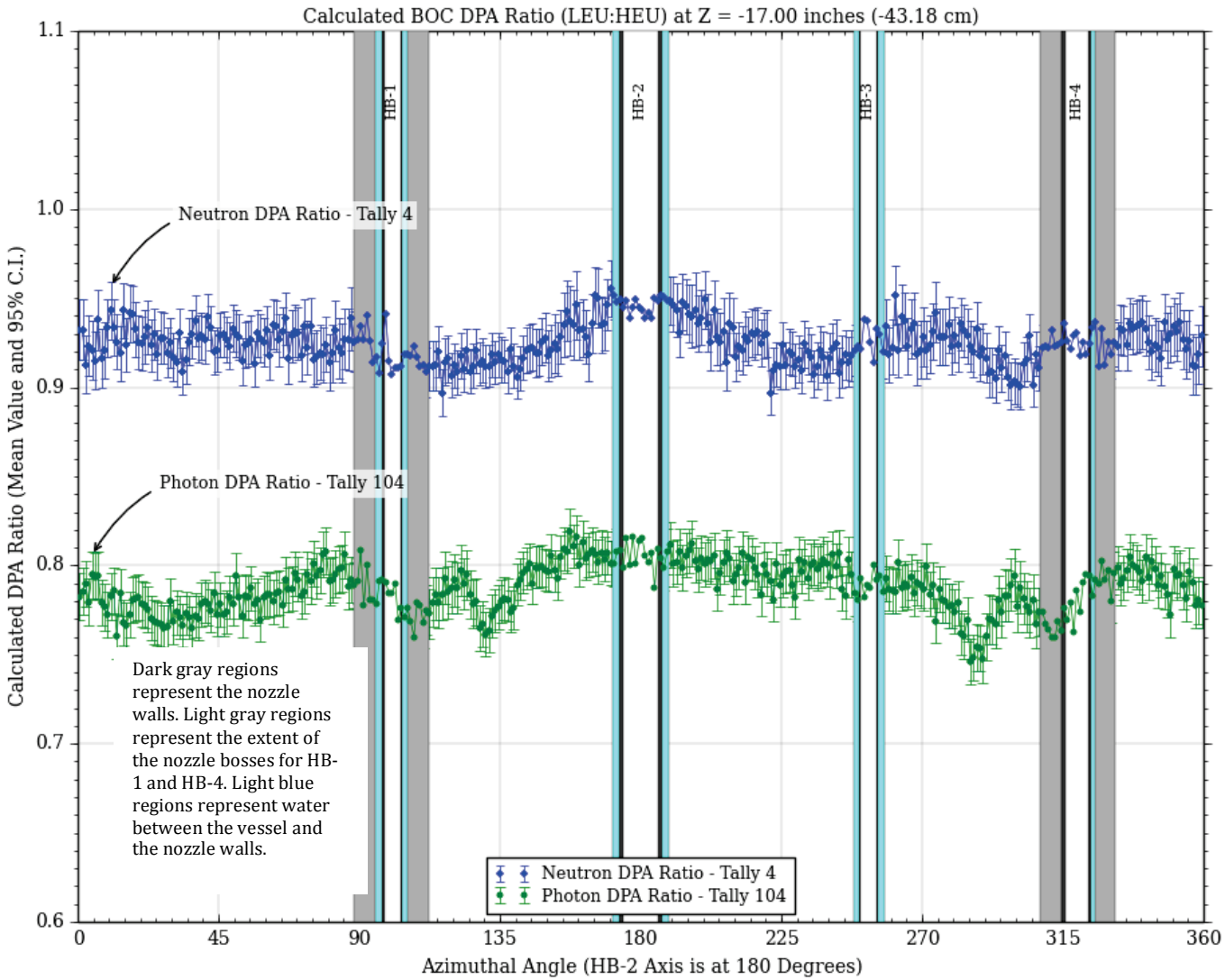

Fig. 4.3-1. BOC LEU/HEU neutron and photon dpa rate ratios at the elevation of the girth weld (17 inches below the HFIR core midplane). The presence of beam tubes HB-1 through HB-4 affect the calculated in-vessel dpa rates for several inches above/below the physical extent of these vessel penetrations. Therefore, the azimuthal extent of all four beam tubes at the core axial midplane is depicted on all dpa rate plots, regardless of axial location.

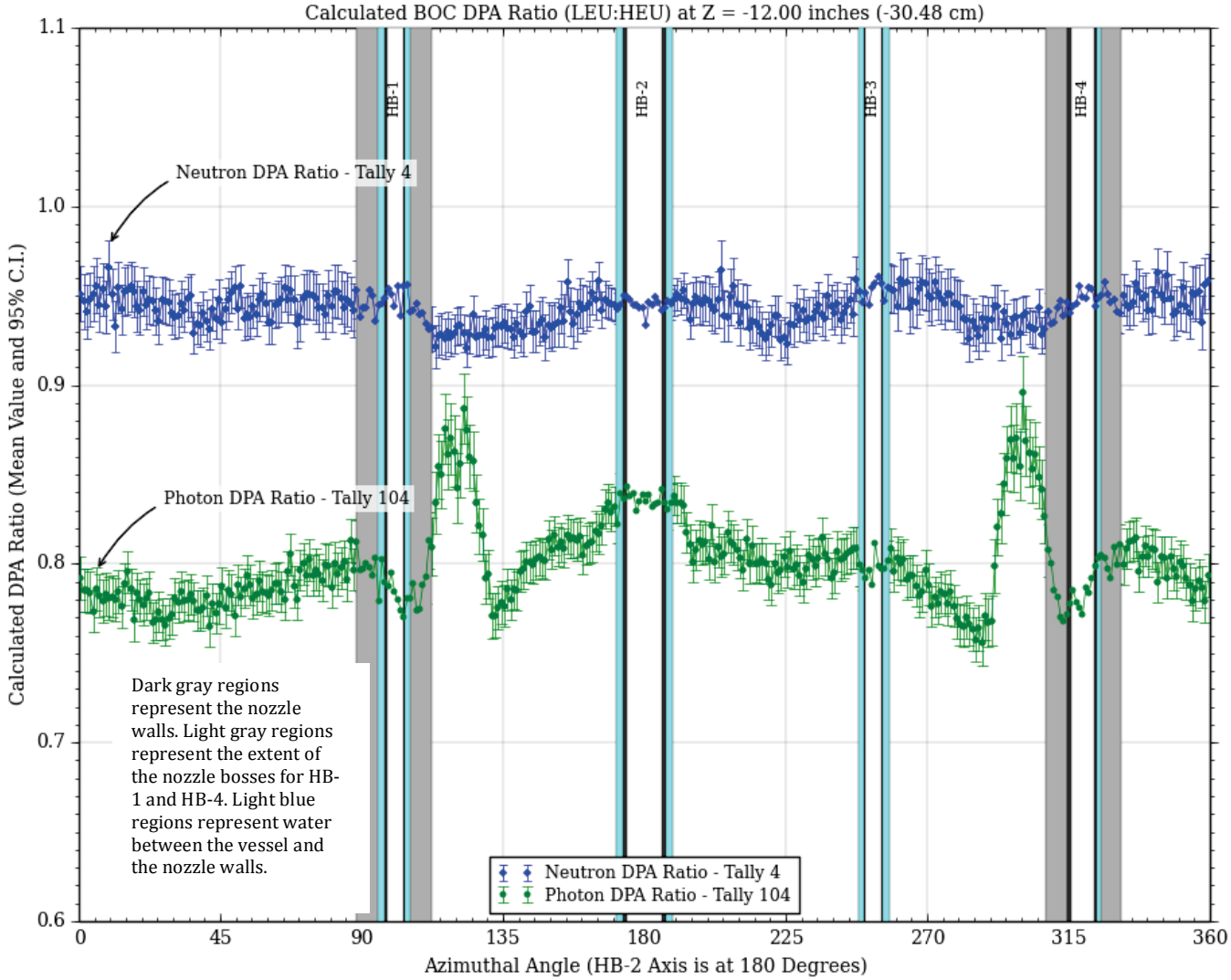

Fig. 4.3-2. BOC LEU/HEU neutron and photon dpa rate ratios at 12 inches below the HFIR core midplane. The presence of beam tubes HB-1 through HB-4 affect the calculated in-vessel dpa rates for several inches above/below the physical extent of these vessel penetrations. Therefore, the azimuthal extent of all four beam tubes at the core axial midplane is depicted on all dpa rate plots, regardless of axial location.

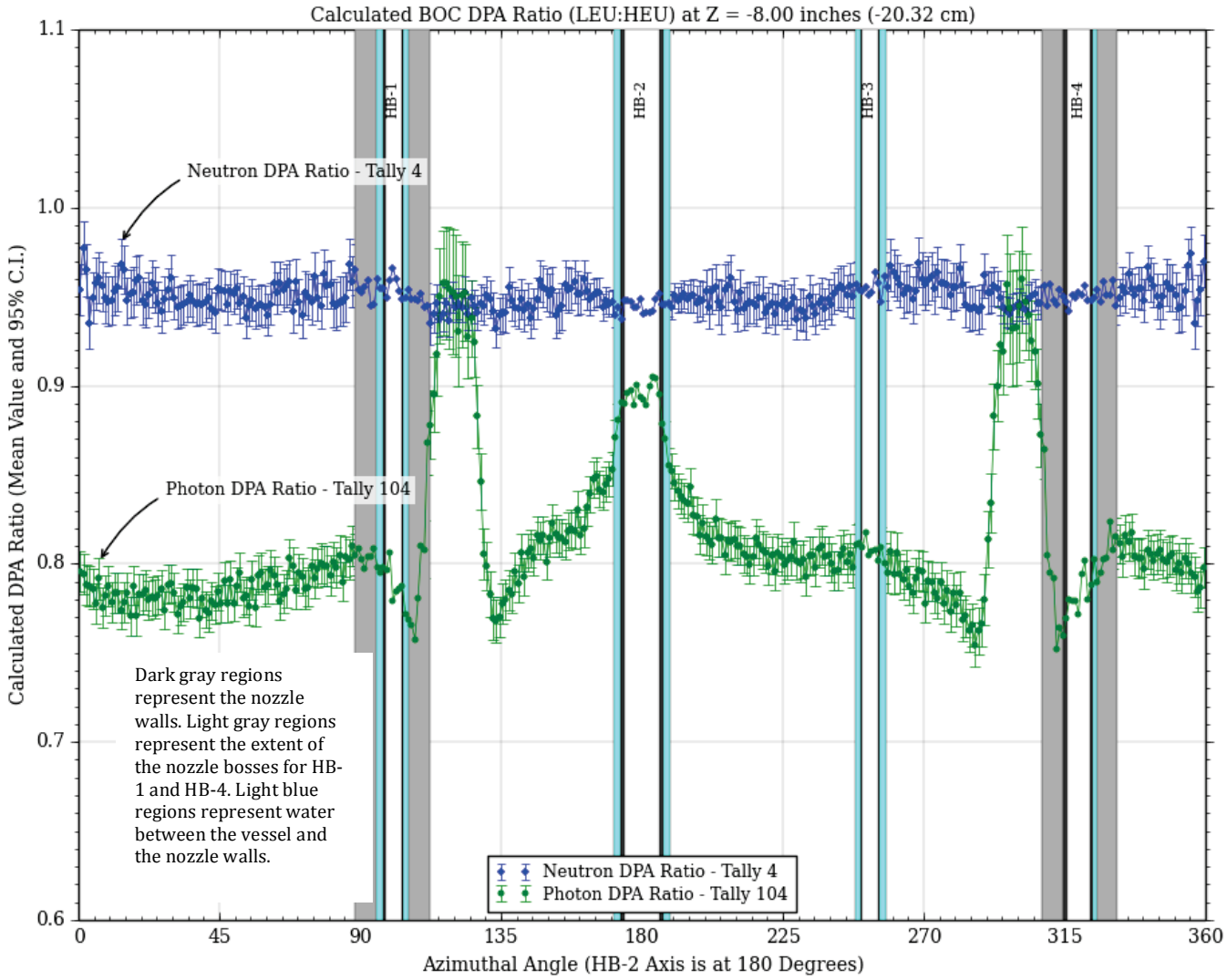

Fig. 4.3-3. BOC LEU/HEU neutron and photon dpa rate ratios at 8 inches below the HFIR core midplane. The presence of beam tubes HB-1 through HB-4 affect the calculated in-vessel dpa rates for several inches above/below the physical extent of these vessel penetrations. Therefore, the azimuthal extent of all four beam tubes at the core axial midplane is depicted on all dpa rate plots, regardless of axial location.

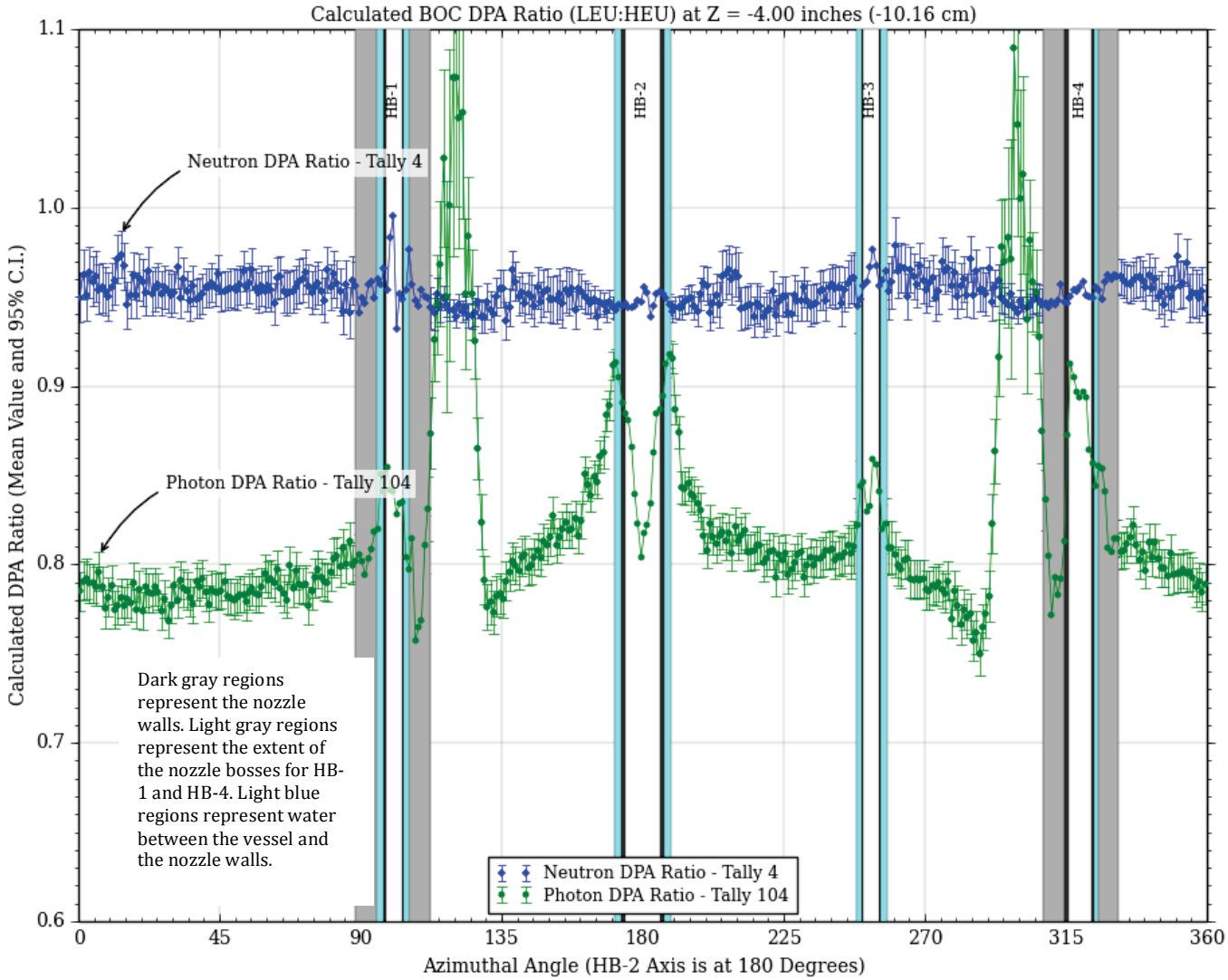

Fig. 4.3-4. BOC LEU/HEU neutron and photon dpa rate ratios at 4 inches below the HFIR core midplane. The presence of beam tubes HB-1 through HB-4 affect the calculated in-vessel dpa rates for several inches above/below the physical extent of these vessel penetrations. Therefore, the azimuthal extent of all four beam tubes at the core axial midplane is depicted on all dpa rate plots, regardless of axial location.

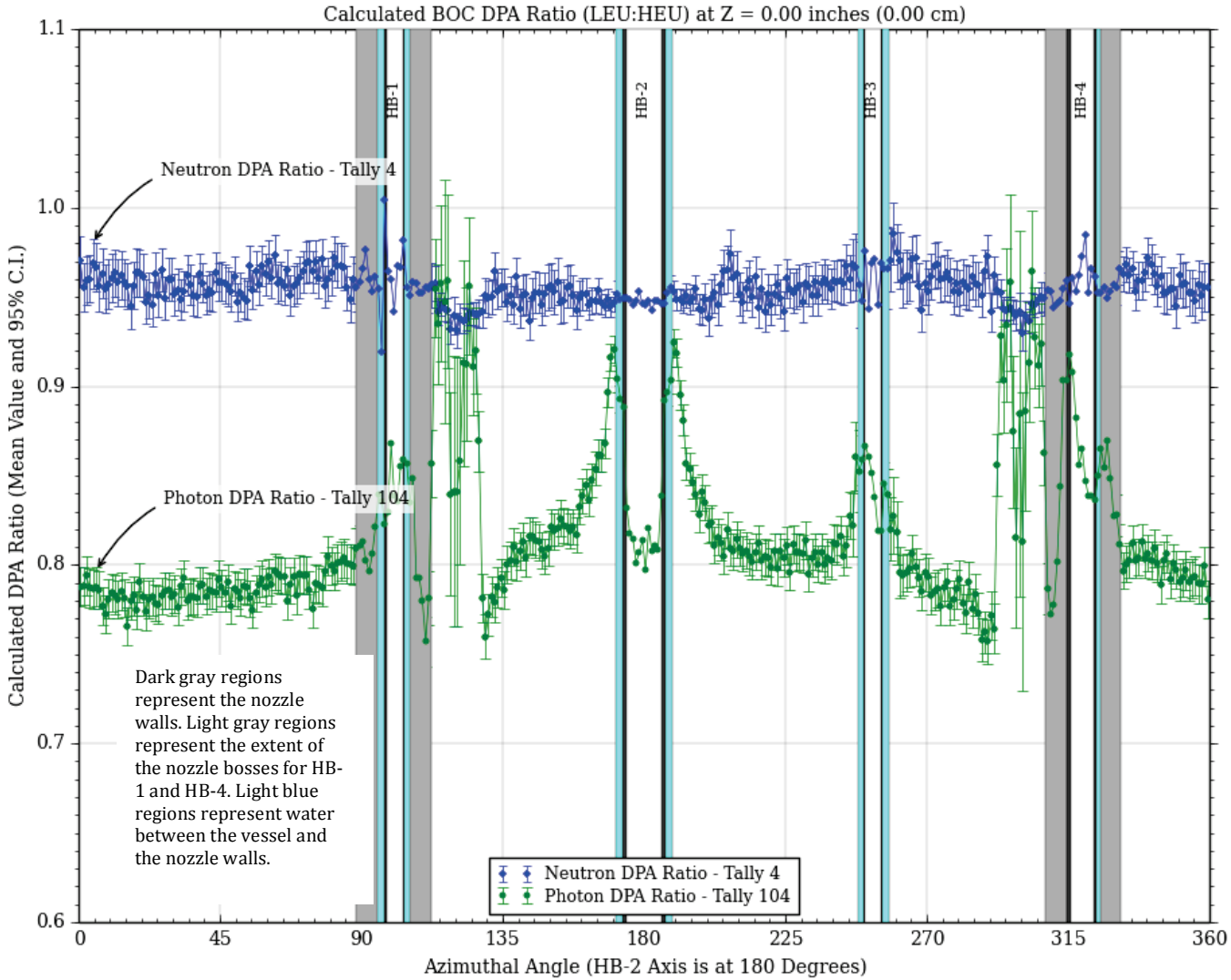

Fig. 4.3-5. BOC LEU/HEU neutron and photon dpa rate ratios at the HFIR core midplane. The presence of beam tubes HB-1 through HB-4 affect the calculated in-vessel dpa rates for several inches above/below the physical extent of these vessel penetrations. Therefore, the azimuthal extent of all four beam tubes at the core axial midplane is depicted on all dpa rate plots, regardless of axial location.

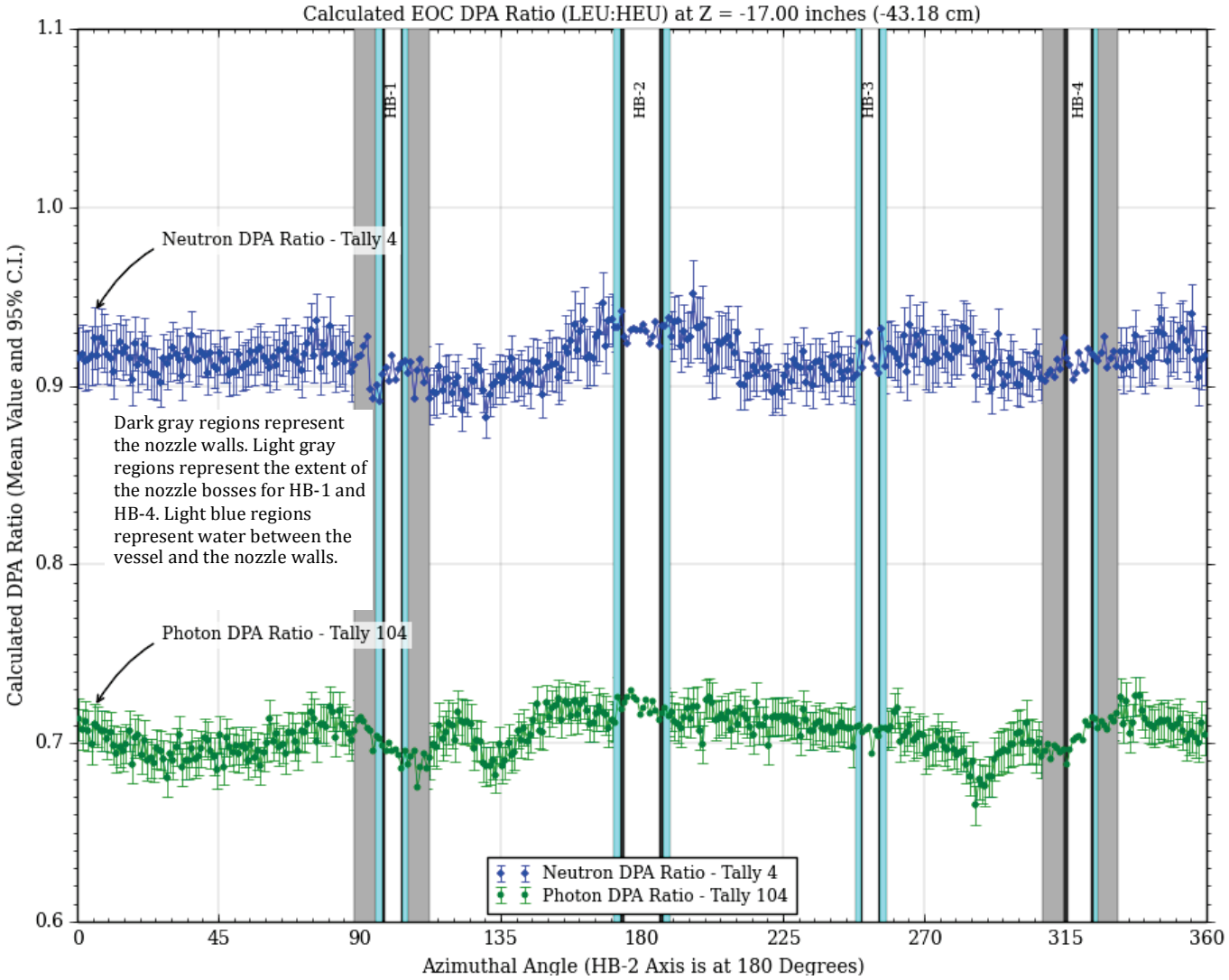

Fig. 4.3-6. EOC LEU/HEU neutron and photon dpa rate ratios at the elevation of the girth weld (17 inches below the HFIR core midplane). The presence of beam tubes HB-1 through HB-4 affect the calculated in-vessel dpa rates for several inches above/below the physical extent of these vessel penetrations. Therefore, the azimuthal extent of all four beam tubes at the core axial midplane is depicted on all dpa rate plots, regardless of axial location.

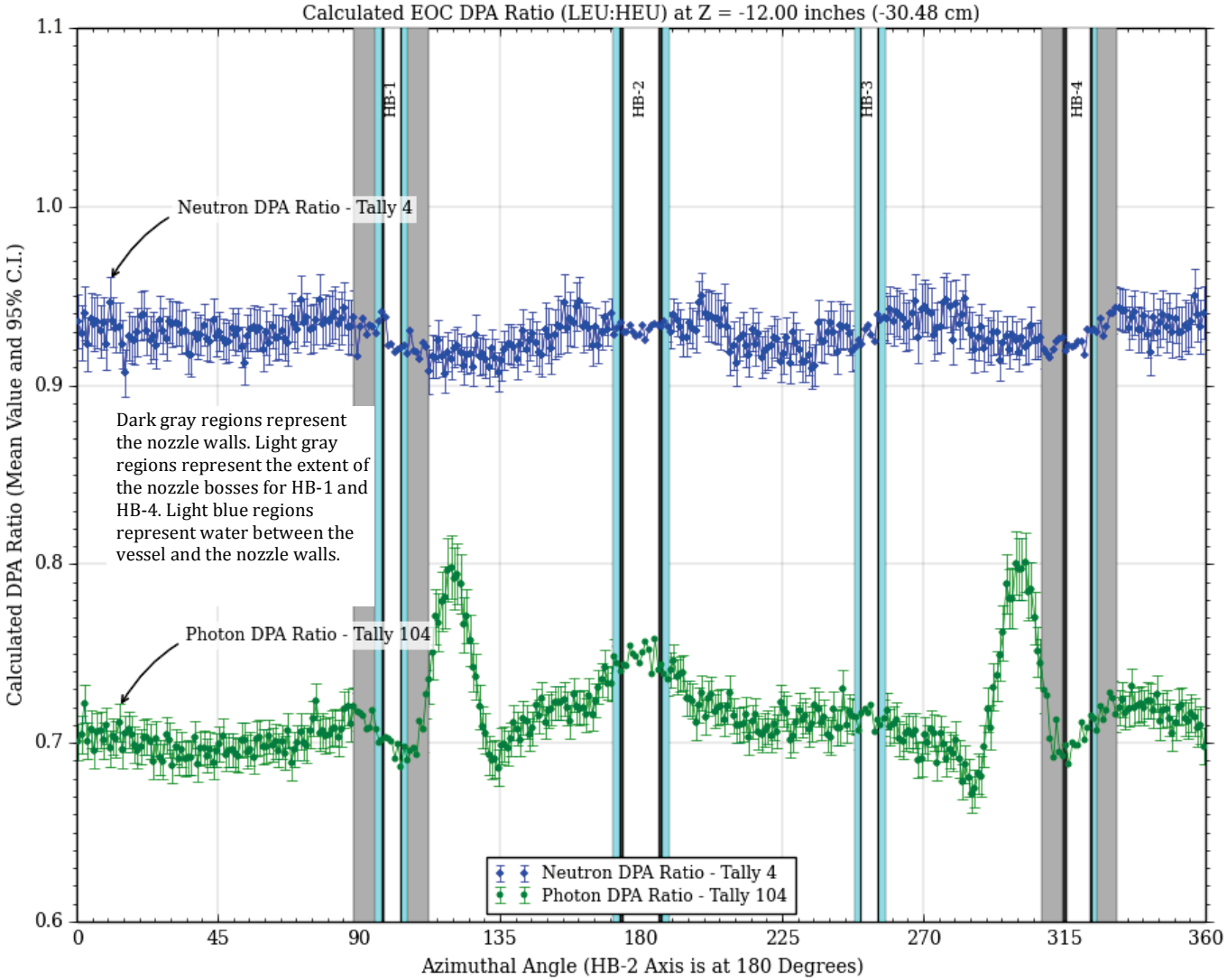

Fig. 4.3-7. EOC LEU/HEU neutron and photon dpa rate ratios at 12 inches below the HFIR core midplane. The presence of beam tubes HB-1 through HB-4 affect the calculated in-vessel dpa rates for several inches above/below the physical extent of these vessel penetrations. Therefore, the azimuthal extent of all four beam tubes at the core axial midplane is depicted on all dpa rate plots, regardless of axial location.

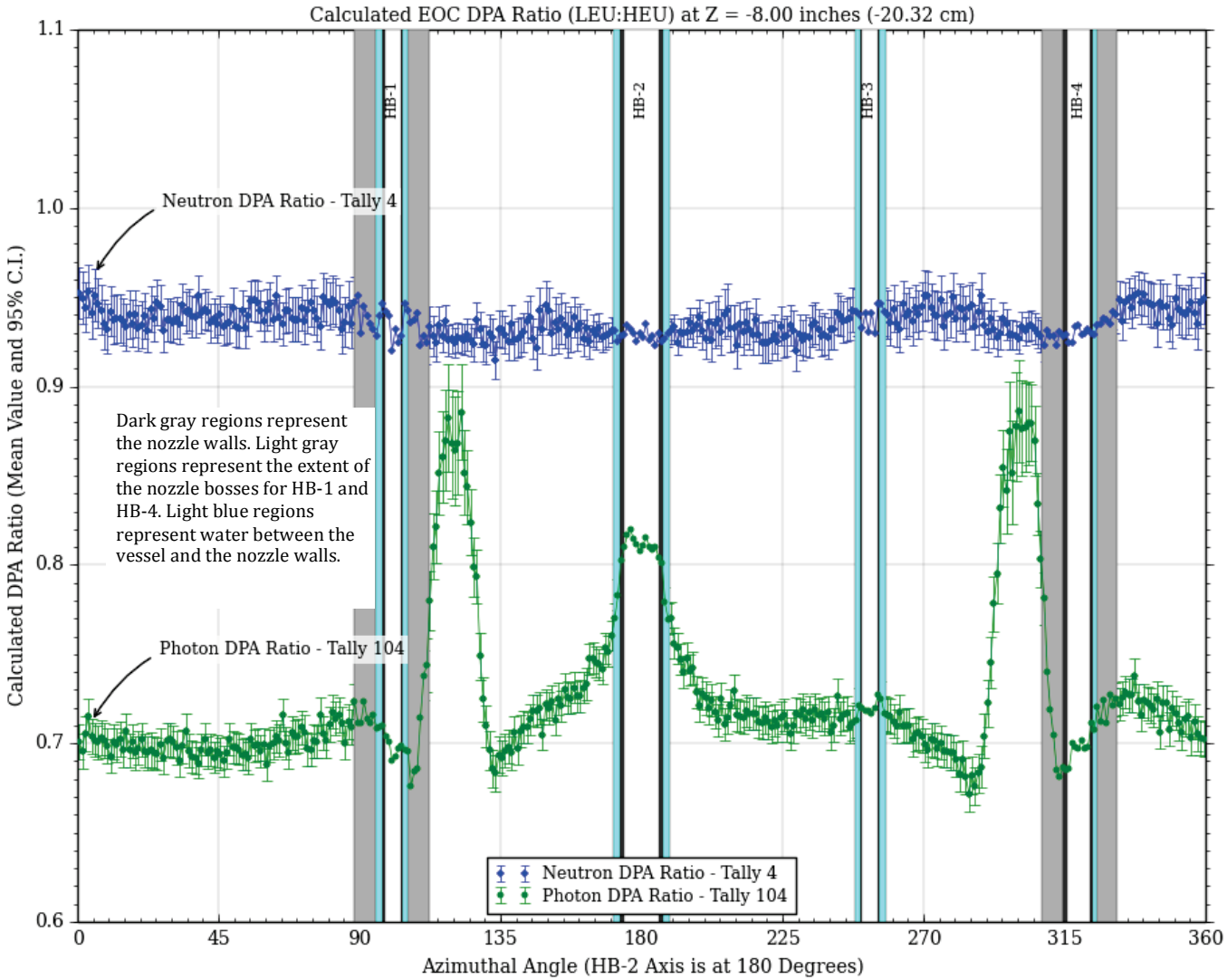

Fig. 4.3-8. EOC LEU/HEU neutron and photon dpa rate ratios at 8 inches below the HFIR core midplane. The presence of beam tubes HB-1 through HB-4 affect the calculated in-vessel dpa rates for several inches above/below the physical extent of these vessel penetrations. Therefore, the azimuthal extent of all four beam tubes at the core axial midplane is depicted on all dpa rate plots, regardless of axial location.

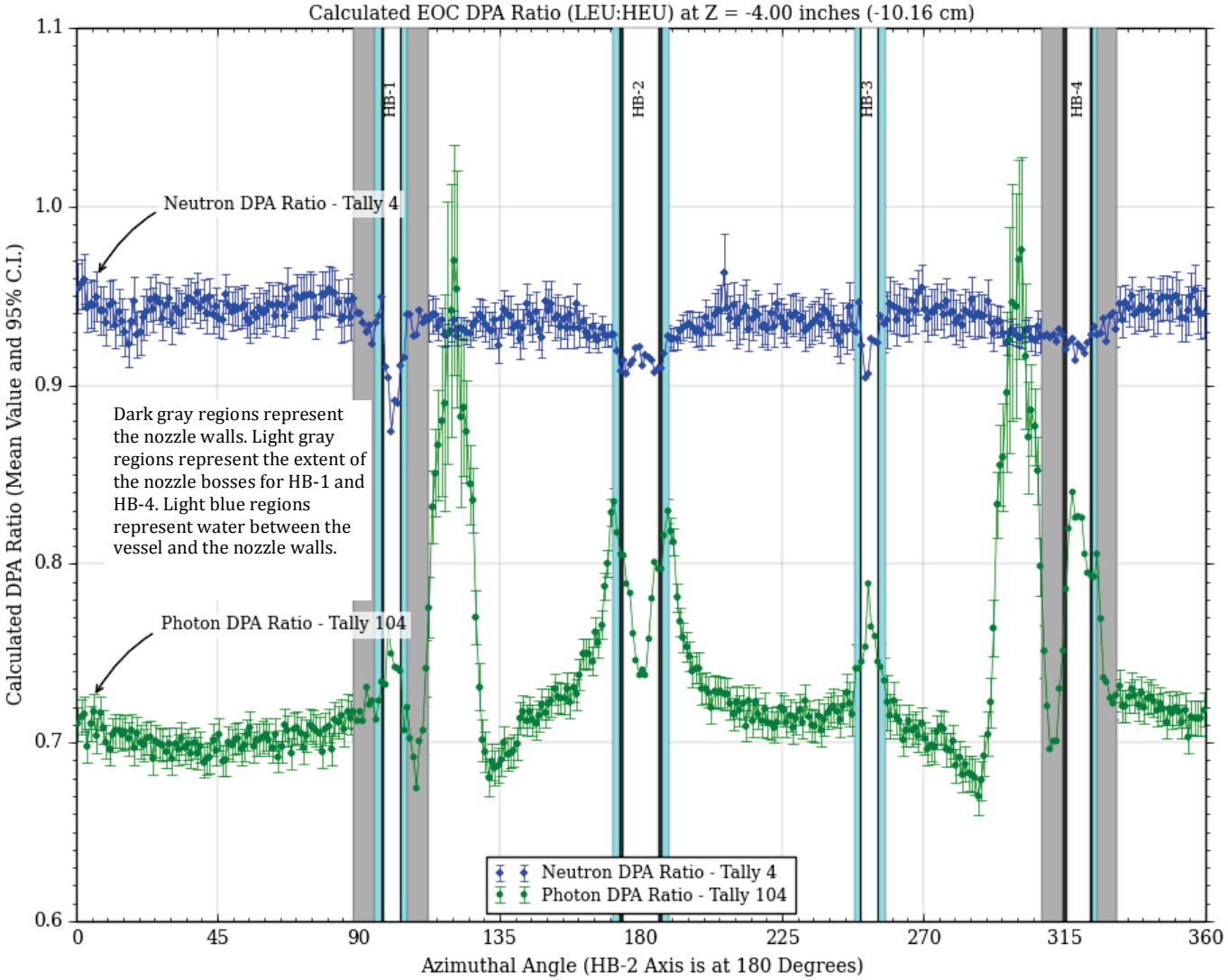

Fig. 4.3-9. EOC LEU/HEU neutron and photon dpa rate ratios at 4 inches below the HFIR core midplane. The presence of beam tubes HB-1 through HB-4 affect the calculated in-vessel dpa rates for several inches above/below the physical extent of these vessel penetrations. Therefore, the azimuthal extent of all four beam tubes at the core axial midplane is depicted on all dpa rate plots, regardless of axial location.

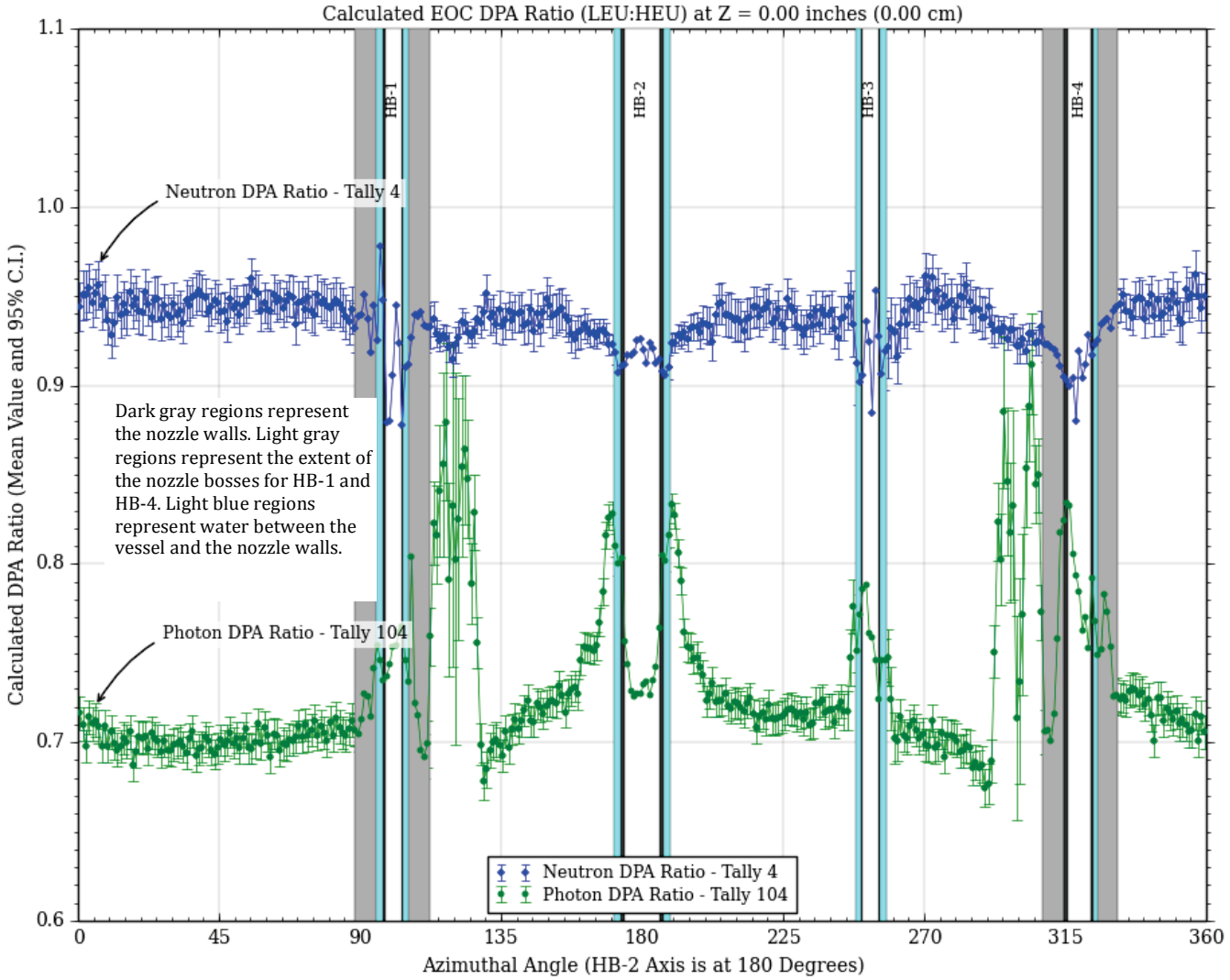

Fig. 4.3-10. EOC LEU/HEU neutron and photon dpa rate ratios at the HFIR core midplane. The presence of beam tubes HB-1 through HB-4 affect the calculated in-vessel dpa rates for several inches above/below the physical extent of these vessel penetrations. Therefore, the azimuthal extent of all four beam tubes at the core axial midplane is depicted on all dpa rate plots, regardless of axial location.

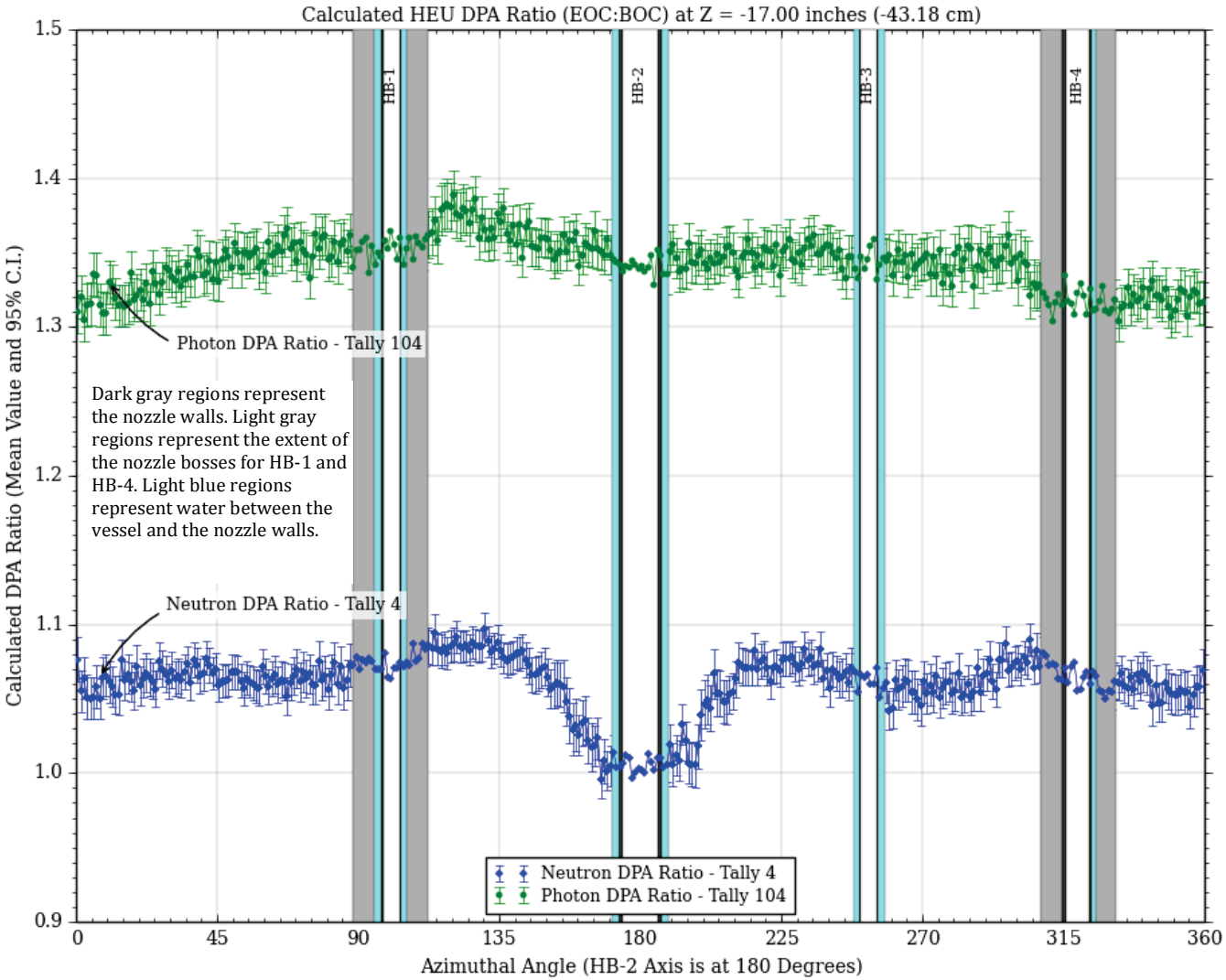

Fig. 4.3-11. HEU EOC/BOC neutron and photon dpa rate ratios at the elevation of the girth weld (17 inches below the HFIR core midplane). The presence of beam tubes HB-1 through HB-4 affect the calculated in-vessel dpa rates for several inches above/below the physical extent of these vessel penetrations. Therefore, the azimuthal extent of all four beam tubes at the core axial midplane is depicted on all dpa rate plots, regardless of axial location.

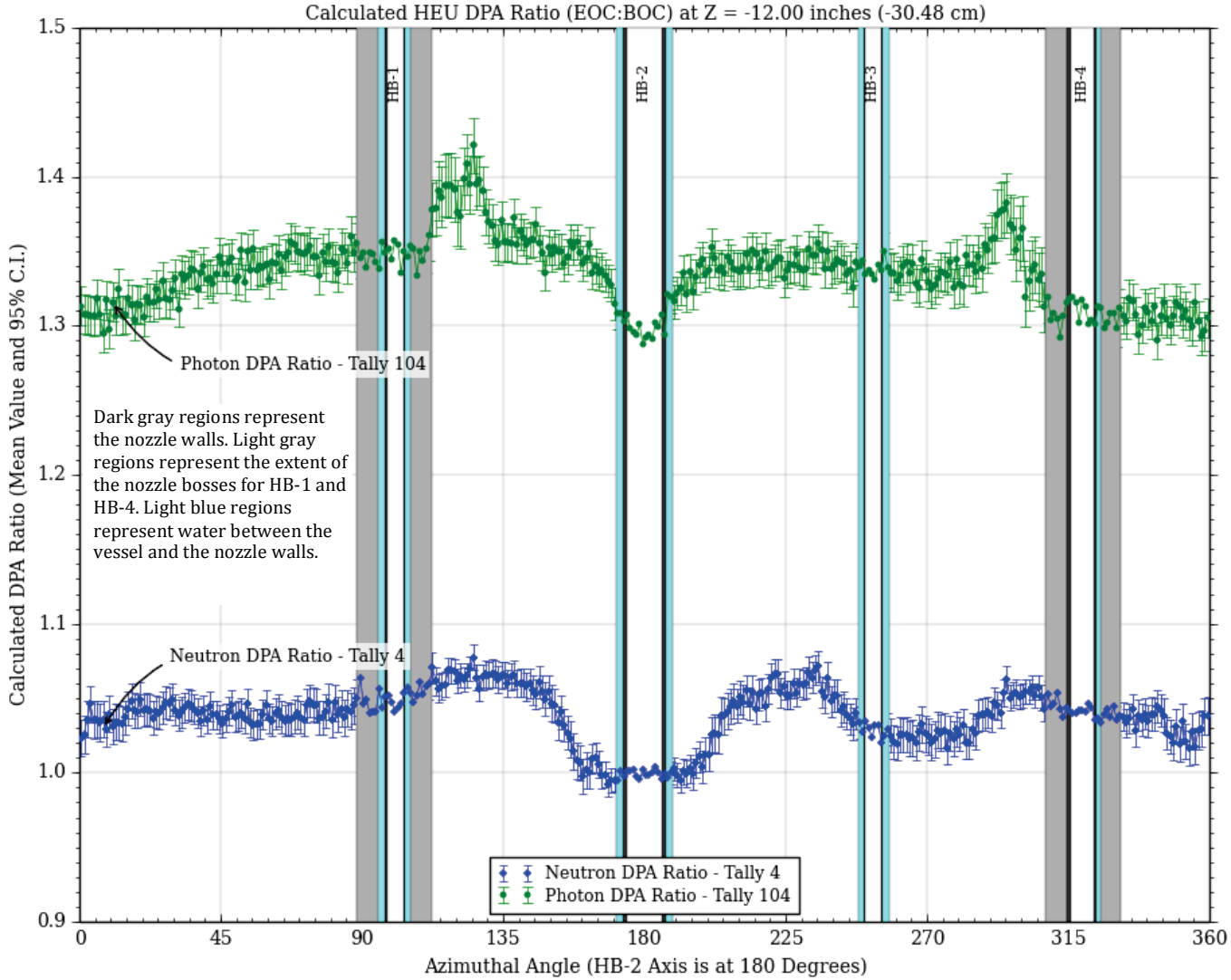

Fig. 4.3-12. HEU EOC/BOC neutron and photon dpa rate ratios at 12 inches below the HFIR core midplane. The presence of beam tubes HB-1 through HB-4 affect the calculated in-vessel dpa rates for several inches above/below the physical extent of these vessel penetrations. Therefore, the azimuthal extent of all four beam tubes at the core axial midplane is depicted on all dpa rate plots, regardless of axial location.

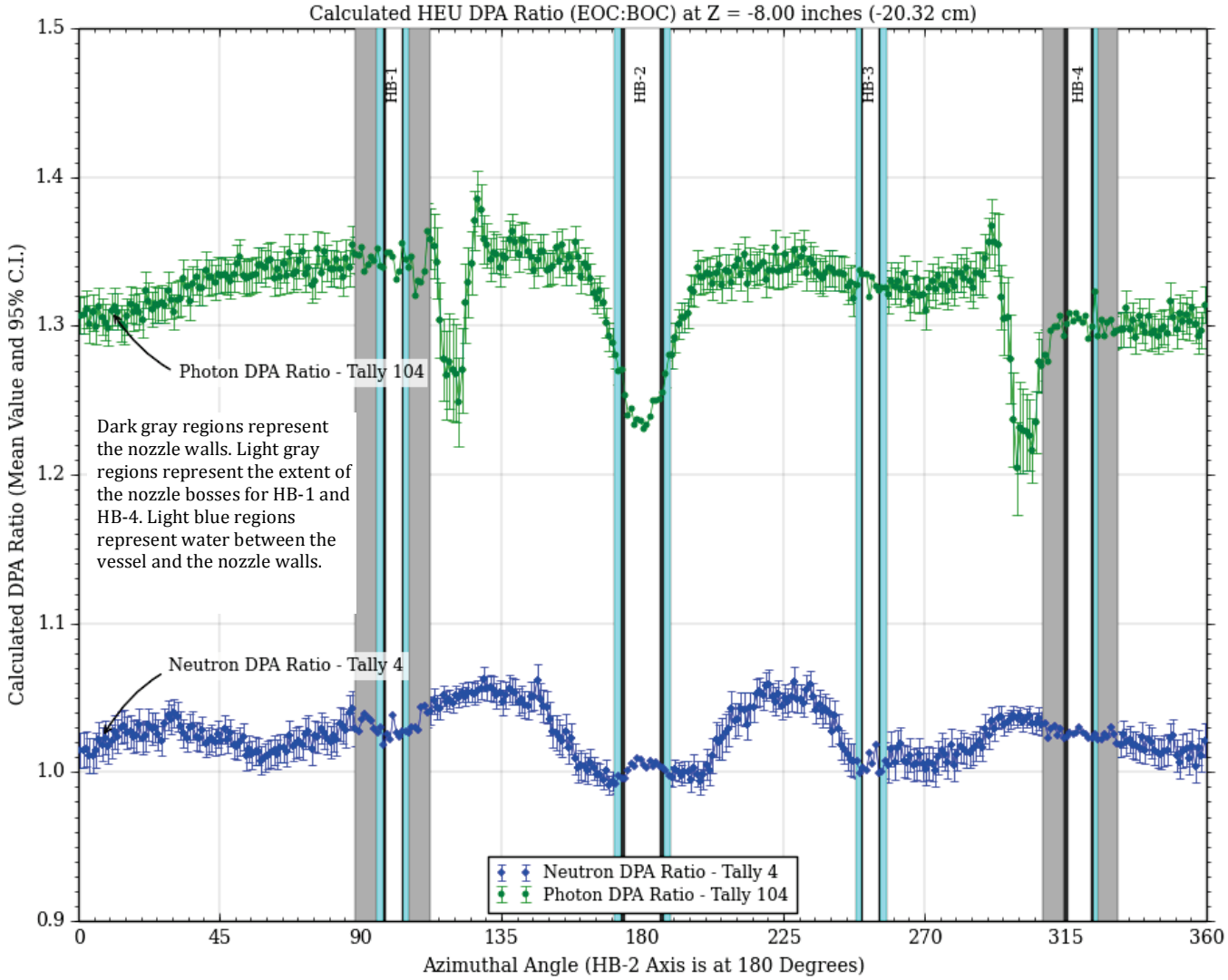

Fig. 4.3-13. HEU EOC/BOC neutron and photon dpa rate ratios at 8 inches below the HFIR core midplane. The presence of beam tubes HB-1 through HB-4 affect the calculated in-vessel dpa rates for several inches above/below the physical extent of these vessel penetrations. Therefore, the azimuthal extent of all four beam tubes at the core axial midplane is depicted on all dpa rate plots, regardless of axial location.

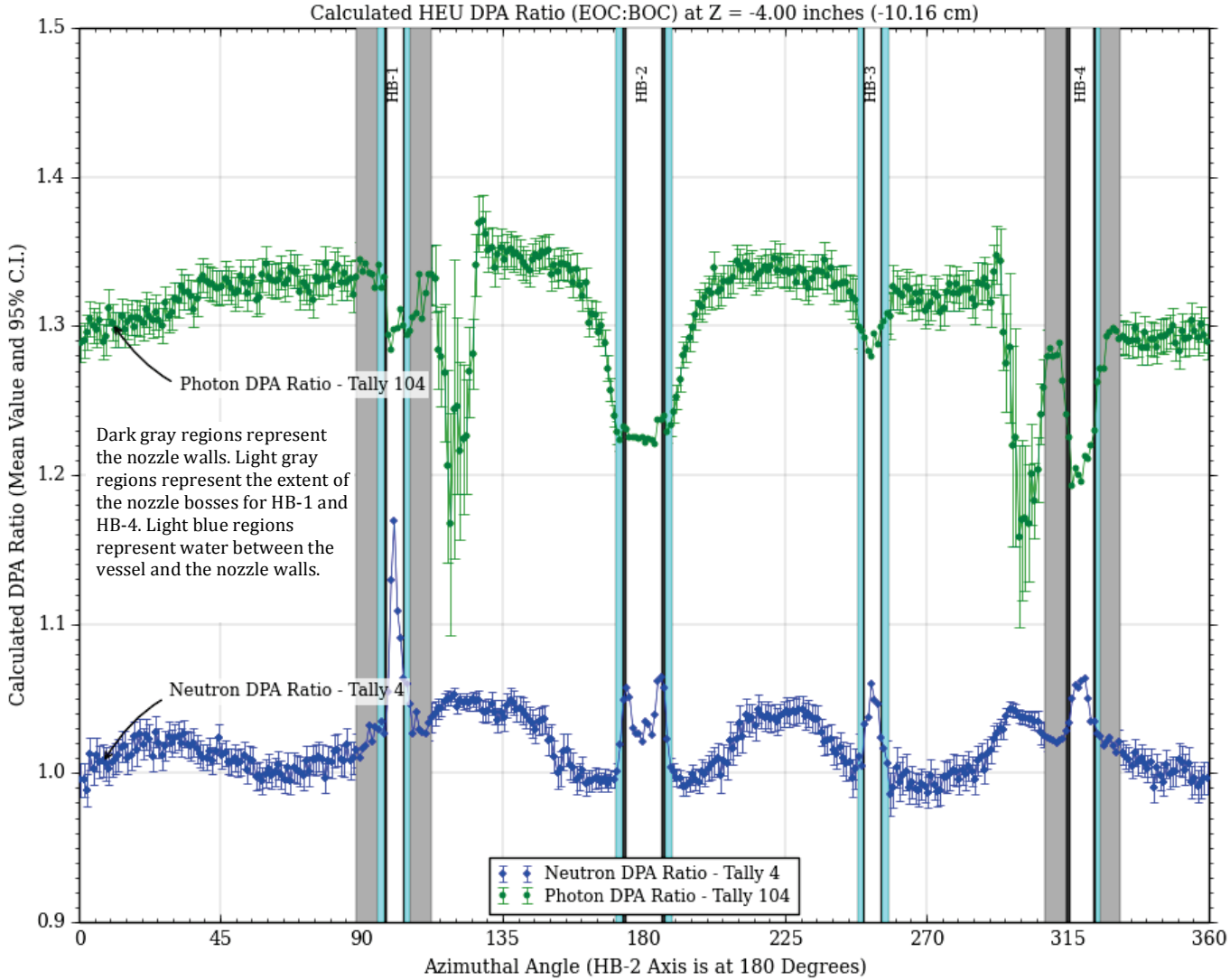

Fig. 4.3-14. HEU EOC/BOC neutron and photon dpa rate ratios at 4 inches below the HFIR core midplane. The presence of beam tubes HB-1 through HB-4 affect the calculated in-vessel dpa rates for several inches above/below the physical extent of these vessel penetrations. Therefore, the azimuthal extent of all four beam tubes at the core axial midplane is depicted on all dpa rate plots, regardless of axial location.

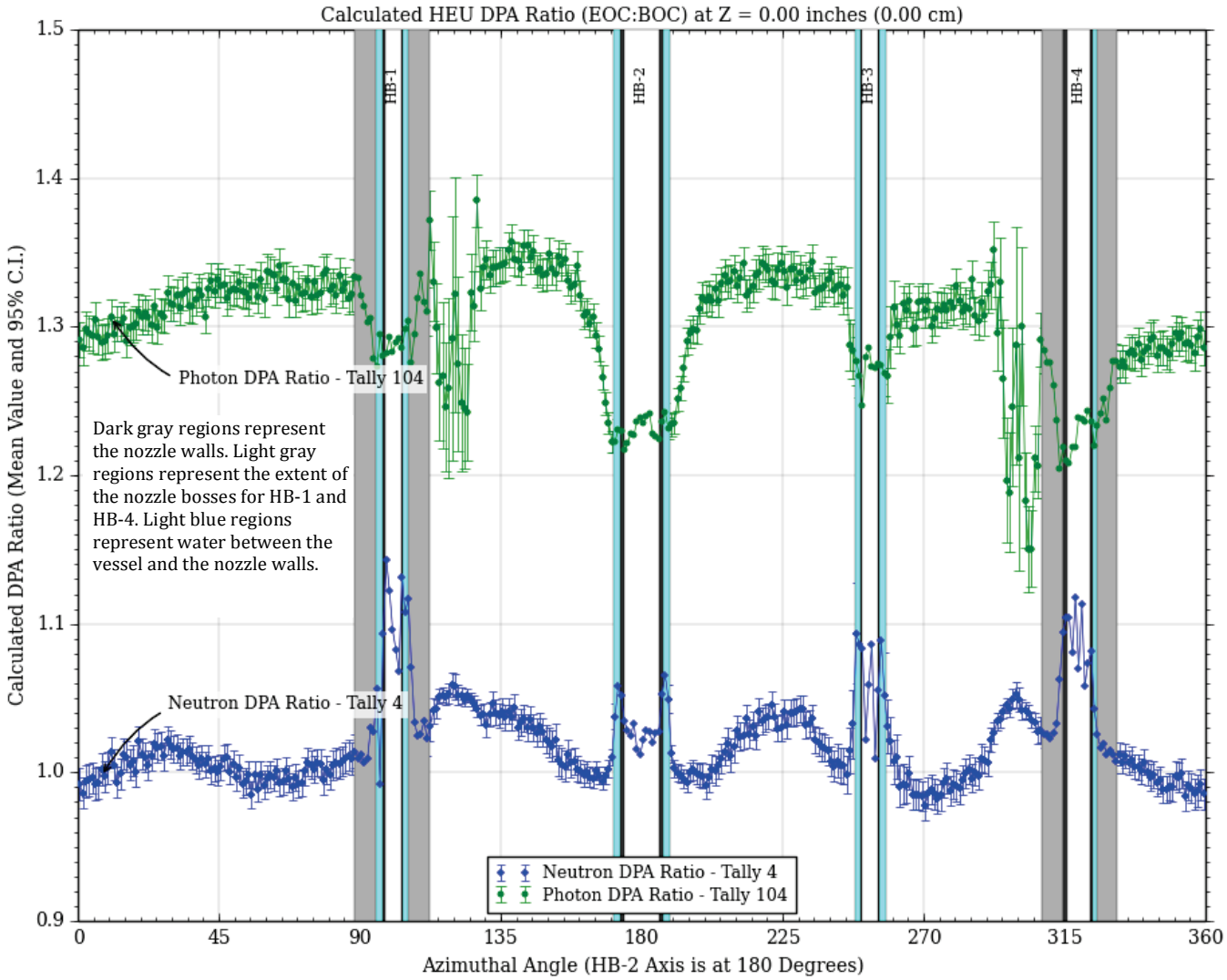

Fig. 4.3-15. HEU EOC/BOC neutron and photon dpa rate ratios at the HFIR core midplane. The presence of beam tubes HB-1 through HB-4 affect the calculated in-vessel dpa rates for several inches above/below the physical extent of these vessel penetrations. Therefore, the azimuthal extent of all four beam tubes at the core axial midplane is depicted on all dpa rate plots, regardless of axial location.

4.4 FISSION PRODUCT PHOTON CONTRIBUTIONS TO RV DAMAGE

Figures 4.4-1 through 4.4-5 present 1-D azimuthal traces of the FP/prompt ratio of the photon dpa rates at a various axial heights in the HFIR RV at BOC. Obviously, at BOC there are no FPs in the core. Therefore, to allow some FPs to build up, the BOC dpa rates are based on the FP photon spectrum that would exist after one day of full power (100 MW) operations. The prompt photon dpa rates include contributions from both fission photons generated in the fueled regions of the core and capture photons generated throughout the model. Based on Fig. 4.1-17 it is obvious that the capture photons dominate the photon dpa rate tally in the RV. Because photons created by capture reactions are typically more energetic than either the prompt fission or delayed FP photons, they will be less effectively attenuated by the high Z materials present in the ICs and dosimetry keys. Away from the influence of these regions, the FP photon contribution to RV dpa rates is generally around 3.5–4% of the prompt (fission + capture) contribution, regardless of axial height.

Tables 3.2-8 and 3.2-9 clearly indicate that slightly more photons are being generated per fission at EOC (11.92) than at BOC (10.58). However, Tables 3.2-8 and 3.2-9 also show that the spectrum is slightly harder at BOC than at EOC. This is expected, because the BOC spectrum is dominated by newly created FPs. Because FPs tend to decay from more highly unstable configurations more quickly than from lower energy nuclear configurations, the highest energy gammas are preferentially emitted earlier. At EOC, the FP population is a mix of newly generated FPs and FPs that have been decaying for more, if not all, of the cycle. The competing effects of slightly more FP photons per fission and a softer overall FP spectrum at EOC lead to an FP/prompt dpa rate ratio that is not significantly different at EOC than at BOC. For example, at 0° at the core axial midplane elevation, the BOC FP/prompt dpa rate ratio is ~3.7%, while this ratio is ~3.3% at EOC. At other elevations, the BOC and EOC differences are even smaller. Because the BOC and EOC behavior is so similar, a separate set of EOC ratio plots is not presented.

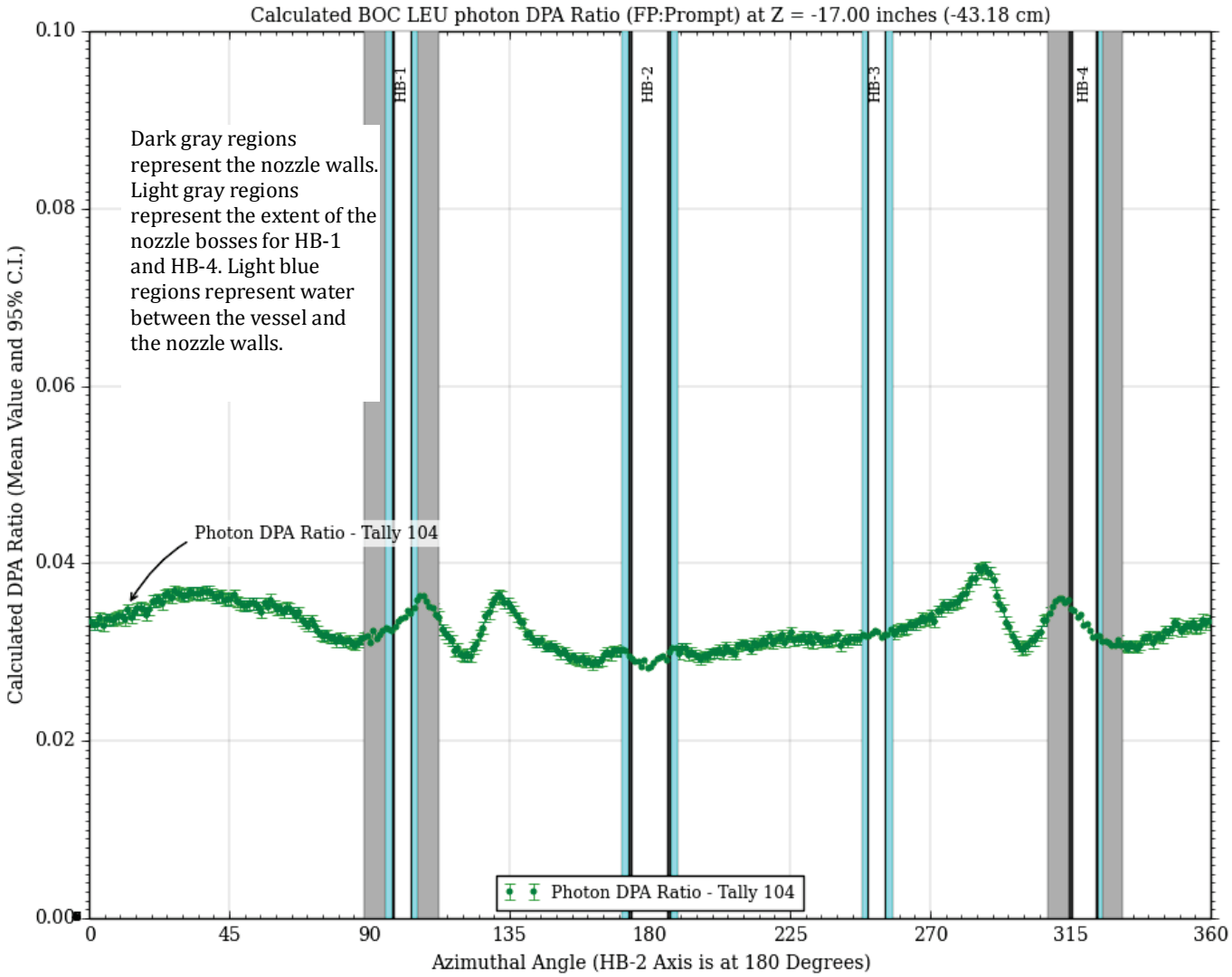

Fig. 4.4-1. LEU BOC FP/prompt photon dpa rate ratios at the elevation of the girth weld (17 inches below the HFIR core midplane). The presence of beam tubes HB-1 through HB-4 affect the calculated in-vessel dpa rates for several inches above/below the physical extent of these vessel penetrations. Therefore, the azimuthal extent of all four beam tubes at the core axial midplane is depicted on all dpa rate plots, regardless of axial location.

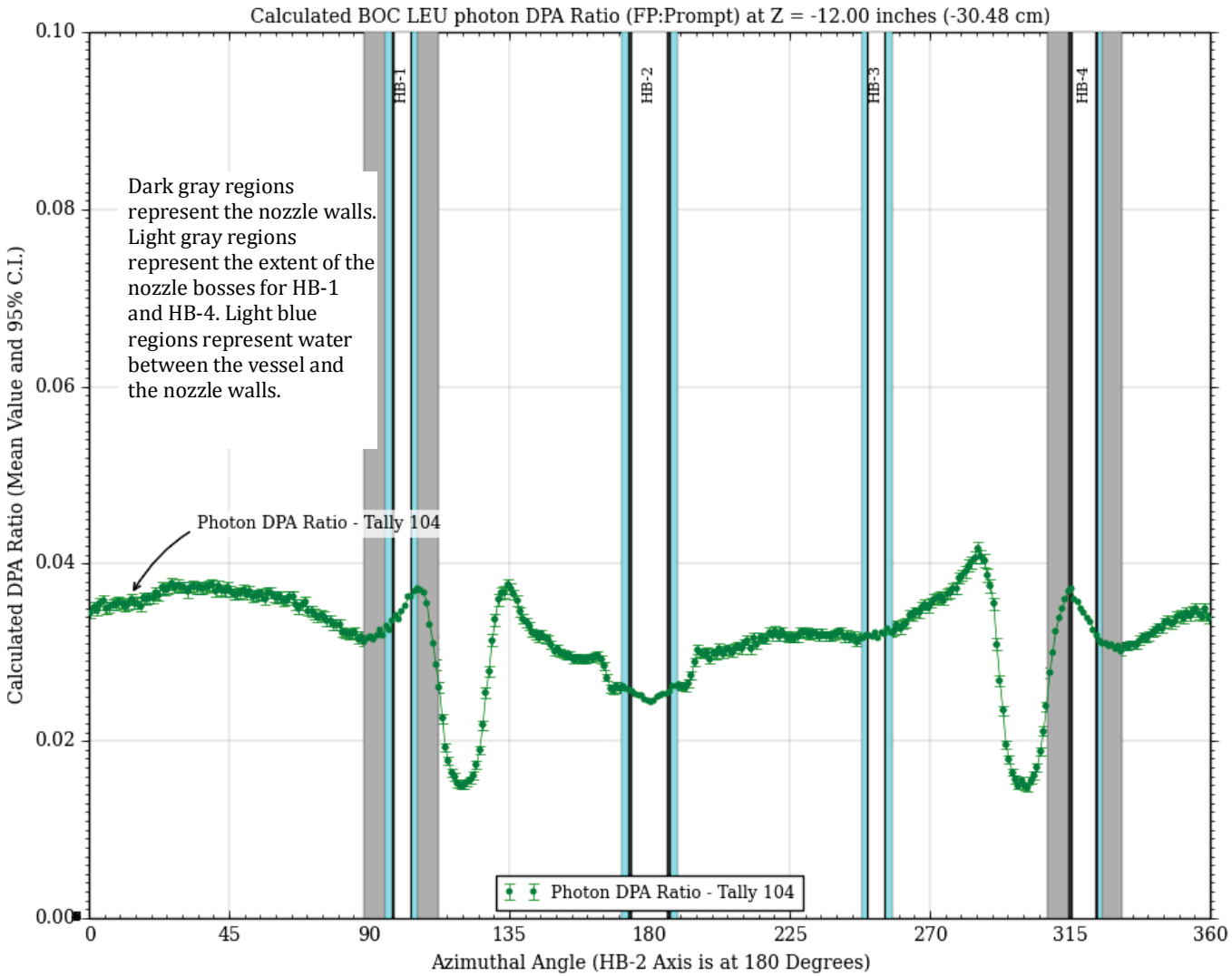

Fig. 4.4-2. LEU BOC FP/prompt photon dpa rate ratios at 12 inches below the HFIR core midplane. The presence of beam tubes HB-1 through HB-4 affect the calculated in-vessel dpa rates for several inches above/below the physical extent of these vessel penetrations. Therefore, the azimuthal extent of all four beam tubes at the core axial midplane is depicted on all dpa rate plots, regardless of axial location.

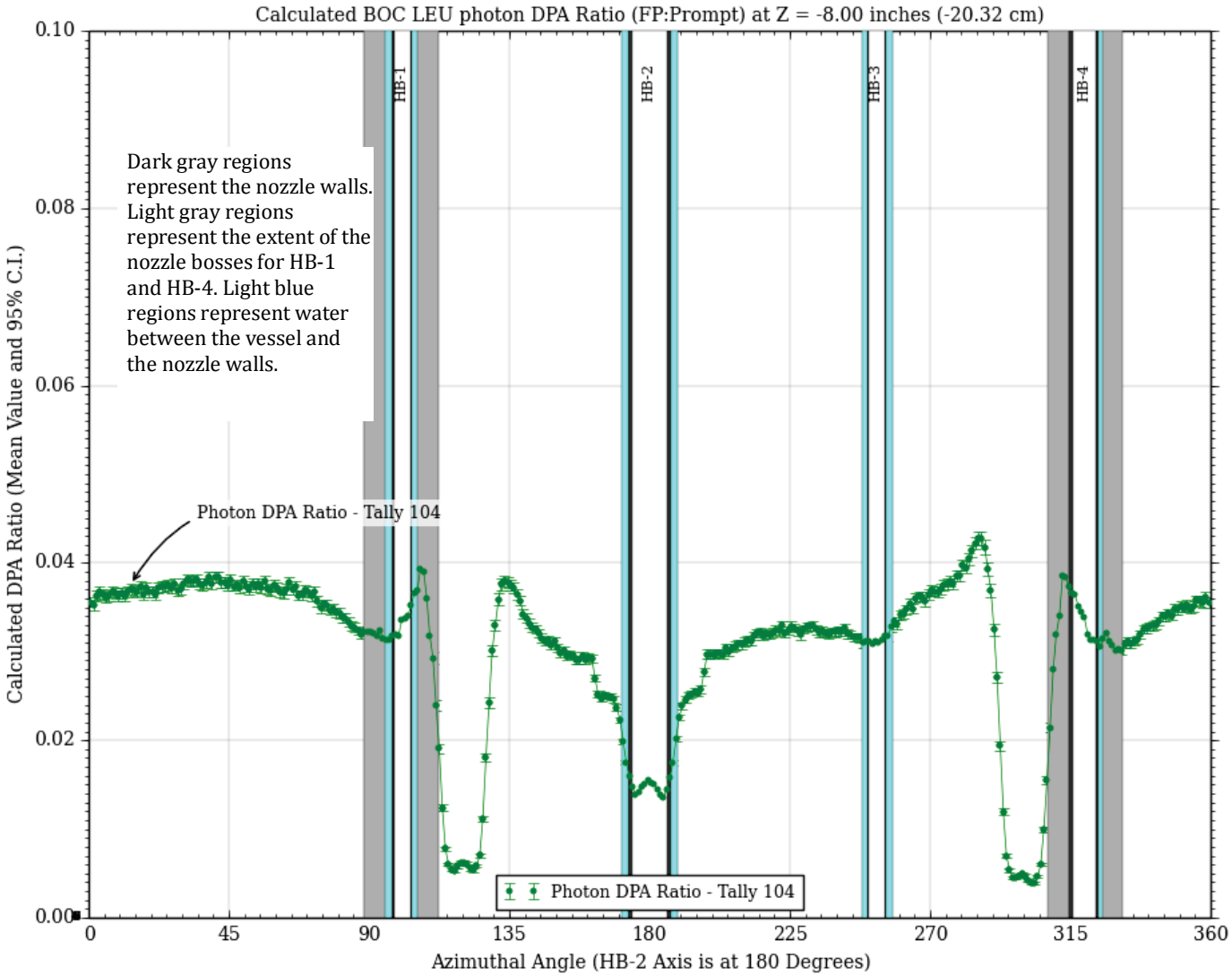

Fig. 4.4-3. LEU BOC FP/prompt photon dpa rate ratios at 8 inches below the HFIR core midplane. The presence of beam tubes HB-1 through HB-4 affect the calculated in-vessel dpa rates for several inches above/below the physical extent of these vessel penetrations. Therefore, the azimuthal extent of all four beam tubes at the core axial midplane is depicted on all dpa rate plots, regardless of axial location.

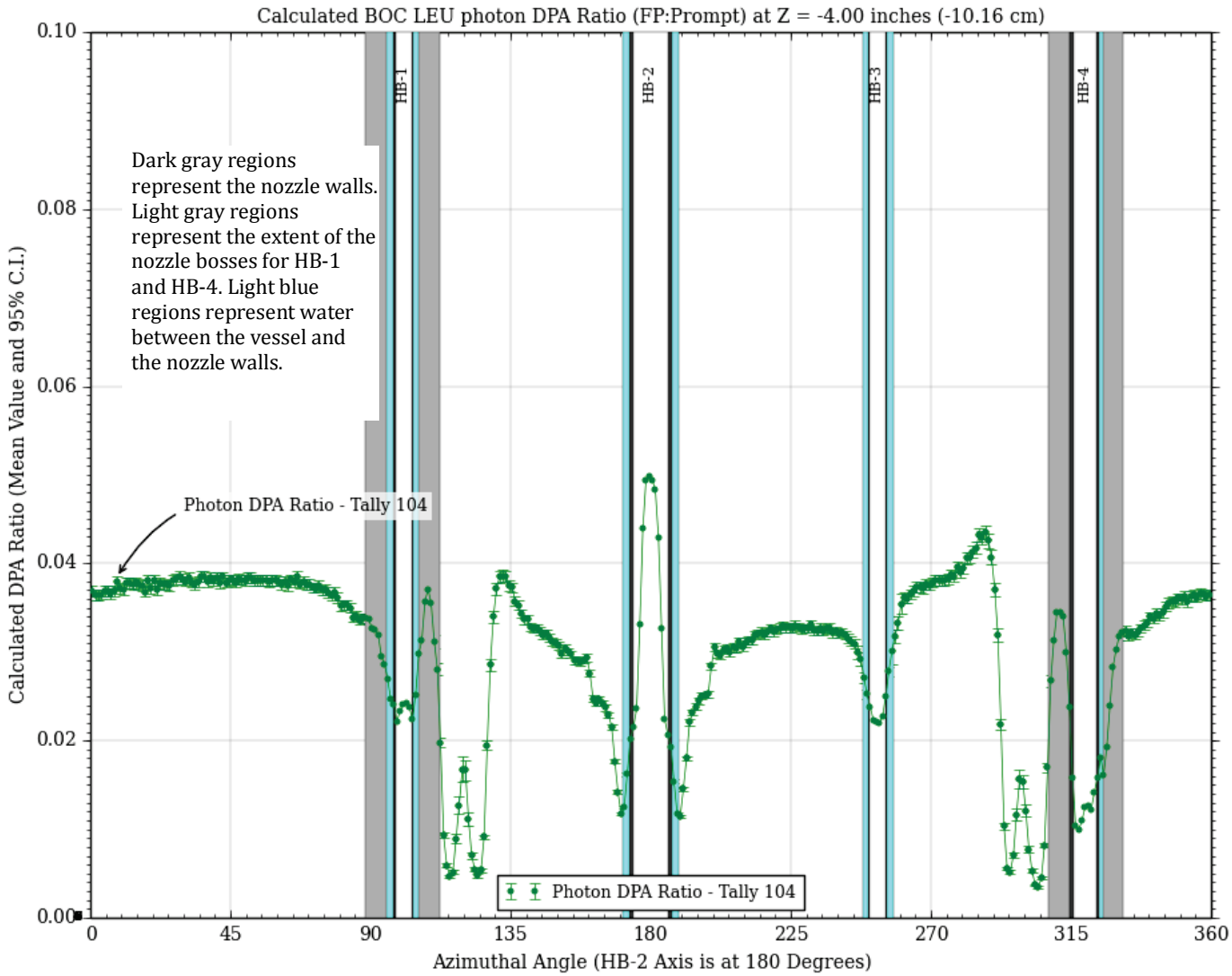

Fig. 4.4-4. LEU BOC FP/prompt photon dpa rate ratios at 4 inches below the HFIR core midplane. The presence of beam tubes HB-1 through HB-4 affect the calculated in-vessel dpa rates for several inches above/below the physical extent of these vessel penetrations. Therefore, the azimuthal extent of all four beam tubes at the core axial midplane is depicted on all dpa rate plots, regardless of axial location.

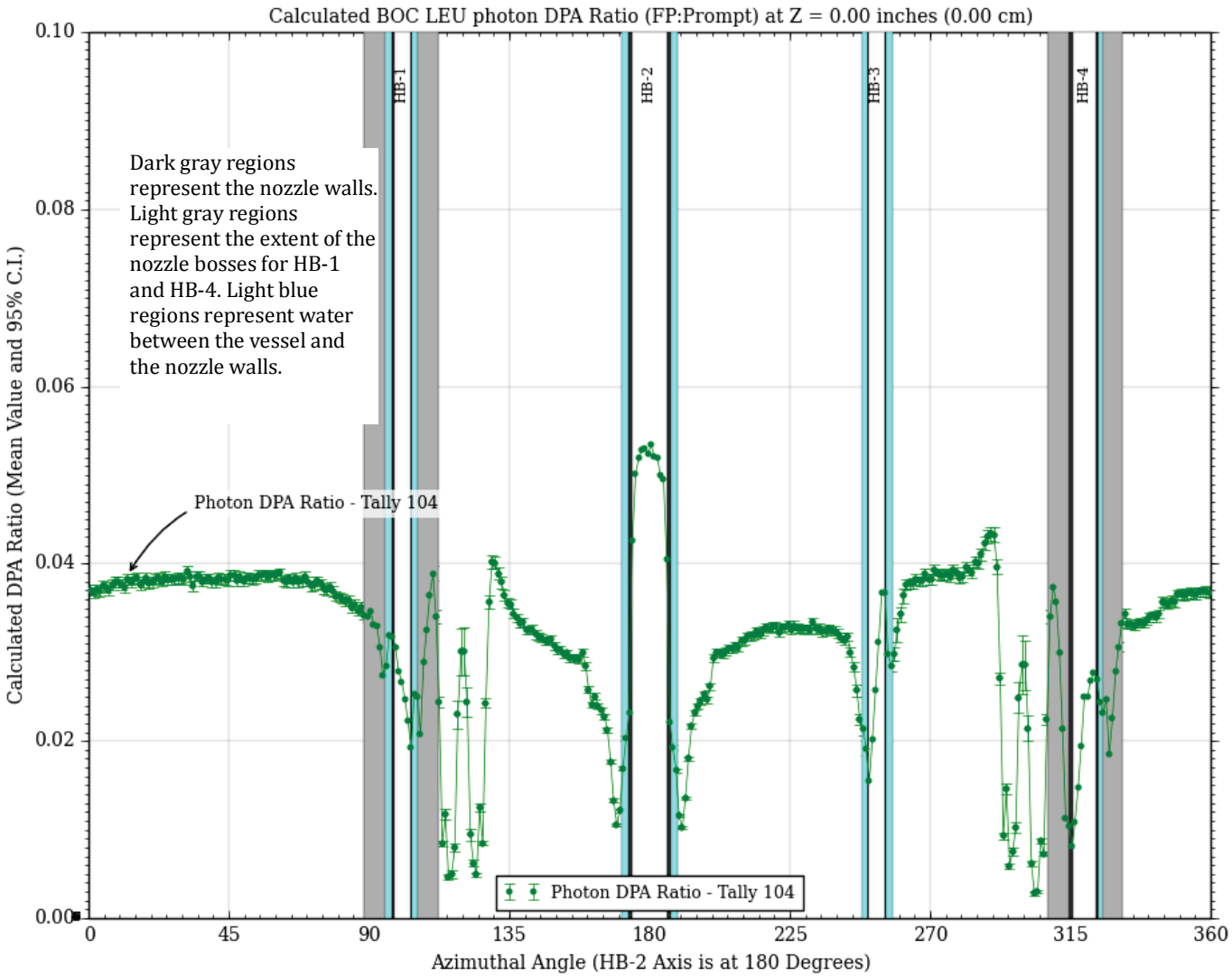

Fig. 4.4-5. LEU BOC FP/prompt photon dpa rate ratios at the HFIR core midplane. The presence of beam tubes HB-1 through HB-4 affect the calculated in-vessel dpa rates for several inches above/below the physical extent of these vessel penetrations. Therefore, the azimuthal extent of all four beam tubes at the core axial midplane is depicted on all dpa rate plots, regardless of axial location.

5. CONCLUSIONS AND RECOMMENDATIONS

Neutron and photon dpa rates in the RV for an LEU core at BOC and EOC, as well as the EOC/BOC ratios of these dpa rates, have been tallied over a finely divided mesh tally covering an axial portion of the RV that extends from 21" below the core axial midplane to 21" above the core axial midplane. This mesh tally has been divided into 1" axial segments and 360 azimuthal segments and covers the first ⅛" of the RV base metal with a single radial mesh. Comparisons of the neutron and photon dpa rates for the current HEU core design and the proposed LEU core design of Ilas and Primm [1] have been made over this same tally mesh. Based on these comparisons, the following conclusions can be made:

- First, and foremost, conversion of HFIR to use the proposed LEU core of Ilas and Primm [1] will have no negative impact on vessel damage relative to current HEU core operations. This conclusion is based on simplified (i.e., homogenized) core models. The newer, more detailed models of Ilas and Chandler [27] indicate that for an HEU core, the vessel damage should not be significantly affected by the choice of core representation (i.e., simplified versus explicit). It is currently anticipated that the vessel damage for an LEU core will also be minimally impacted by the choice of core representation, however, if this is subsequently found to not be the case, additional calculations of LEU vessel damage may be required.

- Neutron dpa rates in the first ⅛" of the RV base metal do not vary significantly over the course of an operational cycle, nor do they vary much between the HEU or LEU cores. LEU EOC neutron dpa rates are typically within ±5% of the BOC values at corresponding axial and azimuthal locations in the first ⅛" of the RV base metal. These same LEU EOC neutron dpa rates are typically 5–7% lower than the corresponding values calculate for the existing HEU core.

- Photon dpa rates in the first ⅛" of RV base metal vary more significantly over the course of an operational cycle and between core types. At BOC, the LEU photon dpa rates are roughly 80% of the corresponding HEU values over much of the RV. Over azimuthal extents of the RV near a beam tube penetration or behind an IC, where photons produced through local neutron captures are dominant, the LEU/HEU ratios generally increase to anywhere between roughly 0.9 and 1.1, depending on height. However, at the elevation of the lower girth weld, the LEU/HEU photon dpa rate ratios are unaffected by the presence of either a beam tube penetration or an IC.

- Photons dominate the total dpa rates tallied in the first ⅛" of RV base metal over a significant azimuthal portion of the RV. Exceptions to this are the azimuthal portions of the RV near either a beam tube or an IC. Within a 3–4° azimuthal arc of the HB-2 beam tube penetration in the RV, the neutron dpa rates in the first ⅛" of the RV base metal are roughly an order of magnitude larger than the photon dpa rates. In the azimuthal region of the RV behind an IC, the neutron dpa rates can exceed the photon dpa rates by more than two orders of magnitude.

The neutron and photon dpa rates presented in this document as well as in Risner and Blakeman [2] were calculated with version 1.60 of the MCNP5 code and were performed on the OIC computing platform. Version 1.6 of MCNP5 on the OIC is currently approved for use. However, at the time the calculations presented in this document and in Risner and Blakeman [2] were performed, this approval was not yet in place. Appendix A describes additional testing of MCNP5 Version 1.6 that was performed on the OIC to support its use in the current and Risner and Blakeman [2] analyses.

6. REFERENCES

[1] G. Ilas and R. T. Primm III, *Low Enriched Uranium Fuel Design with Two-Dimensional Grading for the High Flux Isotope Reactor*, ORNL/TM-2010/318, Oak Ridge National Laboratory, April 2011.

[2] J. M Risner and E. D. Blakeman, *Analysis of dpa Rates in the HFIR Reactor Vessel Using a Hybrid Monte Carlo Discrete Ordinates Methodology*, ORNL/TM-2013/515, Oak Ridge National Laboratory, to be issued.

[3] J. R. McWherter, R. E. Schappel, and J. R. McGuffey, *HFIR Pressure Vessel and Structural Components Material Surveillance Program*, ORNL/TM-1372, Union Carbide Corporation, Nuclear Division, Oak Ridge National Laboratory (January 1966).

[4] R. D. Cheverton, D. M. McGinty, J. R. McWherter, and R. K. Nanstad, *HFIR Pressure Vessel and Structural Components Material Surveillance Program, Supplement 1,* ORNL/TM-1372/S1, Oak Ridge National Laboratory (October 1987).

[5] R. D. Cheverton, R. K. Nanstad, and E. D. Blakeman, *HFIR Pressure Vessel and Structural Components Material Surveillance Program, Supplement 2,* ORNL/TM-1372/S2, Oak Ridge National Laboratory (August 1999).

[6] R. D. Cheverton, R. K. Nanstad, E. D. Blakeman, and H. A. Kmieciak, *HFIR Pressure Vessel and Structural Components Material Surveillance Program, Supplement 3*, ORNL/TM-1372/S3, Oak Ridge National Laboratory (August 2010).

[7] S. W. Mosher et. al., *ADVANTG – An Automated Variance Reduction Generator*, ORNL/TM-2013/416, Oak Ridge National Laboratory (November 2013).

[8] X-5 Monte Carlo Team, *MCNP – A General Monte Carlo N-Particle Transport Code*, *Version 5, Volume I: Overview and Theory*, LA-UR-03-1987, Los Alamos National Laboratory (2003).

[9] T. M. Evans, A. S. Stafford, R. N. Slaybaugh, and K. T. Clarno, "Denovo: a New Three-Dimensional Parallel Discrete Ordinates Code in SCALE," *Nucl. Technol*. 171 (2010): 171–200.

[10] J. C. Wagner and A. Haghighat, "Automated Variance Reduction of Monte Carlo Shielding Calculations Using the Discrete Ordinates Adjoint Function," *Nucl. Sci Eng*. 128 (1998): 186–208.

[11] J. C. Wagner, E. D. Blakeman, and D. E. Peplow, "Forward-Weighted CADIS Method for global Variance Reduction," *Trans. Am. Nucl. Soc*. 97, (2007): 630–633.

[12] R. D., Cheverton et al., *Impact of 2004/2005 Dosimetry and Surveillance Data on the HFIR Vessel Radiation Embrittlement Trend Curve, Hydrostatic Proof Test Conditions, Pressure/Temperature Limits, and Life Extension*, ORNL/TM-2008/007, Oak Ridge National Laboratory (August 2010).

[13] K. T. Farrell, et al., *The DOS 1 Neutron Dosimetry Experiment at the HB-4-A Key 7 Surveillance Site on the HFIR Pressure Vessel*, ORNL/TM-12511, Oak Ridge National Laboratory (January 1994).

[14] I. Remec, J. A. Wang, F. B. K. Kam, K. Farrell, "Effects of Gamma Induced Displacements on HFIR Pressure Vessel Materials," *Journal of Nuclear Materials* 217 (1994): 258–268.

[15] E. D. Blakeman and R. D Cheverton, *Neutron and Gamma Fluxes and dpa Rates for HFIR Vessel Beltline Region (Present and Upgrade Designs) Supplement 2*, ORNL/TM-13693/S2, Oak Ridge National Laboratory (August 2010).

[16] DOORS3.2, RSICC Computer Code Collections, CCC-650, Radiation Safety Information Computational Center, Oak Ridge National Laboratory (1998).

[17] HFIR Safety-Related Software Baseline Revision Approval, SBPF-1300.1-AXMIX-cpile , Software Registry number 001331 (February 7, 2006).

[18] HFIR Safety-Related Software Baseline Revision Approval, SBPF-1300.1-DTD-cpile, Software Registry number 001327 (February 7, 2006).

[19] N. Xoubi and R. T. Primm III, *Modeling of the High Flux Isotope Reactor Cycle 400*, ORNL/TM-2004/251, Oak Ridge National Laboratory (August 2005).

[20] E. D. Blakeman, D. E. Peplow, J. C. Wagner, B. D. Murphy, and D. E. Mueller, *PWR Facility Dose Modeling Using MCNP5 and the CADIS/ADVANTG Variance-Reduction Methodology*, ORNL/TM-2007/133, Oak Ridge National Laboratory (September 2007).

[21] W. Haeck, VESTA User's Manual – Version 2.0.0, IRSN Report DSU/SEC/T/2008-331 Indice A, France (2009).

[22] I. C. Gauld, *ORIGEN-S: Depletion Module to Calculate Neutron Activation, Actinide Transmutation, Fission Product Generation, and Radiation Source Terms*, ORNL/TM-2005/39, Oak Ridge National Laboratory (June 2011).

[23] R. T. Primm III, D. Chandler, G. Ilas, B. C. Jolly, J. H. Miller, and J. D. Sease, *Design Study for a Low-Enriched Uranium Core for the High Flux Isotope Reactor, Annual Report for FY 2008*, ORNL/TM-2009/87, Oak Ridge National Laboratory, (2009).

[24] J. L. McDuffee, *Heat Generation Rates for Various Rabbit Materials in the Flux Trap of HFIR*, C-HFIR-2012-035 Rev. 0, Oak Ridge National Laboratory (2012).

[25] ASTM Standard E693-12, *Standard Practice for Characterizing Neutron Exposures in Iron and Low Alloy Steels in Terms of Displacements Per Atom (DPA)*, E-706 (June 2012).

[26] N. P. Baumann, "Gamma-ray-Induced-displacements in D2O Reactors," *Proc. of the Seventh ASTM0-EURATOM Symposium on Reactor Dosimetry*, Strasbourg, France (August 27–31, 1990).

[27] G. Ilas, D. Chandler, B. J. Ade, E. E. Sunny, B. R. Betzler, and D. L Pinkston, *Modeling and Simulations for the High Flux Isotope Reactor Cycle 400*, ORNL/TM-2015/36, Oak Ridge National Laboratory, February 2015.

APPENDIX A. MCNP5 V1.6 VERIFICATION

APPENDIX A – MCNP5 V1.6 VERIFICATION

DISCUSSION

Version 1.6 of MCNP5 on the OIC has been used to calculate dpa rates in the HFIR RV. At the time the calculations documented in the main body of this report, as well as those documented in Risner and Blakeman [2], were performed, Version 1.51 of MCNP5 on the Betty computing cluster was the MCNP5 version approved for use in HFIR design calculations. Because of the large number of MCNP calculations involved in the latest (both HEU and LEU) dpa rate analyses and the computational resources needed to support these analyses (typically 10 billion histories per run), the capabilities of the OIC and the newer version of MCNP available on that platform were used. To ensure that acceptable results would be obtained for the HFIR HEU and LEU dpa rate analyses performed on the OIC, a rigorous verification of MCNP5 Version 1.6 was performed.

The verification and validation (V&V) of MCNP5 Version 1.6 on the OIC consisted of running several test suites distributed by LANL with MCNP and comparing the results to those generated by the MCNP code developers. Results of a HFIR design model that was run on both the Betty and OIC clusters were also compared.

When the HFIR HEU and LEU MCNP-based dpa rate analyses commenced, the existing MCNP5 Version 1.6 executable on the OIC required the user to explicitly specify a path to the nuclear data for a calculation. A default path to the nuclear data libraries (the DATAPATH variable) is generally specified during compilation. If the DATAPATH variable is not explicitly set at compile time, the compilation scripts will make some assumptions based on the location of the source code files being compiled. If these assumptions are not consistent with the actual location of the nuclear data libraries, the user will need to override them at run time. To avoid the user having to specify a value for the DATAPATH variable for every run, a new compilation was made with a consistent definition of the DATAPATH variable specified at compile time. This compilation also invoked the default behavior of using single precision (4-byte) integers.

Such a single precision (or I4) version is typically acceptable. However, even with the acceleration provided by the ADVANTG program, some difficult deep penetration problems may require several billion particle histories to be run. For example, the final HEU and LEU vessel dpa rate calculations were all performed with 10 billion particle histories to achieve relative errors of less than 1% over the bulk of the region of interest. To perform calculations with this many histories, a double precision integer (I8) executable of MCNP5 Version 1.6 was made. Shortly after this compilation was performed, the OpenMP (OMP) libraries (used by parallel calculations that invoke the POSIX-threads algorithm) on the OIC were upgraded from Version 1.4.3 to Version 1.4.5. A third MCNP5 Version 1.6 compilation was performed requesting double precision integers and the OMP Version 1.4.5 libraries. During this time, investigations to determine why certain problems would abort with an error message of "the weight of the current particle is zero or less." were ongoing. Ultimately, these aborts were traced to the ^{248}Cm data issue discussed in Sect. 3.2.3, "Materials," in the main body of this report. However, because the investigations were underway, a fourth executable was generated explicitly requesting that both integer- and real-valued variables be explicitly defaulted to double precision. This I8R8 version was also linked against the latest OMP Version 1.4.5 libraries. Later it was determined that invoking the I8 compiler option automatically invoked the R8 option, so the I8 and I8R8 executables linked against the OMP 1.4.5 libraries are effectively identical. This was verified by examining both of these executables with the Linux octal dump (od) utility. Comparison of both executables confirmed that they were byte-wise identical except for 12 bytes containing the compilation date string. This string appears in four separate locations in the binary executable and consists of just three characters that are different. The I8OMP145 executable was compiled on 04/25/2012, and the I8R8OMP145 executable was compiled on 05/07/2012. Therefore the

"4," "2," "5" character string in the I8OMP145 executable and the "5," "0," "7" character string in the I8R8OMP145 executables are the only bytes that differ (in four separate locations) between the two executables. These trivial differences in no way affect any of the transport calculations performed by MCNP, so the I8OMP145 and I8R8OMP145 executables can be used interchangeably.

All four of the executables described above were compiled by Mark Baird of the Radiation Safety Information Computational Center (RSICC). All four executables are located in the /projects/MCNP5/MCNP5160_MCNPX270/bin/mod directory on the OIC. Within this directory, the mcnp5.mpi executable was compiled with single precision integers (I4). The mcnp5i8.mpi executable specified double precision integers and linked against the older OpenMP Version 1.4.3 libraries. The mcnp5i8ompi145.mpi and mcnp5i8r8ompi145.mpi executable are both linked against the version 1.4.5 OpenMP libraries.

Because it was unclear how each of the four executables described above would perform at the beginning of the HFIR HEU and LEU RV dpa rate analyses and concurrent V&V testing, all problems in the various MCNP test suites were run with all four executables. The HFIR LEU EOC RV dpa rate calculation run on Betty and the OIC was only run with the mcnp5i8r8ompi.mpi executable on the OIC. This design model was run with the approved /usr/local/mcnp5_v150/bin/mcnp5.mpi executable on the Betty cluster.

The first test suite to be executed on the OIC was the MCNP "Regression" test suite. This test suite consists of 61 small problems that test various code features, including the ability to correctly detect incorrect user inputs and appropriately abort. For all four MCNP5 Version 1.6 executables, 59 of the 61 output files compared identically between the OIC and LANL-supplied results. LANL supplies outputs for jobs run on a Linux platform and outputs run on Windows-based PCs. For the two jobs that did not exactly match the LANL-supplied Linux results, the difference between the OIC and LANL-supplied results were identical within the difference between the LANL-supplied Linux results and the LANL-supplied Windows results. That is, for these two problems, the OIC results exactly matched the LANL-supplied Windows results. This suggests that the Linux and Windows output files for these two test problems were likely switched in the LANL distribution.

The second test suite executed on the OIC was the "VALIDATION_CRITICALITY" test suite. This test suite consists of 31 models from the International Handbook of Evaluation Criticality Safety Benchmark Experiments. This allows for a comparison of calculated and measured values for k_{eff}. Except for lines containing date/time information, all four MCNP5 Version 1.6 executables on the OIC produced identical output files. For 28 of the 31 benchmark measurements, the OIC and LANL-supplied results for k_{eff} matched identically. For the three remaining cases, slight differences were noted; however, the LANL-supplied results file states that the values were calculated with a beta release of MCNP Version 1.6. Changes to the code between the final release and the beta release could result in a different random walk, which would change the calculated results slightly. In all three cases where the calculated value for k_{eff} differed, the error bands on the OIC and LANL-supplied values for k_{eff} overlapped. Therefore, the OIC and LANL calculated values for k_{eff} can be considered statistically equivalent.

The third test suite executed on the OIC was the "VALIDATION_SHIELDING" test suite consisting of 19 dose rate and attenuation factor calculations used by MCNP developers to assess the impact of code and data changes. All four MCNP5 Version 1.6 executables on the OIC produced identical results. Comparison with the LANL-supplied files revealed numerous differences. However, the LANL results contain some oddities. In many output files, some data tables appear out of order. Problems run in parallel can display this behavior for certain data tables if the actual data is not reordered by the master task. However, the tables demonstrating the out of order condition are normally reordered by the master task. All OIC results for these tables were properly ordered, as were the LANL Windows-based results. Also, in some tally results files (MCTAL files), the number of random numbers used in the calculation differed

between the OIC and LANL results. This indicates a different random walk in the two problems. The LANL results might have been run with a slightly different version of the code (perhaps the same beta release version explicitly indicated in the VALIDATION_CRITICALITY test suite results). Because of the oddities in the base case LANL results, the VALIDATION_SHIELDING results were disregarded.

The fourth test suite executed on the OIC was the "VERIFICATION_KEFF" test suite consisting of 75 analytical benchmark models. With the exception of lines containing date/time information or data values that include the central processing unit (CPU) time of a calculation in the result, all four MCNP5, Version 1.6 executables on the OIC produced identical results. An example of a data value including the CPU time for a calculation is the FOM, which is defined as $1/(R^2 +T)$, where R is the relative error associated with a specific tally and T is the CPU time used in the calculation of that tally. No LANL-generated results were provided for this test suite. Comparisons of the OIC-generated results show that 34 of the 75 cases match the analytic result for k_{eff} to within 1 standard deviation. A further 21 of the 75 cases show that MCNP5 Version 1.6 calculates a value for k_{eff} to between 1 and 2 standard deviations of the analytic result. Only 4 cases show a calculated difference of between 2 and 3 standard deviations from the analytic result. Finally, 16 cases show MCNP5 results that are flagged as being more than 3 standard deviations away from the analytic result. However, 10 of these 16 cases show a calculated value for k_{eff} that matches the analytic result to 5 printed decimal places. Furthermore, for these 10 cases, the printed standard deviation of the calculation is listed as 0.00000. This demonstrates that either the actual difference between MCNP5 and the analytic result occurs beyond the 5^{th} decimal place or that the comparison logic incorrectly handles standard deviations that are identically "0" to five decimal places. It is also noted that the MCNP5 calculated values for k_{eff} depend on the input nuclear data. Given the data dependence, the relatively good agreement for most of the problems, and the expectation that some results will always be different from the true solution due to the stochastic nature of MCNP5, the results of the VERIFICATION_KEFF test suite support the conclusion that MCNP5 is functioning acceptably for this test suite.

A final test suite consisting of three simple 3-D problems with voids were run. The "KOBAYASHI" test suite is derived from a set of benchmarks established by the Organisation for Economic Co-Operation and Development (OECD), and each of the three problems are run with a fictitious set of nuclear data that define the nonvoid material to be either a pure absorber or a material that is a 50/50 mix of a pure absorber and a pure scatterer. With the exception of lines containing date/time information or data values that include the CPU time of a calculation in the result, all four MCNP5 Version 1.6 executables on the OIC produced identical results. Again, no LANL-generated results were available. However, the OIC-generated results generally matched the OECD-published results within 1% for nearly all tallies. For this test suite, both the MCNP5 and OECD results are calculated results. For the few detector locations where the results differed by more than 1%, the MCNP relative errors were fairly large (up to 9%) and much larger than the error associated with the corresponding benchmark calculation (e.g., 9.04% versus 0.38% for the worst case result). Overall, the agreement between MCNP and the benchmark results is excellent.

In addition to the various test suites distributed with MCNP5, a HFIR design case was run with both the OIC MCNP5 Version 1.6 executable (mcnp5i8r8omp145.mpi) and the currently qualified Betty MCNP5 Version 1.51 executable. Both codes used the same ENDF/B-VII.0 nuclear data set. However, because the codes are different, the results are expected to be slightly different. As seen in Figs. A-1 through A-5, the ratio between the dpa results obtained with the OIC and Betty MCNP5 versions are typically within a few percent of 1.0. Both the OIC and Betty calculations were run for 1E9 histories. This is an order of magnitude fewer that were used for the actual HEU and LEU RV dpa rate analyses. Therefore, the relative errors are larger, typically 1–5% depending on axial elevation. Even with the larger uncertainties, it can be seen in Figs. A-1 through A-5 that the OIC and Betty results appear to be centered and normally distributed around a ratio of 1.0.

OBSERVATIONS

- Four separate executables of MCNP5 Version 1.6 have been created on the OIC computing cluster. These versions were all generated as part of the process of debugging anomalous behaviors in the initial phases of the HFIR HEU and LEU RV dpa rate analyses.

- With the exception of lines containing date/time information or lines containing results that depend on the CPU time of the calculation, all four of these executables yield identical results for a variety of standard MCNP5 test suites.

- Two of these executables—namely the mcnp5i8omp145.mpi and mcnp5i8r8omp145.mpi in the /projects/MCNP5/MCNP5160_MCNPX270/bin/mod directory on the OIC—are byte-wise identical except for 12 bytes containing compilation date information.

- Results from the various MCNP5 test suites are effectively equivalent with the results provided with the MCNP5 distribution except for the VALIDATION_SHIELDING test suite. Several anomalies in the LANL-provided results for this test suite suggest that a different beta release version of MCNP5 was used to generate the LANL results for this test suite. In many cases, the OIC and LANL results agree. For cases in which this agreement is not seen, LANL results appear anomalous.

- In addition to the various MCNP5 standard test suites, a HFIR design model was run on the OIC (MCNP5 Version 1.6) and Betty (MCNP5 Version 1.51) clusters. Results from the OIC and Betty calculations are statistically equivalent.

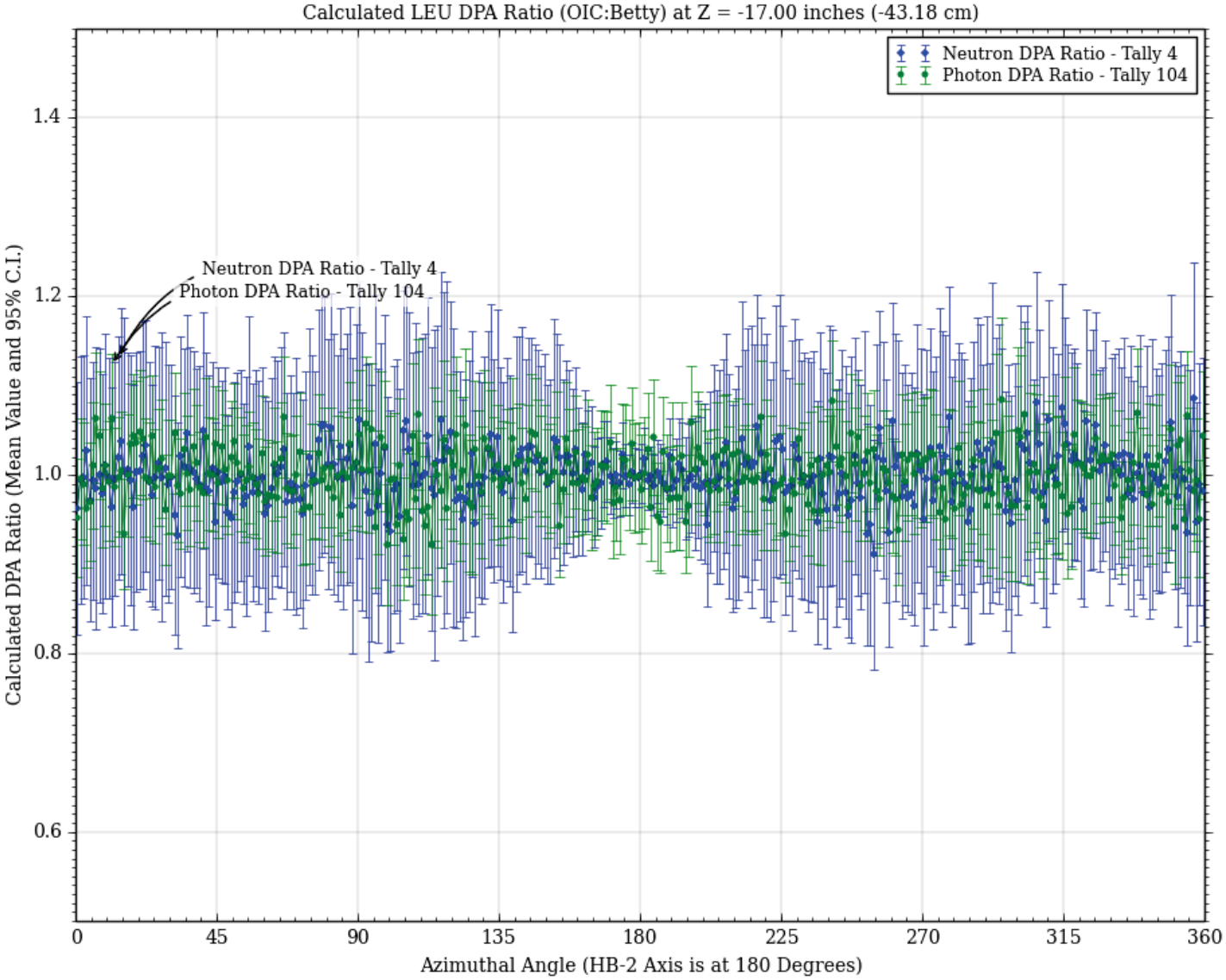

Fig. A-1. HFIR LEU EOC RV dpa rate ratio (OIC to Betty) at the elevation of the girth weld (17 inches below core midplane).

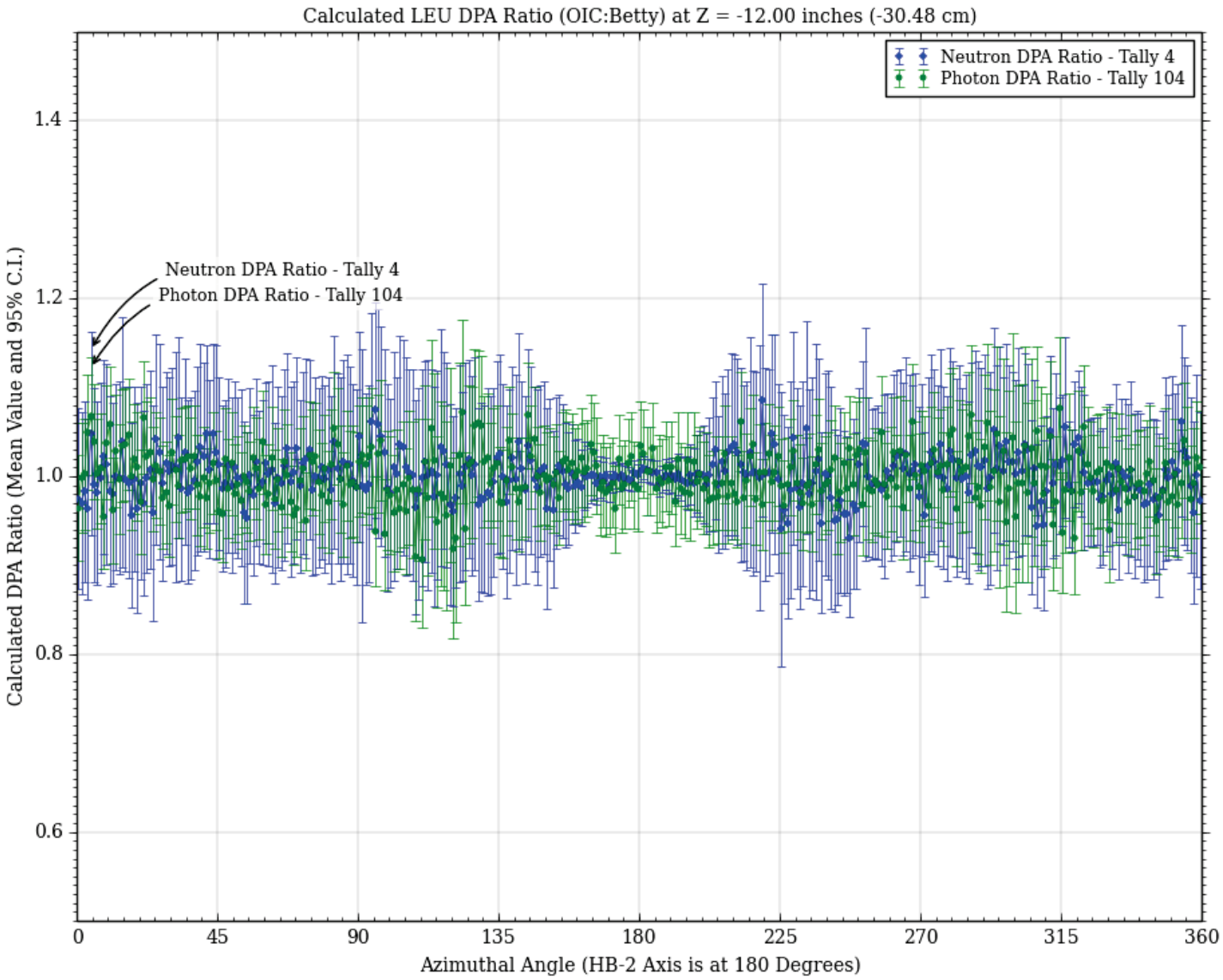

Fig. A-2. HFIR LEU EOC RV dpa rate ratio (OIC to Betty) at 12 inches below the core midplane.

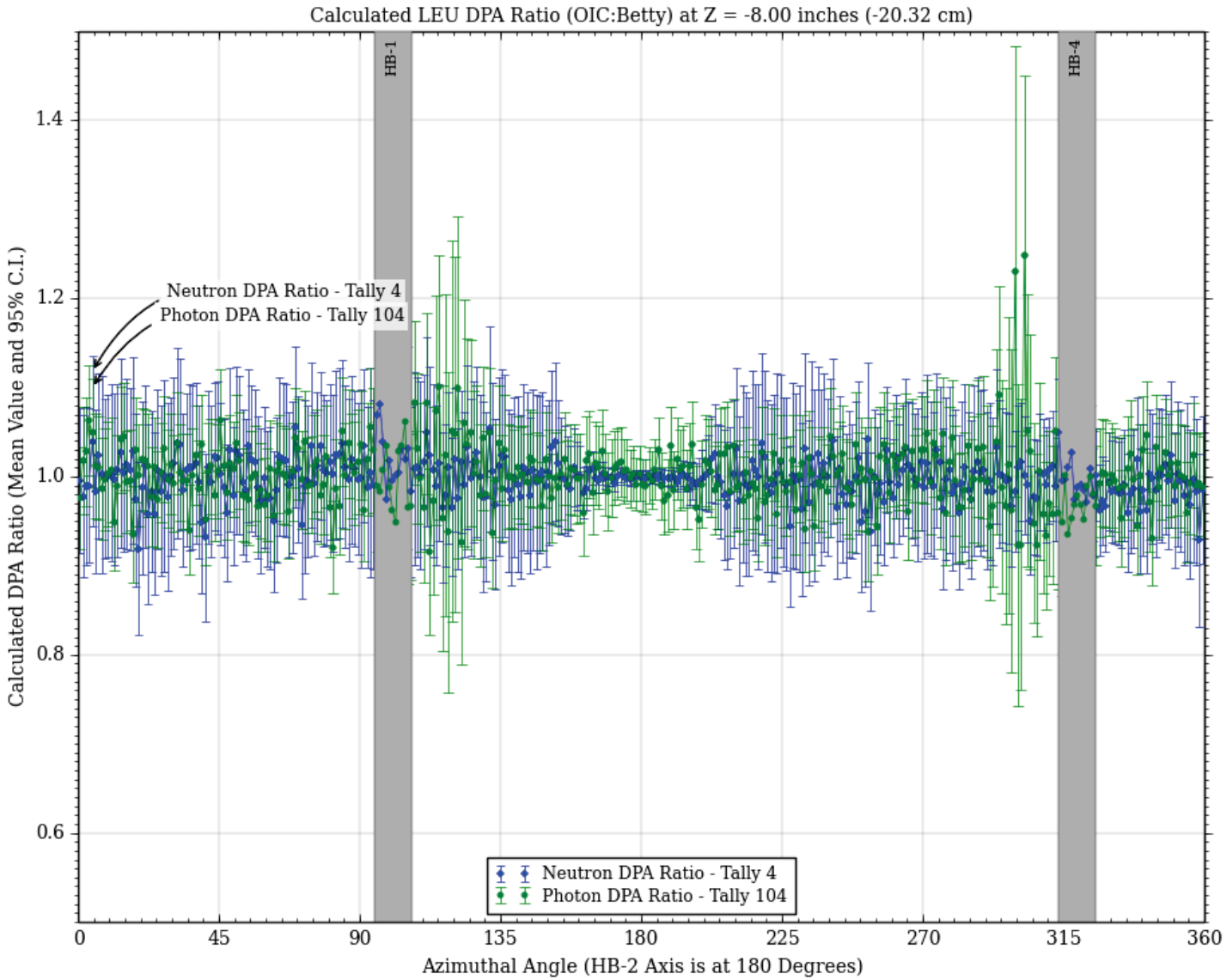

Fig. A-3. HFIR LEU EOC RV dpa rate ratio (OIC to Betty) at 8 inches below the core midplane.

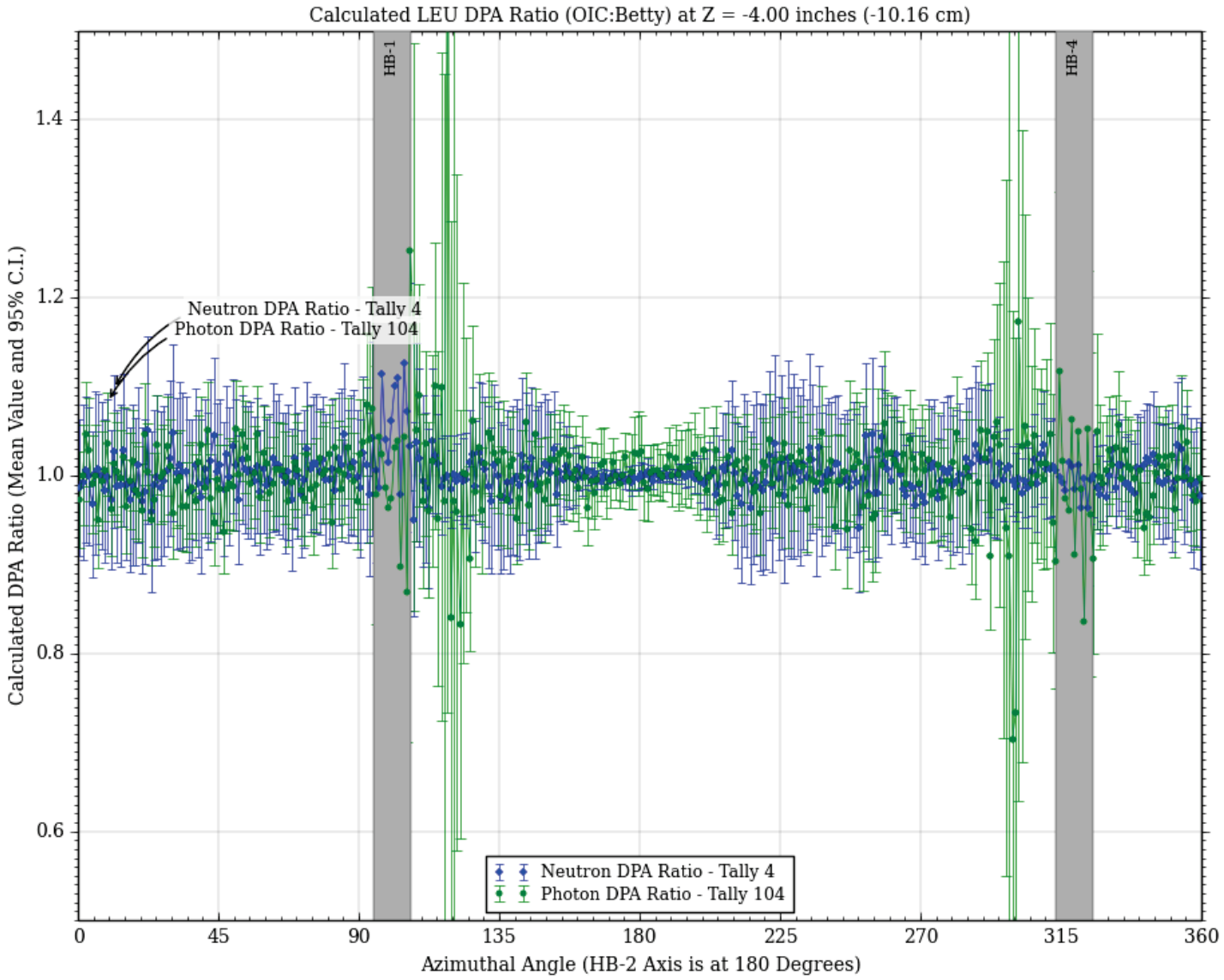

Fig. A-4. HFIR LEU EOC RV dpa rate ratio (OIC to Betty) at 4 inches below the core midplane.

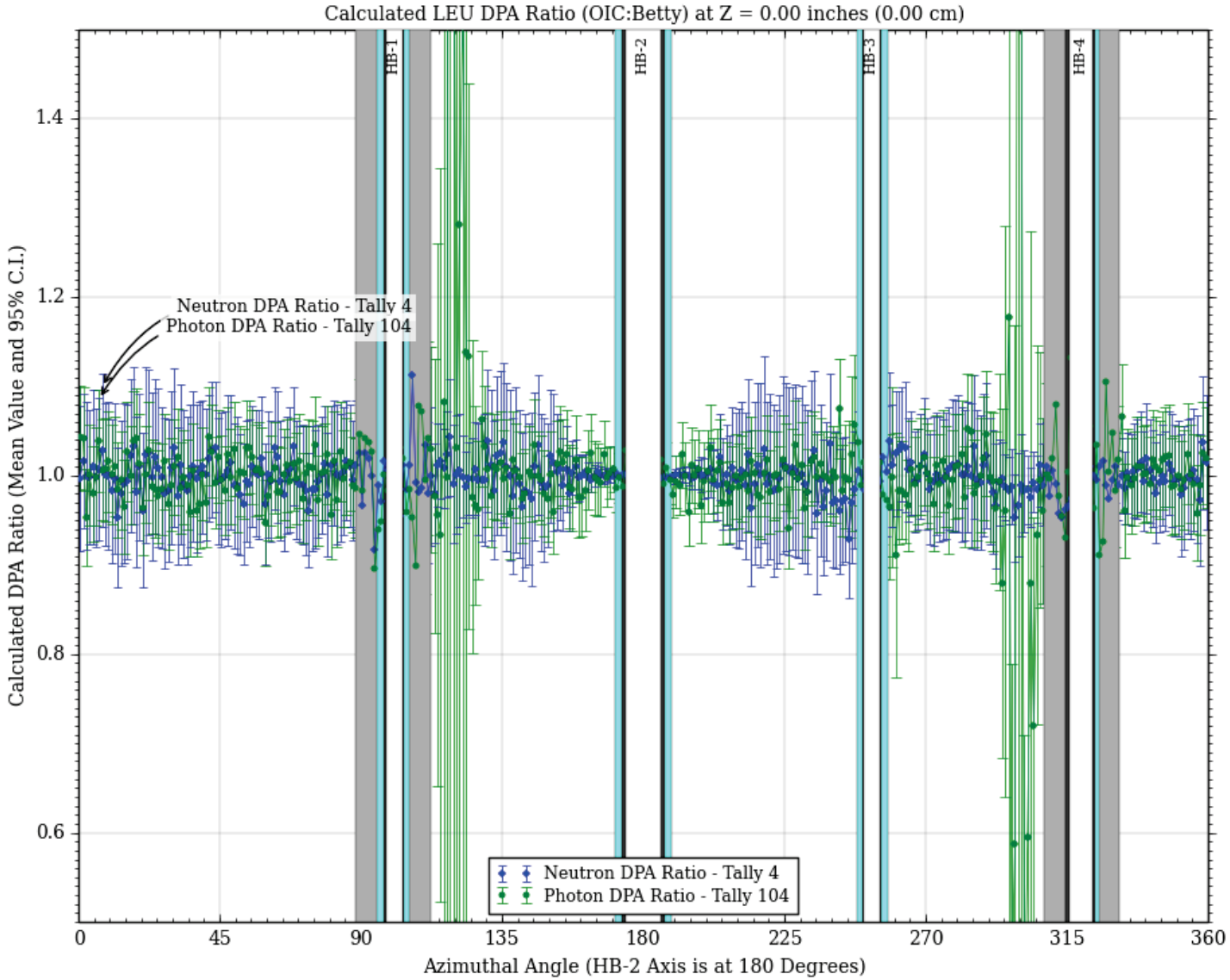

Fig. A-5. HFIR LEU EOC RV dpa rate ratio (OIC to Betty) at the core midplane.

DISTRIBUTION

D. G. Renfro
K. A. Smith
H. A. Kmieciak, Jr.
D. Chandler
R. E. Grove
J. M. Risner
G. Ilas
C. R. Daily
S. C. Wilson